TÉCNICO LISBOA

Numerical Study of the Entrainment Small Scale Features/ Characteristics in Viscoelastic Turbulent Jets

Ricardo Daniel Baptista Marques

Thesis to obtain the Master of Science Degree in

Mechanical Engineering

Examination Committee

Chairperson: Prof. Luís Rego da Cunha Eça
Supervisor: Prof. Carlos Frederico Neves Bettencourt da Silva
Members of the Committee: Prof. José Manuel da Silva Chaves Ribeiro Pereira
Prof. Luís Manuel de Carvalho Gato

November - 2012

Abstract

The main goal of this work centers on studying the turbulent entrainment phenomenon in a viscoelastic flow. Direct numerical simulations (DNS) of a turbulent plane jet with two viscoelastic fluids (different polymer concentrations) are compared to a flow of Newtonian fluid. Therefore, it was also intended to develop and verify a computational code to simulate viscoelastic flows.

Besides, at the turbulent/non-turbulent interface, conditional statistics are performed in order to study the invariants of the velocity gradient, rate-of-strain and rate-of-rotation tensors. These quantities give precious information concerning the topology and geometry of deformation of the infinitesimal fluid elements.

For the computational verification, simulations of decaying homogeneous viscoelastic turbulence were carried out and the results were compared to the ones present in the literature.

It was verified that polymer additives lead to an inhibition of the turbulent phenomena at the small range of scales. Therefore, the two types of fluids are very similar, from the topological and dynamic point of view, but turbulence in this type of flows is less intense.

Keywords: turbulent entrainment; viscoelasticity; plane jet; FENE-P; DNS.

Resumo

O objectivo deste trabalho passa por estudar o fenómeno do arrastamento turbulento num escoamento viscoelástico. Para tal, simulações numéricas directas (DNS) de um jacto plano turbulento com dois fluidos viscoelásticos (de diferentes concentrações poliméricas) são comparadas com a de um fluido Newtoniano. Para tal, fazia parte dos objectivos deste trabalho o desenvolvimento e a verificação de um código computacional para a simulação de escoamentos viscoelásticos.

Além disso, na interface turbulenta/não-turbulenta, são ainda realizadas estatísticas condicionais por forma a estudar os invariantes dos tensores gradiente de velocidade, taxa-de-deformação e taxa-de-rotação. A análise destas quantidades permite inferir acerca da topologia e geometria de deformação dos elementos de fluido infinitesimais.

Para a verificação computacional, realizaram-se simulações de turbulência homogénea viscoelástica em decaimento e os resultados foram comparados com os presentes na literatura científica.

Foi constatado que a adição de cadeias poliméricas conduz a uma inibição dos fenómenos turbulentos na pequena escala. Isto leva a que os escoamentos sejam em tudo semelhantes, do ponto de vista topológico e dinâmico, mas que a turbulência neste tipo de escoamentos seja menos intensa.

Palavras-chave: arrastamento turbulento; viscoelasticidade; jacto plano; FENE-P; DNS.

Contents

List of Figures

List of Tables

Nomenclature

DHIT	Decaying homogeneous isotropic turbulence
DNS	Direct numerical simulations
EDP	Energy decay period
EPP	Energy propagation period
FENE	Finite elastic non-linear extensibility
PDF	Probability density function
T/NT	Turbulent/non-turbulent

Greek symbols

β	Polymer solution concentration
λ	Taylor microscale
λ_p	Polymer relaxation time
$\nu^{[p]}$	Polymer viscosity
$\nu^{[s]}$	Solvent kinetic viscosity
Ω	Enstrophy
ω	Vorticity
ρ	Fluid density
ε	Energy dissipation rate
ξ	Total turbulent kinetic energy

Roman symbols

$\mathbf{u}$	Velocity vector
L	Maximum polymer extension
L_x, L_y, L_z	Computational domain size

N_x, N_y, N_z Grid resolution

p Pressure

Re Reynolds number

u, v, w Velocity Cartesian components

Subscripts

∞ Free-stream condition

i, j, k Computational indexes

x, y, z Cartesian components

ref Reference condition

Chapter 1

Introduction

1.1 Motivation

Over 60 years ago, B.A. Toms discovered that by adding a minute amount of long-chain polymer or some kinds of surfactant additives into a turbulent liquid flow, a dramatic frictional drag reduction would be achieved [1]. This phenomenon, the so-called Toms effect, has great potential in industrial applications, such as in saving pumping power in a water-circulating device like a district heating/cooling system and long-distance liquid transportation pipeline systems. To interpret this turbulent drag reduction, many researchers have paid much attention to theoretical, experimental and numerical simulation studies on drag-reducing flows by additives. Proof of that is the large literature body on the subject [2] and the considerable increase on the number of contributions over the last two decades ([3] for an updated list of references).

In spite of all this research, the physical mechanisms underlying the effect of dilute polymers and turbulence remain involved in a great deal of mistery. This is not surprising, since the problem includes two poorly understood matters: turbulence and additives dynamics. In the wall-bounded turbulent flows, the inhomogeneity emerging from the wall makes it difficult to analyse the interaction between turbulence and polymer microstructures, due to the multitude of competing effects. In constrast, by removing the wall, such as for homogeneous isotropic turbulence (HIT) or bulk turbulence, it is easier to isolate and study those interactions. Therefore, these kind of studies have fundamental importance towards understanding the physics behind additives-turbulence interaction and, so far, they were able to offer a preliminary understanding of the flow characteristics [4]. Drag reduction (DR) is the most well known large scale phenomena, but there is a consensus that the direct action of the polymers is on the small scales of turbulent flows [5].

Nevertheless, more recently, a progress has been made to begin to elucidate these interactions in detail. These advancements come from largely detailed turbulence measurements in flows of dilute polymer solution using laser-based optical techniques and numerical simulations of viscoelastic turbulent flows [6]. In fact, over the past 20 years, direct numerical simulations (DNS) have played an increasingly important role in the investigation of not only this subject, but also the turbulence itself. DNS has the

advantage over laboratory experiments of describing the orientation of the polymer microstructure in addition to the velocity field and Reynolds stress. This information has provided additional insight into mechanism(s) responsible for low/high drag reduction as well as the maximum drag reduction limit [7].

Many researchers have carried out DNS for forced HIT (FHIT) and decaying HIT (DHIT) to study the additives-turbulence interaction and physical mechanism of DR ([5], [8] for FHIT and [10], [11] for DHIT). These importante studies were mainly focused on the DR phenomenon and the characteristics of HIT with polymer additives. However, how the flow structures interact with polymer microstructures has still not been investigated in all its extention. This is the motivation for this work, to study the influence of the polymer additives on the microscales of a turbulent flow, namely on the turbulent entrainment process.

In order to achieve this, attention is given to the turbulent/non-turbulent (T/NT) interface separating the turbulent and the irrotational flow regions. Using a DNS of a turbulent plane jet it is possible to observe the physical mechanisms and dynamics present at this interface, the ones responsible for turbulent entrainment. The focus will be centered on this phenomenon and on the differences that polymer additives cause in relation to a Newtonian fluid.

The study of the invariants allows a detailed characterization of the dynamics, geometry and topology of the flow during the entrainment. The invariants are scalar quantities whose values are independent of the orientation of the coordinate system and contain information concerning rates of vortex stretching and rotation, and on the topology and geometry of deformation of the infinitesimal fluid elements [12]. They have been extensively used in several flow configurations such as isotropic turbulence [13], turbulent mixing layers [14] and turbulent channel flows [15]. In this way, by analysing the evolution of the invariants of the velocity gradient, rate-of-strain and rate-of-rotation tensors across the T/NT interface in a turbulent jet with polymer additives, some insight on the additives-turbulence interaction is expected.

1.2 Objectives and contributions of the dissertation

The objectives of this thesis are enunciated on the following item list:

- Implement a viscoelastic model on a pseudo-spectral Direct Numerical Simulations (DNS) code for simulation of turbulent plane jets;
- Perform a big DNS simulation of viscoelastic turbulent plane jet;
- Compare the viscoelastic and Newtonian turbulent plane jets;
- Analyse the influence of polymer additives on the turbulent entrainment process.

1.3 Dissertation outline

This thesis is structured in six chapters.

The first and current chapter comprises an explanation about the scope of this work.

In the second chapter, a literature review of the several research areas addressed herein is presented. It starts by a general introduction to turbulence and its main features, like vorticy, coherent structures, the energy cascade and the scales involved in a turbulent flow. Attention to turbulent jets is also given, where some of the most important characteristics are explained, along with a description of the invariants.

The third chapter refers to the fundamentals of both pseudo-spectral method and the viscoelastic model, as well as details of their numerical implementation, like spatial and temporal discretization. Particular attention is given to the stability conditions required while implementing the viscoelastic model. The computational domain and boundary conditions are also presented.

In the fourth chapter, the methods concerning the verification of the code are introduced. Direct numerical simulations present in other scientific papers of the topic are compared to the numerical results obtained, in order to verify the results given by the numerical method implemented herein.

The fifth chapter presents the numerical results obtained in this work. The viscoelastic fluid simulations are compared to a Newtonian one and the T/NT interface is studied through several statistical tools. Moreover, the differences between the several simulations are highlighted and explained.

For last, chapter six presents the main conclusions of this study and also suggestions for future work.

Chapter 2

Literature review

The literature review on the subject presented in this work is divided as follows. In the first section the work related to turbulence is reviewed, refering some of the most important features of this kind of turbulent flows. The second section centers on the turbulent entrainment topic and the statistical tools used to analyse it. In the last section, an introduction to the viscoelastic fluids is presented, along with the most important conformation models used in turbulent simulations and some special attention to the model used herein (FENE-P).

2.1 Turbulence

Turbulence is present in the almost totality of the flows encountered in nature and industrial applications. It is ingrained on our universe, from large to small phenomena in a wide range of domains like geophysics, combustion [16], aircraft high lifting devices [17], chemical reactions and even common daily activities. It is, in fact, crucial to life on this planet but also essential to some industrial processes. For instance, turbulent convection currents inside the liquid Earth core generates the Earth magnetic field. The atmosphere can be thought of a giant boundary layer that redistributes water and heat around the planet, its efficiency and dynamics directly linked with its turbulent state. Inside combustion engines, turbulence plays a key role in the mixing and efficient burn of fuel. A few examples of the large range of lengthscales where turbulence can be found are given in fig. 2.1.

On the other hand, turbulence has also the property to produce some of the most beautiful events witnessed by man, fascinating and inspiring artists since the beginning of time and leaving its presence in artistic pieces worldwide, like Van Gogh and his *Starry Night* painting (fig. 2.2).

The turbulence phenomenon has long been considered of extreme importance but, despite all the significant advances in the understanding of its processes and features, it remains nowadays one of the most challenging scientific problems, eluding even a consensual definition. In 1932, the Bristish physicist Sir Horace Lamb refers to turbulence [21]:

> I am an old man now, and when I die and go to heaven there are two matters on which I hope for enlightenment. One is quantum electrodynamics and the other is the turbulent

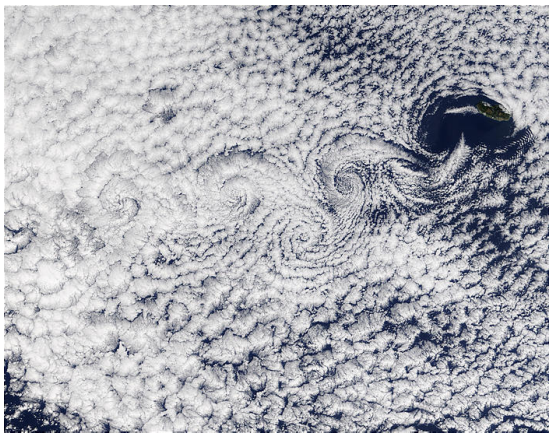

(a) Vortex Street near Madeira Island (via [18])

(b) Formula 1 Car (via [19])

Figure 2.1: Turbulent Flows of different magnitudes

Figure 2.2: Starry Night, Van Gogh (via [20])

motion of fluids. And about the former I am rather optimistic.

This sentence expresses the difficulty and the feeling shared by most researchers that have struggled valiantly to understand both the physical essence and the mathematical structure of turbulent fluid motion.

The flow behaviour of Newtonian fluids is described by the non-linear Navier Stokes equations[1]:

$$\nabla \cdot \mathbf{u} = 0, \tag{2.1}$$

$$\frac{D\mathbf{u}}{Dt} = \frac{\partial \mathbf{u}}{\partial t} + \mathbf{u} \cdot \nabla \mathbf{u} = -\frac{1}{\rho}\nabla p + \nu \nabla^2 \mathbf{u}, \tag{2.2}$$

where $\mathbf{u}$ is the velocity vector, p the pressure, ρ the fluid density and ν the kinematic viscosity. A Newtonian fluid obeys to the Newton's law of viscosity,

$$\tau_{ij} = \rho\nu \left(\frac{\partial u_i}{\partial x_j} + \frac{\partial u_j}{\partial x_i} \right), \tag{2.3}$$

[1] Navier-Stokes equations actually refer to the Navier-Stokes and the Mass conservation equations. The generalization is due to easiness of reference.

where τ_{ij} is the deformation rate of the fluid elements.

The main parameter dictating the presence of turbulence in a flow is the Reynolds number (Re), expressed by

$$Re = \frac{Ul}{\nu}, \tag{2.4}$$

where U and l are a characteristic velocity and length of the flow, respectively. This non-dimensional number was first introduced by Reynolds [22] and represents a ratio between the viscous and inviscid forces in the flow. It then expresses the flow capacity to dampen (through viscous effects) or amplify disturbances present in it.

The turbulence phenomenon arises at high Reynolds numbers due to the amplification of small scale disturbances superimposed to the flow, which quickly grow until the flow is brought into the chaotic state known as turbulence. Unlike the laminar flow regimes, where the motion of the flow usually possesses an ordely and smooth nature, a turbulent flow is characterized by chaos and randomness, perceptible on the highly irregular velocity field, associated with the presence of coherent structures of a wide range of lengthscales. Another important feature is the high level of mixing, which has a great impact on the rates of heat and mass transfer, for instance. In a laminar flow field, mixing is only consequence of molecular diffusion, but mixing rates in turbulent flows exceed in more than a couple of magnitude orders this molecular diffusion rates [23].

Despite their unpredictable behaviour, it is known that turbulent flows have some stable statistical properties [24] and that is the reason why their treatment rely on statistical methods instead of deterministic ones. Among those, mean values, root mean square (RMS), variance, probability density functions (PDFs) and correlations are some of the tools used to analyse turbulence. Spectra are also commonly used to identify dominant frequencies and wavenumbers in the Fourier space.

2.1.1 Vorticity

Vorticity is a very important quantity in turbulence and is defined by

$$\boldsymbol{\omega} = \nabla \times \mathbf{u}, \tag{2.5}$$

where $\mathbf{u}$ is the velocity vector. Incompressible hydrodynamic turbulence can be seen as a spatially complex distribution of vorticity, which advects itself in a chaotic manner. Unlike velocity, vorticity cannot be created or destroyed in the interior of a fluid and is instead generated by the presence of boundaries which introduce into the flow necessary velocities gradients, like the presence of walls (and the non-slip condition) [25]. This is a consequence of the Kelvin-Helmholtz theorem, which says that in the absence of rotational external forces, a fluid that is initially irrotational remains irrotational. An irrotational flow is defined by $\nabla \times \mathbf{u} = 0$.

The vorticity dynamics can be analysed through the curl of the momentum equation, resulting in

$$\frac{D\boldsymbol{\omega}}{Dt} = \frac{\partial \boldsymbol{\omega}}{\partial t} + \mathbf{u} \cdot \nabla \boldsymbol{\omega} = \boldsymbol{\omega} \cdot \nabla \mathbf{u} + \nu \nabla^2 \boldsymbol{\omega} = \mathbf{S} \cdot \boldsymbol{\omega} + \nu \nabla^2 \boldsymbol{\omega}, \tag{2.6}$$

where S is the strain rate tensor $\mathbf{S} = (\nabla\mathbf{u} + \nabla\mathbf{u}^T)/2$ or $S_{ij} = (\partial u_i/\partial x_j + \partial u_j/\partial x_i)/2$. The left-hand side of Eq. (2.6) is the same for both two and three dimensions and states that the vorticity is advected by the local velocity. The first term in the right-hand side is exclusive of three-dimensional flows and represents the vorticity production. The last term traduces the vorticity viscous diffusion in the flow.

The importance of that new term ($\mathbf{S} \cdot \boldsymbol{\omega}$) must be understood and to do so, a new quantity named *enstrophy* is defined as $\Omega = (1/2)|\boldsymbol{\omega}|^2 = \omega_i\omega_i/2$. The enstrophy transport equation is:

$$\frac{D\Omega}{Dt} = \frac{\partial\Omega}{\partial t} + \mathbf{u}\frac{\partial\Omega}{\partial\mathbf{x}} = \boldsymbol{\omega}\cdot\mathbf{S}\cdot\boldsymbol{\omega} + \nu(\nabla^2\Omega - |\nabla\boldsymbol{\omega}|^2) \tag{2.7}$$

or in indicial notation,

$$\frac{D\left(\frac{1}{2}\omega_i\omega_i\right)}{Dt} = \frac{\partial\left(\frac{1}{2}\omega_i\omega_i\right)}{\partial t} + u_j\frac{\partial\left(\frac{1}{2}\omega_i\omega_i\right)}{\partial x_j} = \omega_i\omega_j S_{ij} + \nu\frac{\partial^2\left(\frac{1}{2}\omega_i\omega_i\right)}{\partial x_i x_j} - \nu\left(\frac{\partial\omega_i}{\partial x_j}\right)^2. \tag{2.8}$$

The viscous part of this equation contains a diffusion term ($\nabla^2\Omega$) and an enstrophy dissipation term ($|\nabla\boldsymbol{\omega}|^2$). If one neglects for a moment this viscous terms and focuses on the inertial term in the right-hand side, results

$$\frac{D\Omega}{Dt} = 2\boldsymbol{\omega}\cdot\mathbf{S}\cdot\boldsymbol{\omega}, \tag{2.9}$$

which is the main difference between two- and three-dimensional flows. While in the latter there is a mechanism for modifying the enstrophy, in the former there is none. In three dimensions, vorticity is amplified or damped because the flow stretches or compresses the fluid particles, changing their moment of inertia and the corresponding vorticity components have to adjust. In two-dimensional flows, the stretching and compression of the particles happen in the plane of the flow, while vorticity is always perpendicular. There is never a vorticity component in the direction of the stretching and the enstrophy is conserved (in two dimensions, $D\Omega/Dt = 0$). In this way, the behaviour of two-dimensional vorticity configurations is very different than in three dimensions.

2.1.2 Coherent structures

Within a turbulent flow, even at high Reynolds numbers, some spatially organized structures of recognizable shape can be found. Their presence has attracted the attention of researchers, since they play an important role in the midst of turbulent flows and their dynamics can be understood by developing some simple mathematical models. Besides, these structures are also known to govern the transport, mixing and diffusion of mass, momentum and scalars, making their study essential to engineering applications.

In this sense, in a turbulent flow, two different coherent structures can be defined: intense vorticity structures (IVSs) and large vorticity structures (LVSs). The ISVs are defined as structures with particular strong vorticity, *i.e.*, structures composed of flow points with vorticity greater than a particularly high vorticity threshold. The characteristics of the IVSs are similar in a variety of different flows, *e.g.*, the vortex radius, axial vorticity and azimuthal velocity from the IVSs in mixing layers are similar to the values found in isotropic turbulence. Specifically, it has been reported that the radius of the ISVs is

$R \approx 5\eta$, where η is the Kolmogorov micro-scale, in isotropic turbulence, mixing layers, channel flows and jets [53].

On the other hand, the LSVs are the largest structures present in a particular flow. They are often originated in the particular instabilities from that flow and their characteristics such as the vortex core radius, length size and lifetime are deeply related to these processes. Therefore they are quite different from flow to flow. However, the dynamics of these structures share some common features with LSVs from other flows, as they consist of structures with roughly tubular shape and are approximately governed by the same inviscid laws.

Both structures have different methods of identification. For the LSVs, low pressure isosurfaces are used, while for the ISVs the Q criterion is the most common. This quantity is defined as the second invariant of the velocity gradient tensor,

$$Q = \frac{1}{2}(\Omega_{ij}\Omega_{ij} - S_{ij}S_{ij}), \tag{2.10}$$

where $\Omega_{ij} = (\partial u_i/\partial x_j - \partial u_j/\partial x_i)/2$ is the rate-of-rotation tensor. Positive values of Q define regions of high local vorticity and low rate of deformation. This quantity will be refered again in section 2.2.2, along with a more detailed explanation of the invariants.

The presence of coherence structures in isotropic turbulence was first shown by the numerical experiments of Siggia [26] and confirmed by the experimental observations of Douady *et al.* [27]. Lesieur [28] provides a narrower definition for a subgroup of these coherence structures, the *coherent vortices*. These are defined as those regions of space that:

- Vorticity ω is high enough so fluid trajectories can wind around;
- Keep a characteristic shape during a lifetime longer enough in front of their local turnover time ω^{-1};
- Have an unpredictable nature.

Coherent vortices appear in two main forms: *vortex tubes* and *vortex sheets*. The former consist of elongated tube like structures, mainly subjected to axial strain, and the latter to vorticity sheets under plain strain.

2.1.3 The energy cascade

An integral part of turbulence is the concept of *energy cascade*. The general idea was first proposed by Richardson [29], who imagined that large turbulent eddies, generated by the external forces acting on the flow, would become unstable and break into smaller ones. These would in turn break again, until the eddies became small enough to be damped by viscosity.

Later, Kolmogorov [30] introduced the concept of an energy cascade *per se*, saying the role of the break-up process is to transfer energy from large scales, where it cannot be dissipated, to the smaller ones, where it can. Energy is injected by the interaction between mean and turbulent flow into the largest eddies, whose Reynolds numbers are large if the flow is turbulent, and is transferred to the eddies that

result from their break-up. This process is inviscid and no energy is dissipated, but as the eddies become smaller with every cascade step, so do their Reynolds numbers. Eventually, the energy reaches an eddy size for which viscosity cannot be neglected any longer and it is only at that stage that the energy is dissipated (fig. 2.3). The hypothesis of Kolmogorov is that the cascade is essentially one-directional, self-similar and uniformly distributed over the flow. Energy is predominantly transferred from larger to smaller eddies and the flux of energy is independent of the eddy size at which is measured.

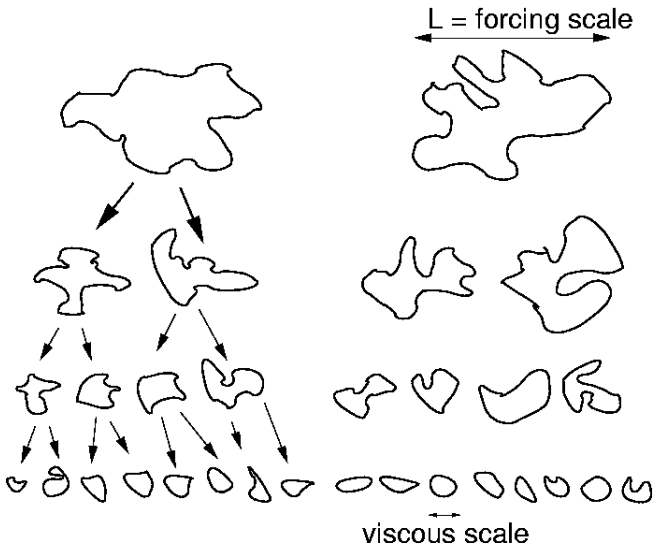

Figure 2.3: Schematic representation of the energy cascade

The energy cascade gives a global picture of the flow but, in fact, locally and instantaneously, the energy flows from the large to small scales (forward energy transfer) and also from the small to the large scales (backward energy transfer). The overall transfer energy is the difference between the two phenomena and, in most cases, it is the forward energy transfer that dominates.

One tool commonly used to evaluate how the turbulent kinetic energy is distributed across the different lengthscales of a turbulent flow is the energy spectrum. It was deduced by Obukhov [31] by formulating the Kolmogorov hypothesis in the spectral space. In this space, the eddies characteristic length scale l becomes a wave number according to $k = 2\pi/l$. The energy spectrum function represents the contribution to the turbulent kinetic energy from each eddy with wavenumber k. In isotropic turbulence it is expressed by:

$$E(k) = \frac{2}{\pi}\int_0^\infty R(r)\cos(kr)dr, \tag{2.11}$$

where $R(r) = 1/2\langle \mathbf{u}(\mathbf{x}) \cdot \mathbf{u}(\mathbf{x} + r\hat{\mathbf{e}})\rangle$, r is the distance between two points and $\hat{\mathbf{e}}$ is the unit vector. Then, the total turbulent kinetic energy results from the integration of the energy distribution $E(k)$:

$$K = \frac{1}{2}\langle \mathbf{u}^2 \rangle = \int_0^\infty E(k)dk. \tag{2.12}$$

Using dimensional analysis, the form for the energy spectrum function is

$$E = E(k, \varepsilon) = C_K \varepsilon^{2/3} k^{-5/3}, \tag{2.13}$$

where C_K is the Kolmogorov constant. Equation (2.13) is the famous *five thirds* power law and it agrees reasonably well with experimental evidence, remaining one of the bases of turbulent theory.

From the observation of a typical energy spectrum, fig. 2.4, one can conclude that the largest amount of energy in a turbulent field is carried by the scales with lower k, the larger scales. That is the reason why they are often called by energy containing eddies. On the other hand, the smaller scales contribute with a low amount of kinetic energy, being associated to the end of the energy transfer mechanism, representing the dissipative scales. Between the two ends of the spectrum, the energy is transferred from the energy containing eddies to the dissipative scales and the wavenumbers in that range are said to belong to the inertial sub-domain range.

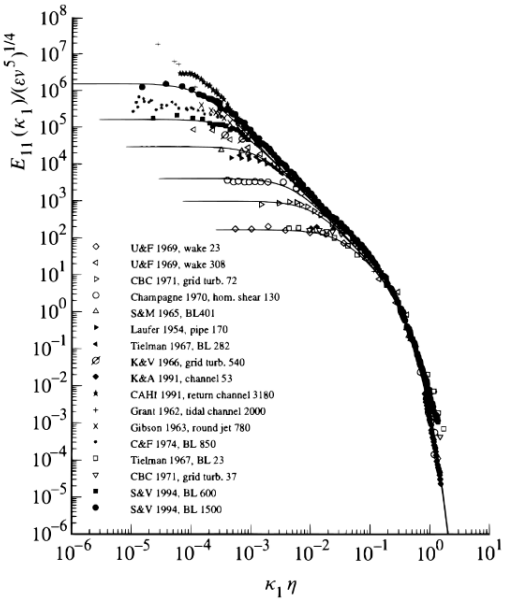

Figure 2.4: Measurements of one-dimensional longitudinal velocity spectra (symbols) and model spectra for $Re_\lambda = 30, 70, 130, 300, 600, 1500$. Experimental data culled from Saddoughi and Veeravalli (1994), Re_λ is the last number in the legend (via [32])

Kolmogorov [30] also suggested that, at sufficiently high Re, the eddies break down process causes them to loose their anisotropy and become, at the smallest scales, statistically isotropic. The boundary conditions of a turbulent flow define the shape of the larger scale eddies, whether dealing with turbulent jets, wakes or boundary layers. After being subjected to a series of instability mechanisms upon which new smaller eddies are generated, the anisotropy of the flow structures starts to slowly fade away and the resulting eddies only feel the larger scales by the energy flux arriving to them. When in this stage, the flow is *locally isotropic* and in *statistical equilibrium*. In this framework, scales belonging to the universal equilibrium range possess a number of universal characteristics and are independent from the larger scales, which is the type of flow where they exist.

2.1.4 Scales in turbulent flow

The assumptions made in the energy cascade theory are enough to estimate the inner viscous length where self-similarity ceases to hold. One starts by label an 'eddy' through a velocity difference u_l

across a distance l. Since the argument depends only on scaling similarity, like a dimensional analysis, the details of how the velocities are measured are not important for the case. The kinetic energy per unit mass of size l eddies is proportional to u_l^2 and decays in a time which can only be of order $T_l = l/u_l$, in the absence of viscous effects. The energy is transferred in the break-up process at a rate proportional to

$$\varepsilon \sim \frac{u_l^2}{T_l} = \frac{u_l^3}{l}. \tag{2.14}$$

Since the assumption is that the energy transfer is essentially an inviscid process, until the dissipation region is attained, Eq. (2.14) should also represent the average dissipation rate at the viscous scale. Equation (2.14) then leads directly to a power law for the velocity increments,

$$u_l \sim (\varepsilon l)^{1/3}. \tag{2.15}$$

It follows from Eq. (2.15) that the Reynolds number of the eddy $u_l l/\nu$ decreases as the cascade proceeds to smaller sizes, until becomes of order unity, when

$$u_l l/\nu \approx 1, \qquad l \approx \eta = (\nu^3/\varepsilon)^{1/4}. \tag{2.16}$$

The letter η stands for the Kolmogorov scale and, for distances shorter than this, viscous forces dissipate the eddies before they have time to decay into smaller ones, making the flow smooth.

Following the same procedure, the Kolmogorov velocity length scale yields

$$u_\eta = (\nu\varepsilon)^{\frac{1}{4}} \tag{2.17}$$

and then the Kolmogorov time scale results in

$$\tau_\eta = \frac{\nu}{\varepsilon}^{\frac{1}{2}}. \tag{2.18}$$

At present, the only support for these assumptions is that experimental results agree with their consequences [25], but there is no adequate theoretical proof that the same could not be achieved in a different way.

Another scale worth mentioned is the Taylor microscale. Between the large eddies scale and the Kolmogorov microscale, this intermediary scale is defined by

$$\lambda = \sqrt{\frac{u'^2}{\left\langle \left(\frac{\partial u}{\partial x}\right)\right\rangle^2}}, \tag{2.19}$$

where $u' = \left\langle u^2 \right\rangle^{1/2}$ is the root mean square value of the velocity fluctuations. The Taylor microscale lacks a clear physical meaning but it is related with several physical events found in turbulence, incorporating both small and large scale effects. It is also used to define the microscale Reynolds number as

$$Re_\lambda = \frac{u'\lambda}{\nu}. \tag{2.20}$$

Fully turbulent flow requires Re_λ to be larger than approximately 100 and it is not possible to speak of real turbulence below $Re_\lambda \approx 30$, since the instabilities needed for the cascade do not develop in that regime.

2.1.5 Turbulence in jets

Turbulent jets are part of the large group of free shear flows, which also includes wakes, mixing layers and thermal plumes. These flows are characterized by developing far away from the influence of boundaries, like walls, and usually in a quiescent environment. Examples of jets surrounding our everyday life are given in fig. 2.5.

(a) Water jets from the Three Gorges Dam (via [34])

(b) Volcano in Eyjafjallajokul (Iceland) erupting (via [35])

(c) Jet burning biofuel (via [36])

Figure 2.5: Jets in real life

The interest in study turbulent jets is related to the direct need of predicting their behaviour and influence, due to their presence on such a broad range on man made and natural contexts, but also because they are a good object of study to improve the knowledge on the physics of turbulence.

A jet consists in a source of momentum forcing its way into an ambient environment that is, for the sake of simplicity, at rest or animated of constant velocity in the same direction. This momentum spreads throughout space free from the influence of external forces and only by the action of flow internal motions. Therefore, jets evolve and develop along a preferred direction, which leads to some important features of these kind of flows: their average velocity, $\bar{u}_x$, is much higher than their transversal velocity, $\bar{u}_y$ ($\bar{u}_x \gg \bar{u}_y$), and their transversal gradients, $\partial/\partial y$, are much larger than the streamwise ones, $\partial/\partial x$

($\partial/\partial y \gg \partial/\partial x$). Another characteristic feature is the relation of scales between the shear layer thickness (δ) and the streamwise length (L), with the latter being much larger than the former ($\delta/L \ll 1$).

A characteristic common to all shear flows is the existence of a sudden change from a rotational region (turbulent), to an irrotational surrounding. This change is settled by a very controversial interface, the turbulent/non-turbulent (T/NT) interface. While the jet develops streamwise, there are important exchanges of mass, momentum and scalars through this interface, spreading out the jet. This will transmit momentum to the adjoining fluid, contaminating it with vorticity and dragging mass in a phenomena known as *turbulent entrainment*. A more detailed description of turbulent entrainment will be presented further into the text.

In order to properly quantify the jet growth and ascertain the jet boundaries, the jet half-width ($\delta_{0.5}$) is defined. It expresses the distance from the jet centreline to the location where the average streamwise velocity is half of the average centreline streamwise velocity, as can be seen in fig. 2.6 and Eq. (2.21).

$$\bar{u}_x(x, y = \delta_{0.5}) = \frac{1}{2}[\bar{u}_x(x, y = 0) - \bar{u}_x(x, y = \infty)] \tag{2.21}$$

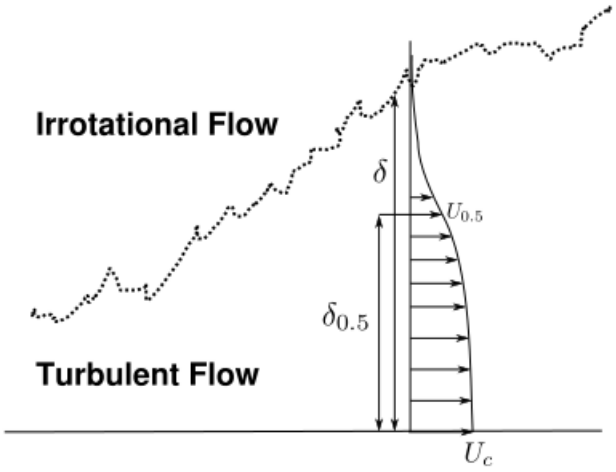

Figure 2.6: Jet half-width ($\delta_{0.5}$) in the turbulent jet (via [37])

Another important variable is the jet momentum thickness (θ), a measure of the jet momentum in relation to an inviscid ideal flow:

$$\theta(x) = \int_0^\infty \left[\frac{\bar{u}_x(x) - \bar{u}_\infty(x)}{\bar{u}_0 - \bar{u}_\infty(x)}\right]\left[1 - \frac{\bar{u}_x(x) - \bar{u}_\infty(x)}{\bar{u}_0 - \bar{u}_\infty(x)}\right] dy, \tag{2.22}$$

where $\bar{u}_\infty(x)$ is the undisturbed velocity far away from the jet, $\bar{u}_0$ the centreline velocity at the origin and $\bar{u}_x(x)$ is the local centreline velocity.

The turbulent plane jet

The turbulent plane jet designates a jet entering into the environment through a rectangular aperture of height H (fig. 2.7) and developing along the XY plane. This means that, along the spanwise direction,

the resulting initial shear layer will be virtually equal in each planar section and, consequently, the mean flow on parallel planes is statistically identical.

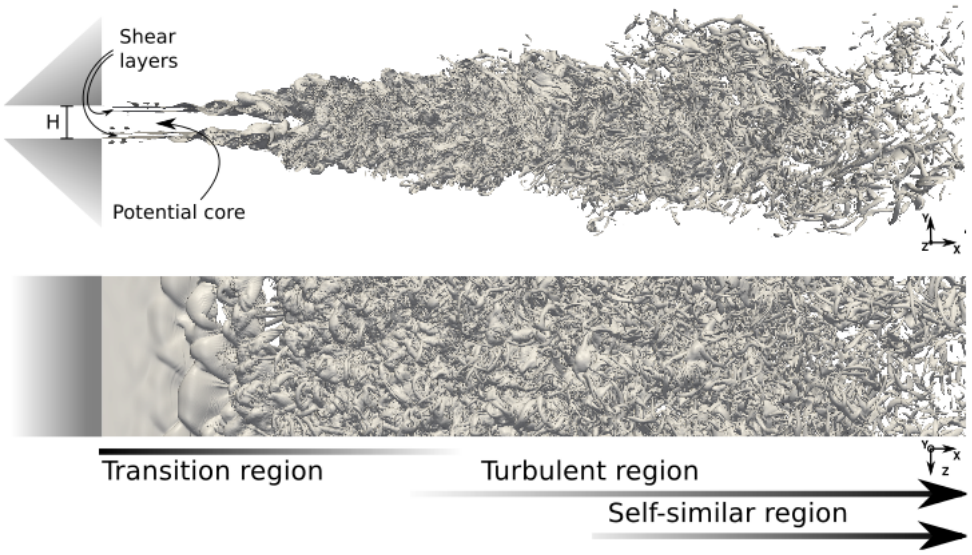

Figure 2.7: Plane jet schematic views (side and top-down) and its different regions. $|\omega|$ isosurfaces are used for illustration purposes. (via [37])

Inspecting fig. 2.7 it is possible to distinguish several regions. There are two shear layers originated by the velocity gradient between the flow incoming from the inlet aperture and the quiescent outside environment. The flow between those shear layers is called the potential core region. Here, the inital inlet profile is preserved since there are no influence of viscosity effects that created the shear layers. Then, follows the transition region, where the flow undergoes transition into a fully developed state. For last, further downstream, appears the self-similarity region, the region of space where the velocity profiles and some other variables of interest collapse after being properly scaled.

Transition to turbulence

Most real fluid flows found around the world, either in nature or engineering applications, are in turbulent state. The transition process from laminar state into a turbulent one is processed through the amplification of small, natural or externally imposed, disturbances present in the surrounding environment. The most common sources of perturbations are:

- Free stream disturbances;
- Inlet perturbations (initial conditions);
- Pressure waves from acoustic sources;
- Mechanical structures vibrations;
- Disturbances fed back from the downstream events.

Transition also has a strong dependence on the flow type and its properties. In this way, it only occurs if the aforementioned disturbances do exist and if the flow denotes receptivity to amplify them, which in general implies a high Reynolds number. However, two other situations may take place. On the one hand, the viscous effects may be strong enough to dump the small perturbations, avoiding the transition to turbulence. In this case, the Reynolds number is not sufficiently high, or is only high enough to amplify disturbances with very specific wavenumbers. On the other hand, the imposed disturbances may be very strong and the transition occurs abruptly in a phenomena known as by-pass.

Nevertheless, for the most common case, apart from the nature of the instability mechanisms (viscous or inviscid), transition to turbulence processes through four different stages (fig 2.8):

- Growth of the primary instabilities within the shear layer, due to two-dimensional disturbances;
- Appearence of secondary instabilities, enhancing the three-dimensional character of the flow structures;
- Random development of turbulent eruptions and crests;
- Degeneration into a chaotic turbulent regime.

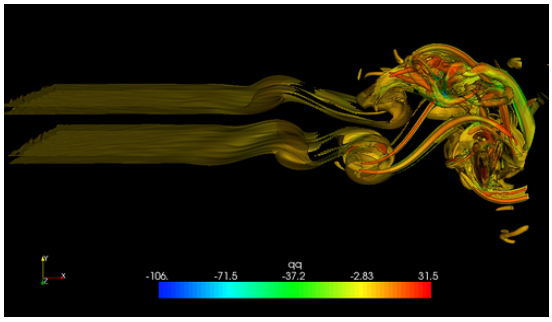

(a) Plane jet transition - side view

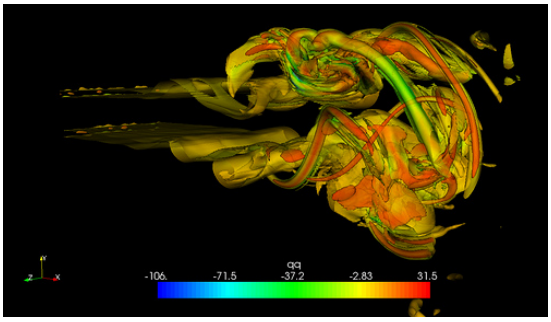

(b) Plane jet transition - angle view

Figure 2.8: Two views of a plane jet transition in a numerical simulation (via [38]): all four different transition stages can be visualized.

In jets, there are different instability length scales, each one corresponding to a distinct instability mode, which dominates the transistion process at different flow regions. Particularly in the plane jet, the two dominant instability modes are the *shear layer mode*, with a correspondent length scale of $L_{inst} = \theta$ and the *preferred* or *jet-column mode*, associated with the region starting after the end of the potential core, with a $L_{inst} = H$ [42].

Shear layer mode

The inital jet transition is related to the behaviour of the two shear layers resulting from the steep velocity gradient between the inlet velocity profile and the quiet (or relatively low, uniform velocity) outside environment. These shear layers grow through momentum diffusion towards the outside and into the potential core region. The shear layer will be much smaller than the inlet width ($\delta/H \ll 1$), for sufficiently high Reynolds numbers, becoming insensitive to curvature effects.

For plane jets, inital shear layer characteristics are very similar to the ones found in round jets and mixing layers. In the initial phase of the jet development, the Kelvin-Helmholtz instability appear. Forming in the upper and lower part of the jet, separated by the potential core region, it develops independent, but correlated to the inlet velocity profile [33]: flat profiles promote a symmetrical arrangement of primary Kelvin-Helmholtz instability ('varicose' mode), while parabolic profiles lead to asymmetric arrangements ('sinuous' mode), as can be seen in fig. 2.9.

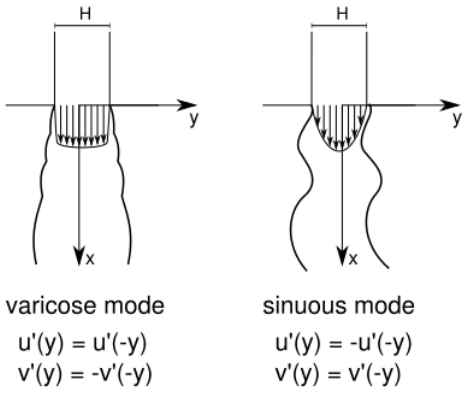

Figure 2.9: Varicose and sinuous modes.

The Kelvin-Helmholtz vortices result from perturbations in the shear layer velocity profile. A small environmental disturbance promotes a slightly small oscillation in the central streamline, reducing the area between streamlines and the outer region boundary. Therefore, the velocity increases in this thinner region due to continuity effects. This will promote a local pressure decrease, further amplifying the effect as the streamline is pulled in that direction. This cyclic process leads to a non-linear amplification of this primary disturbances. The vorticity convection, by the mean flow, will then increase the distance between the crests and troughs, shaping the flow into a characteristic wavy pattern.

Before the end of the potential core region, the shear layer mode frequency is associated with the Strouhal number given by Eq. (2.23),

$$Str_\theta = \frac{f_0 \theta_0}{U_0}, \tag{2.23}$$

where $f_0 = O(1/\theta_0)$ is the instability frequency and U_0 is the maximum inlet streamwise velocity. For the plane jet, the most usable frequency corresponds to the Strouhal number equal to $Str_\theta = 0.0165$.

Preferred mode

Near the end of the potential core region, both viscosity and curvature effects are no longer negligible and have to be taken into consideration when analysing the jet instability features. In this region, as already remarked, the instability scale is $L_{inst} = H$ and a new Strouhal number must be defined as

$$Str_H = \frac{f_p H}{U_0}, \tag{2.24}$$

where $f_p = O(1/H)$ is the preferred mode frequency, corresponding to the average passage frequency of vortices at the end of the potential core region. For this mode and at high Re, it has been found for all

jets that the Strouhal number takes values from a narrow range, $0.24 < Str_H < 0.5$ (fig. 2.10), as can be seen in several experimental (for instance, [39] and [40]) and numerical works (like [41]).

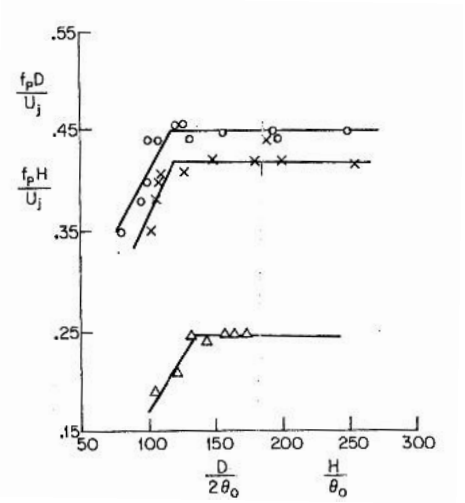

Figure 2.10: Evolution of the Strouhal number with $D/2\theta$ and H/θ ratios for round and plane jets, respectively. $\circ$ and $\times$ stands for round jet, $\triangle$ for plane jet. Source [42]

In order to adjust to the now singular shear layer, large modifications to phase and frequency of the initial instabilities waves must be performed. The shear layer adjustment is divided into two categories based on the relation of the two distinct length scales and associated frequencies. The first one, *tuned jet*, is characterized by $f_0/f_p = 2^n$, where n is an integer. The second is called *untuned jet* and $f_0/f_p \neq 2^n$. This last mode yields a more dramatic readjustment of frequency and phase from the vortices arriving from the shear layers so they fit into the jet column frequency.

Secondary instabilities

After the merging events refered before and during the longitudinal convection, secondary instabilities develop from the main vortex rollers arising from the Kelvin-Helmholtz instabilities. These spanwise disturbances show a characteristic length scale lower than that of the primary ones [43]. However, despite their smaller scale, they play a very important role in the enhancement of the three dimensional complexity of the flow, contributing to the initial emergence of smaller 3D structures, lacking preferential direction and so characteristic of fully develop turbulent flow.

Merging of the shear layers

In the plane jet, the opposite shear layers vorticity sign conduct to large scale merging events and dramatic reorganizations of the flow. At the end of the potential core region, around $x/H \simeq 4-5$, this complex and violent phenomena affects significantly the development of the jet, forming smaller anti-symmetric coherent structures.

This process evolves depending on the nature of the Kelvin-Helmholtz instabilities. On the one hand, in the varicose mode, the initial symmetric vortices will quickly give place to new and smaller anti-symmetric, fully turbulent and self-preserving structures with high three dimensional nature. These

will persist throughout the remainder of the self-similar region. The sudden change in the turbulence character is due to the upstream feedback from these restructuring events, with a frequency close to half the one of the preferred mode [33]. On the other hand, in the sinuous mode, which is less common, less dramatic events occur since the new anti-symmetric structures result from already anti-symmetric vortices.

In direct result of all this, a new frequency emerges, named similarity fundamental mode, characterized by

$$Str_{sim} = \frac{f_{sim}\delta_{0.5}}{\Delta U} = 0.11, \tag{2.25}$$

where $\delta_{0.5}$ comes from Eq. (2.21) and $\Delta U = U_2 - U_1$, with U_2 the maximum inlet velocity and U_1 the inlet co-flow velocity.

2.2 Turbulent entrainment

In contrast with their laminar siblings, turbulent shear flows have a high growth capability, absorving large quantities of non-turbulent flow. This behaviour enables the surroundings to sustain higher mixing rates of mass, energy and scalars. The growth process is called entrainment and, despite its physics are well understood for laminar regimes, where a viscous diffusion process dominates, in the turbulent side many questions remain unanswered. Several theories have been proposed, either from experiences and theoretical studies ([44], [45]), but also from new DNS simulations ([12], [46]).

There is a general consensus that the explanation for the turbulent entrainment phenomena lies in the dynamic interactions found in the interface between the turbulent and the non-turbulent flow regions: the T/NT interface. A first theory elaborated by Corrsin and Kistler [44] proposes the existence of a viscous superlayer with a characteristic width of the order of the Kolmogorov microscale (η). Knowing that vorticity could not be created among the irrotational flow, it would be diffused across that layer into irrotational flow, contaminating it, in a process similar to that happening in laminar flows. This theory is known as *nibling*.

Later, Brown and Roshko [47] found the presence of large scale organized structures in the flow near T/NT interface and added a new hypothesis for the nature of turbulent entrainment. This new idea was designated by *engulfment* and argues that turbulent entrainment is mainly driven by the large scale motions. First, large packs of irrotational fluid are involved and swallowed into the inside of the turbulent region. Then molecular diffusion is responsible for transmit vorticity and kinetic energy to the irrotational fluid elements, until a fully turbulent state is reached. This process is visible in fig. 2.11 and this explanation has become the standard one, found in many fluid mechanics textbooks. Also, several studies supported the idea of engulfment being the dominant process for turbulent entrainment, for instance [48], [49] and [50].

However, new studies ([51]–[52]) performing more detailed measurements in the T/NT region have proven that the role of engulfment in the turbulent entrainment process has been overestimated. These studies show that the amount of irrotational fluid trapped by the large scale movements only accounts for

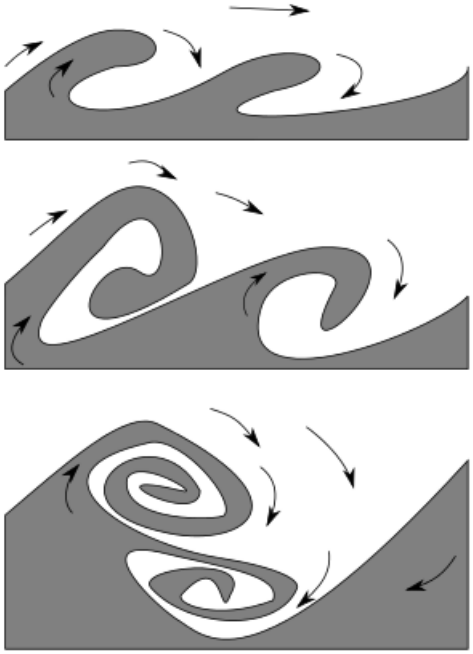

Figure 2.11: Sketch of entrainment by engulfment, inspired by Corcos and Sherman (1984). Turbulent flow in grey, arrows represent streamline segments and are not to scale. (via [37])

a small percentage of the total mass flux into the turbulent flow, approximately 10%. This result brought brack the nibling theory, where the main phenomena driving the turbulent entrainment is connected with the small scales. At large Reynolds numbers, the entrainment rate and propagation velocity of the T/NT interface relative to the fluid are independent of viscosity. Therefore, the slow process of vorticity diffusion into the irrotational region must be accelerated by interaction of velocity fields originated from eddies of all sizes, so that the overall rate of entrainment is set by large-scale parameters of the flow. This means that although the spreading is brought about by small eddies (viscosity), its rate is governed by larger eddies.

2.2.1 Turbulent/non-turbulent interface

A lot has been said about the turbulent/non-turbulent (T/NT) interface but nothing about how it is defined. That is because a consensual definiton is still open to debate. As mentioned before, between the turbulent and the non-turbulent region, a sharp, convoluted interface can be found. This interface marks an area of change in the nature of the velocity fluctuations present in the flow from vortical to irrotational. In this way, the irrotational zone is not absent of velocity fluctuations, as it would be expected. These do exist but have a irrotational character, *i.e.*, $\boldsymbol{\nabla} \times \mathbf{u}' = 0$. da Silva and dos Reis [53] have shown that dissipation measured in the irrotational region, near the interface, is connected with velocity fluctuations caused by the coherent structures nearby.

It also must be said that the T/NT interface is not the viscous superlayer mentioned by Corrsin but is made of the adjacent turbulent region near the irrotational region [51]. The superlayer would rest on the top of this interface or be part of it, as a last thin belt prior to the irrotational region and its existence

remains controversial.

So, despite all this indefinition, the topic about T/NT interface has captured the attention of a large number of researchers and several studies have been performed. Biset *et al.* [51] observed that the vorticity components undergo a sharp jump at the T/NT interface and Westerweel *et al.* [52] saw the same thing relatively to the streamwise velocity and passive scalar field across this interface. Holzner *et al.* [54] observed the existence of an intense kinetic energy dissipation outside the turbulent region near the T/NT interface and that the net effect of viscosity at that location is to cause an increase of the total enstrophy. Subsequently, da Silva and Pereira [55] noticed that it is the viscous dissipation that is responsible for this positive viscous contribution to the enstrophy while the enstrophy viscous dissipation remains negative across the jet, as expected. Also, the challenges faced by the subgrid-scale models near the T/NT interface were analysed by da Silva [56], showing that these classical models may need particular modifications near the edge of a jet if fine capturing of the Reynolds stresses at this location is needed, *e.g.*, in order to predict accurately the mixing rates near the T/NT interface of a jet.

Finally, some conflicting results regarding the thickness of the sharp vorticity jump (δ_ω) observed at the T/NT interface have been reported. The thickness of the turbulent front generated from an oscillating grid is of the order of the Kolmogorov microscale (Holzner *et al.* [54]) whereas the experimental results from round jets by Westerweel *et al.* [52] and the numerical simulations of plane jets by da Silva and Pereira [12], [57] clearly show a vorticity jump thickness at the T/NT interface of the Taylor microscale order. More recently, da Silva and Taveira [46] have been able to reconcile these reports showing that δ_ω is roughly equal to the size of the largest coherent vortices found nearby, *i.e.*, $\eta < \delta_\omega < \lambda$.

2.2.2 Invariants

The invariants are scalar quantities whose values are independent of the orientation of the coordinate system and contain information concerning the rates of vortex stretching and rotation, and on the topology and geometry of deformation of the infinitesimal fluid elements [12]. By analysing the invariants one can better understand these issues and perform a detailed characterization of the dynamics of the flow during the entrainment, using a relatively small number of variables.

The velocity gradient tensor $A_{ij} = \partial u_i/\partial x_j$ can be slipt into a symmetric and a skew-symmetric component,

$$A_{ij} = S_{ij} + \Omega_{ij}, \tag{2.26}$$

where $S_{ij} = \frac{1}{2}(\partial u_i/\partial x_j + \partial u_j/\partial x_i)$ and $\Omega_{ij} = \frac{1}{2}(\partial u_i/\partial x_j - \partial u_j/\partial x_i)$ are the rate-of-strain and rate-of-rotation tensors, respectively.

The velocity gradient tensor A_{ij} has the following characteristic equation:

$$\lambda_i^3 + P\lambda_i^2 + Q\lambda_i + R = 0, \tag{2.27}$$

where λ_i are the eigenvalues of A_{ij}. The first, second and the third invariants of the velocity tensor are

$$P = -A_{ij} = -S_{ij}, \tag{2.28}$$

$$Q = -\frac{1}{2}A_{ij}A_{ji} = \frac{1}{4}\left(\omega_i\omega_i - 2S_{ij}S_{ij}\right), \tag{2.29}$$

$$R = -\frac{1}{3}A_{ij}A_{jk}A_{ki} = -\frac{1}{3}\left(S_{ij}S_{jk}S_{ki} + \frac{3}{4}\omega_i\omega_j S_{ij}\right), \tag{2.30}$$

respectively, where $\omega_i = \varepsilon_{ijk}\partial u_j/\partial x_k$ is the vorticity field ($P = 0$ in incompressible flow).

Similarly, the invariants of the rate-of-strain tensor are defined by its characteristic equation. The independent invariants of S_{ij} are

$$Q_S = -\frac{1}{2}S_{ij}S_{ij} \tag{2.31}$$

and

$$R_S = -\frac{1}{3}S_{ij}S_{jk}S_{ki}. \tag{2.32}$$

Finally, the only invariant of the rate-of-rotation tensor is

$$Q_W = \frac{1}{2}\Omega_{ij}\Omega_{ij} = \frac{1}{4}\omega_i\omega_i. \tag{2.33}$$

It is important to mention that the invariants of S_{ij} are obtained by setting Ω_{ij} to zero in Eqs. (2.29) and (2.30), while the only invariant of Ω_{ij} is obtained by setting S_{ij} to zero in Eq. (2.29).

All of these quantities have a physical meaning. Extensive review on this topic can be found in [14], [15] and also [58], but some insight is presented here.

Starting with $Q_W = \omega_i\omega_i/4$, this invariant is related to the second invariants of A_{ij} and S_{ij} through $Q_W = Q - Q_S$. Therefore, Q_W is proportional to the enstrophy density ($\Omega^2 = \omega_i\omega_i/2$). Regions of intense enstrophy tend to be concentrated in tubelike structures in many turbulent flows such as isotropic turbulence [59], mixing layers [60] and jets [61].

The second invariant of S_{ij}, $Q_S = -S_{ij}S_{ij}/2$ is proportional to the local rate of viscous dissipation of kinetic energy since $\varepsilon = 2\nu S^2 = -4\nu Q_S$, where $S^2/2 = S_{ij}S_{ij}/2$ is the strain product. In isotropic turbulence, intense values of viscous dissipation of kinetic energy tend to be concentrated in structures with the form of sheets or ribbons [62]. On the other hand, the third invariant of S_{ij}, $R_S = -S_{ij}S_{jk}S_{ki}/3$, is proportional to the strain skewness $S_{ij}S_{jk}S_{ki}$. This invariant has two important physical meanings. It appears as part of the production term in the strain product transport equation [58],

$$\frac{D}{Dt}\left(\frac{1}{2}S_{ij}S_{ij}\right) = -S_{ij}S_{jk}S_{ki} - \frac{1}{4}\omega_i\omega_j S_{ij} - S_{ij}\frac{\partial^2 p}{\partial x_i \partial x_j} + \nu S_{ij}\nabla^2 S_{ij}. \tag{2.34}$$

As can be seen, a positive value of R_S is associated with the production of strain product (and thus of viscous dissipation), whereas $R_S < 0$ implies a destruction of strain product. Moreover, in can be shown that $R_S = -(\alpha_S^3 + \beta_S^3 + \gamma_S^3)/3 = -\alpha_S\beta_S\gamma_S$, where $\alpha_S \geq \beta_S \geq \gamma_S$ are the three eigenvalues of S_{ij} arranged in descending order. Due to incompressibility $\alpha_S + \beta_S + \gamma_S = 0$, so, $R_S > 0$ implies $\alpha_S, \beta_S > 0$, $\gamma_S < 0$ and the associated flow structure is sheetlike. If $R_S < 0$, then $\alpha_S > 0$, $\beta_S, \gamma_S < 0$, which implies

a tubelike structure.

Finally, the physical meaning of the invariants of A_{ij} depends on the sign of Q. If $Q > 0$, the enstrophy ($\Omega^2 = \omega_i\omega_i/2$) dominates over strain product ($S^2/2 = S_{ij}S_{ij}/2$), whereas if $Q < 0$, the opposite occurs. In a vortex flow, for instance, the center of the vortex is characterized by $Q > 0$, while in the region around it, $Q < 0$, implying that the strain product (and hence the viscous dissipation of kinetic energy) dominates. The meaning of R dependes on the sign of Q. If $Q \gg 0$, then $R \sim -\omega_i\omega_j S_{ij}/4$ and $R < 0$ implies a predominance of vortex stretching over vortex compression, but if $R > 0$, vortex compression dominates. On the opposite side, if $Q \ll 0$, then $R \sim -S_{ij}S_{jk}S_{ki}/3 = -\alpha_S\beta_S\gamma_S$ and, therefore, $R > 0$ is associated with a sheetlike structure, whereas $R < 0$ is connected to a tubelike structure.

The aforementioned invariantes are usually represented and analysed in joint PDFs combining two of them. The most common consist on the maps of (R, Q), (R_S, Q_S) and (Q_W, $-Q_S$). Figures 2.12(a) – 2.12(c) show sketches of each one of these maps with physical meaning associated with each particular location.

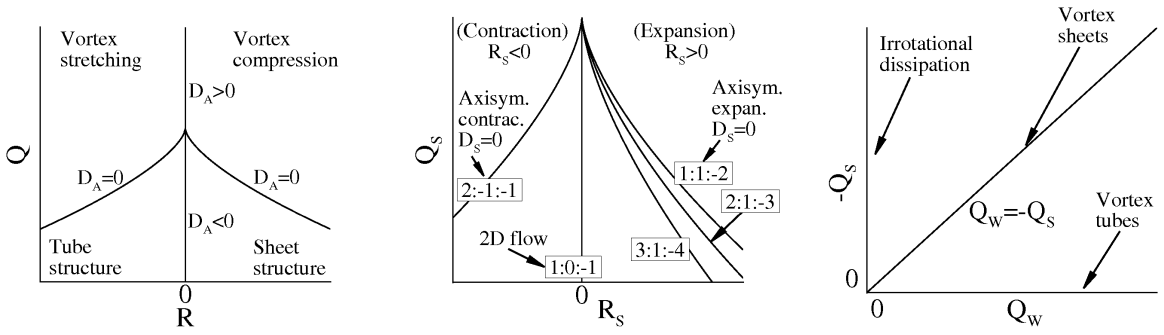

(a) (R, Q) map (b) (R_S, Q_S) map (c) (Q_W, $-Q_S$) map

Figure 2.12: Sketch of the invariant maps of (R, Q), (R_S, Q_S) and (Q_W, $-Q_S$), with the physical/topological features associated with each zone. [12]

The (R, Q) map (fig. 2.12(a)) allows to infer about the relation between the local flow topology (enstrophy or strain dominated) and the enstrophy production term (vortex stretching or vortex compression), resulting in the associated geometry of the deformation of the fluid elements (contraction or expansion). The lines labeled with D_A are defined by the discriminant $D_A = 27/(4R_A^2) + Q_A^3$, which divides the map in two regions. If $D_A > 0$, Eq. (2.27) has one real and two complex-conjugate roots, whereas if $D_A < 0$, the equation has two real distinct roots. Usually, in many turbulent flows, the (R, Q) displays a characteristic teardrop shape due to a strong (anti)correlation between R and Q in the region $R > 0$, $Q < 0$ associated to sheetlike structures, but also (not as strong) in the region $R < 0$, $Q > 0$ with a predominance of vortice stretching. These relations and the teardrop shape can be observed in isotropic turbulence [13], mixing layers [14] and channel flows [15].

On the other hand, the (R_S, Q_S) map (fig. 2.12(b)) is particularly useful to analyse the geometry of the local straining (or deformation) of the fluid elements since $R_S = -\alpha_S\beta_S\gamma_S$ and $\alpha_S + \beta_S + \gamma_S = 0$ due to incompressibility. If one defines the ratio of the second to the first eigenvalue of the rate-of-strain

tensor as $a = \beta_S/\alpha_S$, each value of a represents a line in the (R_S, Q_S) with the following expression:

$$R_S = (-Q_S)^{3/2} a(1+a)(1+a+a^2)^{-3/2}. \tag{2.35}$$

Each line is associated with a given flow geometry: $\alpha_S : \beta_S : \gamma_S = 2 : -1 : -1$ (axisymmetric contraction), $1 : 0 : -1$ (two-dimensional flow), $3 : 1 : -4$ (biaxial stretching) and $1 : 1 : -2$ (axisymmetric stretching). Once again, the discriminant for this map is defined by the line $D_S = 27/(4R_S^2) + Q_S^3$. Figure 2.12(b) shows a (R_S, Q_S) map with several lines of constant a and their associated local flow geometry. Moreover, since $Q_S = -\epsilon/(4\nu)$, large negative values of this quantity are associated with regions of kinetic energy dissipation. Generally, the (R_S, Q_S) map of many turbulent flows shows a strong prefe-rence for the zone $R_S > 0$, $Q_S > 0$, indicating a predominance of sheet structures. The most probable geometry observed corresponds to a geometry of $3 : 1 : -4$ or $2 : 1 : -3$, as seen in [13]–[15].

For last, the (Q_W, $-Q_S$) map (fig. 2.12(c)) is useful to analyse the topology related to the dissipation of kinetic energy. The vertical line $-Q_S = S_{ij}S_{ij}/2$ represents points with high dissipation but little enstrophy density and also points of strong dissipation outside and away from the vortex tubes ('irrotational dissipation'). On the other hand, the horizontal line $Q_W = \Omega_{ij}\Omega_{ij}/2$ stands for points with high enstrophy but very small dissipation as in the solid body rotation at the center of a vortex tube ('vortex tubes'). The line making $45\,^\circ$ with the vertical and horizontal lines, $Q_W = -Q_S$, represents points of both high dissipation and high enstrophy density, as occurs in vortex sheet structures. In compressible mixing layers, it has been shown that the smallest scale motions associated with the highest local values of dissipation but with relatively small amounts of the total dissipation tend to be aligned with this line [14]. However, generally, the regions of high dissipation are not correlated with regions of concentrated enstrophy [13], [15].

2.3 Viscoelastic fluids

The use of viscoelastic fluids, in particular the dilute polymeric solutions, instead of the Newtonian fluids, in turbulent flows generates drag reduction (DR) and improves the heat transfer. Researchers study DR for both practical and fundamental purposes. Practical applications include pipe flows (or other internal flow geometries) and marine vehicles, although the former has had much success with polymers than the latter. Fundamentally, studying the effects of polymers on turbulence provides valuable insight into the physics of fluid turbulence.

Since Toms's discovery, the investigation on the subject has been extensive and continuing. Figure 2.13 presents experimental data of the Darcy friction factor in turbulent pipe flow with viscoelastic fluids, (Escudier *et al.* [63]). It can be observed that a more elastic fluid, 0.125% PAA (polyacrylamide), presents higher drag reduction (lower value of the friction factor f) than a less elastic fluid, the blend of 0.09% CMC (sodium carboxymethylcellulose) and 0.09% XG (xanthan gum). The more elastic fluid

approaches the maximum drag reduction asymptote or Virk asymptote, defined by Eq. (2.36):

$$1/\sqrt{f} = 9.5 \times \log(Re_w \sqrt{f}) - 19.06. \tag{2.36}$$

The term Re_w is the wall Reynolds number, based on the local viscosity at the wall μ^w. For a better understanding of the changes, the friction factor for Newtonian fluids given by Eq. (2.37) is presented, which is used as a reference.

$$f = 0.316 \times Re^{-0.25} \tag{2.37}$$

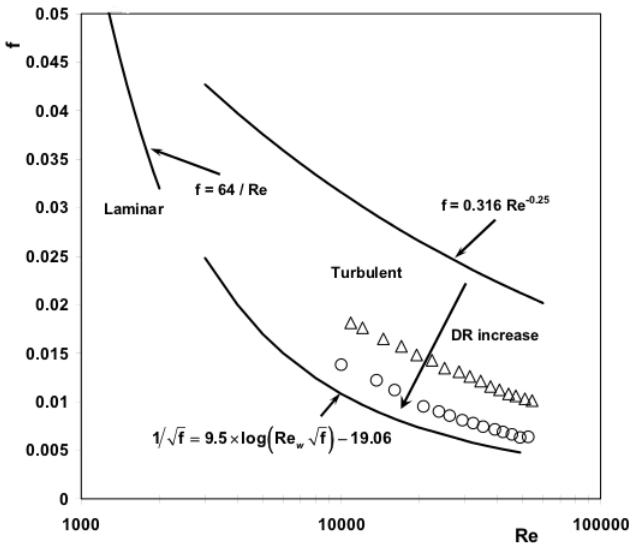

Figure 2.13: Experimental data of the Darcy friction factor in turbulent pipe flow with viscoelastic fluids: △ Blend 0.09% CMC and 0.09% XG; ∘ 0.125% PAA (via [87])

This extensive research activity produced sufficient experimental evidence to conclude that the underlying physical mechanisms of DR involve dynamical interactions between polymers and turbulence. Two results provide the basic evidence. The first is that laminar pipe flow of dilute polymer solutions shows no significant differences in the skin friction (or other flow characteristics) compared with laminar pipe flow of Newtonian fluids. The second is that, for a fixed pipe diameter, the Reynolds number, Re, at which DR is first observed depends on the number of monomers in the macromolecule. This implies an incipient interaction because, in general, turbulence dynamics depend fundamentally on Re and polymer dynamics depend fundamentally on the number of monomers [64], [65].

Detailed explanations for the onset of DR can generally be divided into two classes, based on the proposed effects of polymer stretching on the flow. The first class focuses on viscous effects ([66], [67]), while the second refers to the elastic effects ([68], [69]). The viscous explanation claims that the effect of polymer stretching in a turbulent flow produces an increase in the effective viscosity. For instance, in wall-bounded turbulent shear flows, polymers are primarily believed to be stretched just outside the viscous sublayer, in the so-called buffer layer. The strain rate and vorticity fields associated with the buffer layer are assumed suitable to cause full extension of the polymers (*i.e.*, the coil-stretch transition), leading to a corresponding large increase in the elongational viscosity [6]. It is argued that a large

increase in the effective viscosity just outside the viscous sublayer will suppress turbulent fluctuations, increase the buffer layer thickness and reduce the wall friction [70].

On the other hand, the elastic theory proposed by Tabor and de Gennes [69] postulates that the elastic energy stored by the partially stretched polymers is an important variable for DR and the increase in the effective viscosity is small and inconsequential. It also says that the onset of DR occurs when the cumulative elastic energy stored by the partially stretched polymers becomes comparable with the kinetic energy in the buffer layer at some turbulent length scale larger than the Kolmogorov scale. The usual Kolmogorov-type energy cascade is then terminated prematurely and scales below cutoff are believed to behave elastically [68]. These effects yield a thicker buffer layer and subsequent DR. Experiments [71] and numerical simulations [72] have shown that the elastic theory has merit and may be useful for predicting DR.

Despite the two classes of explanations appear fundamentally different, both have merit when compared to experimental data. At first sight, this implies an inconclusive finding, but the issue is more complicated because an elastic effect can formally be interpreted in terms of a corresponding viscous effect [72]. This is best observed and explained from model systems of a polymer, such as the FENE-P (Finite Elastic Non-linear Extensibility-Peterlin) and it will be mentioned latter.

2.3.1 Constitutive equations

Constitutive equations are relations that describe the complex rheological behaviour of fluids relating the stress tensor with the kinematic quantities. Depending on the mathematical relationship, the equation can be linear, quasi-linear or non-linear. The linear rheological constitutive equation is based on a simple principle where the response at any time is directly proportional to the value of the input signal, for example, for a fixed stress one obtain a directly proportional strain rate. The differential equations are therefore linear and the coefficients of the time differentials are defined by the material parameters, such as viscosity coefficient and rigidity modulus. These parameters are constant and not depending on variables such as strain or strain rate.

One of the first linear viscoelastic constitutive equations was the Maxwell model, where viscous and elastic behaviour are combined by the following equation

$$\boldsymbol{\tau} + \frac{\mu}{G}\frac{\partial \boldsymbol{\tau}}{\partial t} = \mu\dot{\boldsymbol{\gamma}}, \tag{2.38}$$

where $\boldsymbol{\tau}$ is the stress tensor, μ the viscosity, G the elastic modulus and $\dot{\boldsymbol{\gamma}}$ the shear rate. The linear models like the previous mentioned one, among others, can only be used as theoretical models due to their limitations, since they are unable to predict normal stresses (non-linear effect) and describe variable viscosity.

The quasi-linear constitutive models solve some of these problems by replacing the material derivatives with Oldroyd's convected derivatives. The Oldroyd-B model has the capacity to determine the first

normal coefficient and are invariant to coordinate system changes. It is defined as

$$\boldsymbol{\tau} + \lambda_1 \dot{\boldsymbol{\tau}}_{(1)} = -\mu_0 \left(\dot{\boldsymbol{\gamma}}_{(1)} + \lambda_2 \dot{\boldsymbol{\gamma}}_{(2)} \right), \tag{2.39}$$

where $\dot{\boldsymbol{\gamma}}_{(1)} = \dot{\boldsymbol{\gamma}}$, $\dot{\boldsymbol{\gamma}}_{(2)}$ is the upper convected time derivative of the deformation rate tensor,

$$\dot{\boldsymbol{\gamma}}_{(2)} = \frac{D}{Dt}\dot{\boldsymbol{\gamma}}_{(1)} - \left[(\nabla \nu)^T \cdot \dot{\boldsymbol{\gamma}}_{(1)} + \dot{\boldsymbol{\gamma}}_{(1)} \cdot (\nabla \nu) \right], \tag{2.40}$$

and $\dot{\boldsymbol{\tau}}_{(1)}$ is the upper convected time derivative of the stress tensor,

$$\dot{\boldsymbol{\tau}}_{(1)} = \frac{D}{Dt}\dot{\boldsymbol{\tau}} - \left[(\nabla \nu)^T \cdot \dot{\boldsymbol{\tau}} + \dot{\boldsymbol{\tau}} \cdot (\nabla \nu) \right]. \tag{2.41}$$

This constitutive equation contains three parameters: $\mu_0 = \mu_s + \mu_p$, the total viscosity composed of solvent and polymer components, respectively, λ_1, the relaxation time and $\lambda_2 = (\mu_s/\mu_0)\lambda_1$, the retardation time. More details of this model can be found in Bird *et al.* [64]. These models (quasi-linear) are capable of describing time-dependent flows, but are not able to make a proper representation of the rheological properties of polymer solutions. For instance, the deficiencies of constant viscosity.

To correct the limitations of the previous models, non-linear differential models have been formulated which include, among others, quadratic terms in velocity gradient and non-linear terms in stress, associated to the polymeric contribution. As an example of a non-linear constitutive model, the Giesekus model is presented:

$$\boldsymbol{\tau}_p + \lambda_1 \dot{\boldsymbol{\tau}}_{p(1)} - \alpha \frac{\lambda_1}{\mu_p} \left[\boldsymbol{\tau}_p \cdot \boldsymbol{\tau}_p \right] = -\mu_p \dot{\boldsymbol{\gamma}}. \tag{2.42}$$

There are the following parameters in this model: the polymer relaxation time λ_1, the polymeric viscosity μ_p and the dimensionless mobility factor α. The origin of this term can be traced back to the anisotropic Brownian motion and/or anisotropic hydrodynamics drag on the constituent polymer molecules [85]. The inclusion of the term $[\boldsymbol{\tau}_p \cdot \boldsymbol{\tau}_p]$ gives material functions that are more realistic than those obtained with the Oldroyd-B model, for example, capturing shear-thinning of the viscosity.

Besides the Giesekus model, there are more complex representations, where the coefficients are variable quantities depending on stress invariants. Some very important models are based on molecular kinetic theories, such as the FENE-dumbbell (finite extensive, non-linear elastic), developed to represent dilute or semi-dilute polymeric solutions, which is capable to predict the shear-thinning effect of the viscosity and of normal stress difference coefficient.

2.3.2 FENE-P model

The FENE-dumbbell is an elementary non-linear kinetic model in which the polymeric part is described by two identical beads connected through an entropic spring (fig. 2.14). The model captures two essential characteristics of a linear polymer: orientability and stretchability. These properties are essential to describe rheological properties of the polymer solution [64].

The beads are advected through the flow and deformed by the forces due to straining of the flow.

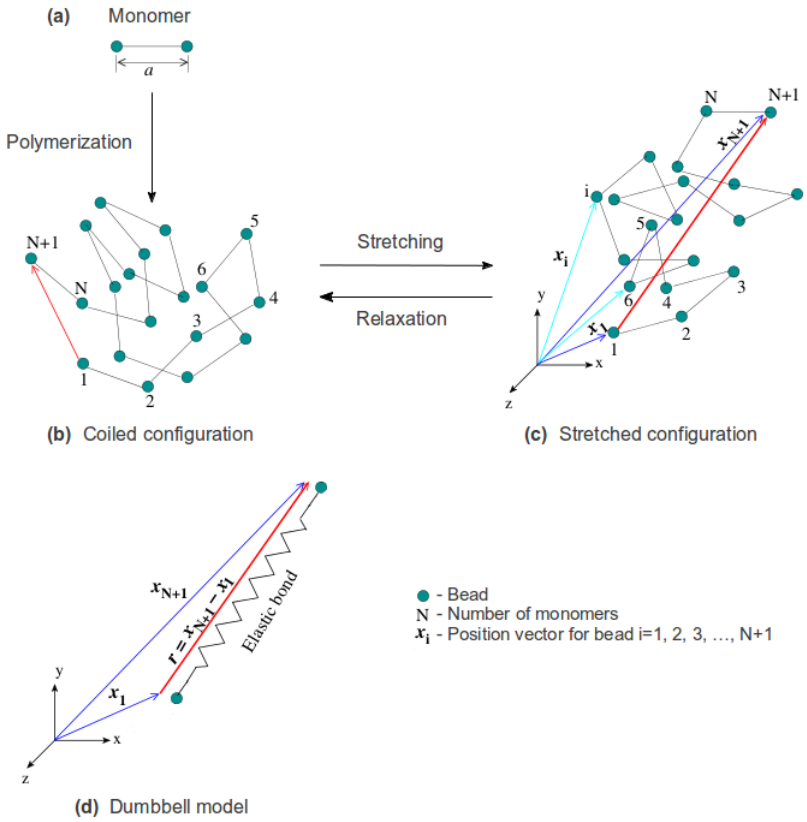

Figure 2.14: (a) Schematic of the basic structure of a monomer from a general polymer molecule. (b) Coiled (relaxed) configuration of the polymer molecule with N monomers. (c) Stretched configuration of the polymer molecule. (d) Elastic dumbbell model which only takes into account the dumbbell connector vector $\mathbf{r}$. (via [85])

Advection is related to the motion of the center of mass of the dumbbells, while deformation changes the dumbbell configuration, *i.e.*, the orientation and the separation distance of the beads. Each bead of a dumbbell is presumed to experience three forces [85]:

- a hydrodynamic drag force which is modeled by the Stokes law;
- a Brownian force due to thermal fluctuations in the liquid which makes the bead move in an irregular manner;
- an intramolecular force resulting from the elastic spring in the dumbbell.

The polymeric dynamics are then described by the evolution of the vector $\mathbf{r}$ that connects the two beads, as can be seen in fig. 2.14.

The polymer contribution $\boldsymbol{\tau}_p$ to the stress tensor is given by

$$\boldsymbol{\tau}_p = n \left\langle \mathbf{r}\mathbf{F}^c \right\rangle - nkT\mathbf{I}, \tag{2.43}$$

with n as the dumbbell number density, k as the Boltzmann constant, T as the absolute temperature, $\mathbf{F}^c$ as the force of the spring, $\mathbf{r}$ as the separation vector between two beads and $\mathbf{I}$ as the identity matrix. The angular brackets denote the configuration space average. The first term on the right-hand side

(RHS) accounts for the contribution from the intramolecular potential and the second term represents the motion of the beads [64].

The spring force $\mathbf{F}^c$ is defined, for a single FENE dumbbell, as

$$\mathbf{F}^c = \frac{H}{1 - r^2/r_0^2}\mathbf{r}, \tag{2.44}$$

where H is the spring constant, $r^2 = \mathbf{r} \cdot \mathbf{r}$ is the square of separation distance between two beads and r_0 the maximum spring length.

However, it is not possible to solve directly Eq. (2.43) due to high computation effort. For this reason, simplifications were necessary and it was on this context that the most known approximation appeared, the FENE model with the Peterlin closure (FENE-P). It consists in pre-averaging the non-linear spring law as

$$\mathbf{F}^c = \frac{H}{1 - \langle r^2 \rangle / r_0^2}\mathbf{r}. \tag{2.45}$$

Introducing Eq. (2.45) into Eq. (2.43) a closed form of polymer stress is obtained

$$\boldsymbol{\tau}_p = nH\frac{\langle \mathbf{r}\mathbf{r}^T \rangle}{1 - \langle r^2 \rangle / r_0^2} - nkT\mathbf{I}, \tag{2.46}$$

where $\mathbf{r}$ is a column vector.

The main difficulty presented by this model is the configuration space average calculation, for which it is necessary to solve an extra equation. Derivated from diffusion equation and based in a distribution function [64], the transport equation for $\langle \mathbf{r}\mathbf{r}^T \rangle$ yields:

$$\frac{D\langle \mathbf{r}\mathbf{r}^T \rangle}{Dt} = \frac{\partial \langle \mathbf{r}\mathbf{r}^T \rangle}{\partial t} + \mathbf{u} \cdot \nabla \langle \mathbf{r}\mathbf{r}^T \rangle = \langle \mathbf{r}\mathbf{r}^T \rangle \cdot \nabla\mathbf{u} + \nabla\mathbf{u}^T \cdot \langle \mathbf{r}\mathbf{r}^T \rangle - \frac{\langle \mathbf{r}\mathbf{r}^T \rangle}{\lambda_p(1 - \langle r^2 \rangle / r_0^2)} + \frac{4kT}{\zeta}\mathbf{I}, \tag{2.47}$$

where ζ is the Stokes friction coefficient of the bead and $\lambda_p = \zeta/4H$ is the characteristic relaxation time of the dumbbell. The first two terms on the RHS of Eq. (2.47) represent deformation (stretching and rotation of the dumbbell) by hydrodynamic forces and arise due to the difference in local fluid velocity at each bead of the dumbbell. The third term is due to elastic retraction of the spring and the last term models Brownian motion [85].

A proper non-dimensionalization of Eq. (2.47) is required. So, an appropriate characteristic length scale is the trace of Eq. (2.47) at long times (neglecting the time derivative) and in the absence of flow, resulting in the equilibrium length $\langle r^2 \rangle_{eq}$:

$$\langle r^2 \rangle_{eq} = \frac{\frac{3kT}{H}}{1 + \frac{3kT}{Hr_0^2}}. \tag{2.48}$$

Then, $\langle \mathbf{r}\mathbf{r}^T \rangle$ is non-dimensionalized by $\langle r^2 \rangle_{eq}$ and a conformation tensor is defined as follows

$$\mathbf{C} = \frac{\langle \mathbf{r}\mathbf{r}^T \rangle}{\frac{1}{3}\langle r^2 \rangle_{eq}}. \tag{2.49}$$

Substituting Eq. (2.49) into Eq. (2.47) yields the following transport equation for the conformation tensor [2]:

$$\frac{D\mathbf{C}}{Dt} = \frac{\partial \mathbf{C}}{\partial t} + \mathbf{u}\cdot\nabla\mathbf{C} = \mathbf{C}\cdot\nabla\mathbf{u} + \nabla\mathbf{u}^T\cdot\mathbf{C} - \frac{L^2}{\lambda_p(L^2-3)}\left[f(R)\mathbf{C}-\mathbf{I}\right], \tag{2.50}$$

where

$$L^2 = \frac{r_0^2}{\frac{1}{3}\left\langle r^2\right\rangle_{eq}} \tag{2.51}$$

is the ratio of square of the maximum separation distance between the beads to the equilibrium distance. The term $f(R)$ is designated by *Peterlin function* and is defined as

$$f(R) = \frac{L^2-3}{L^2-R^2}, \tag{2.52}$$

where R^2 is the non-dimensional polymer stretch,

$$R^2 = \frac{r^2}{\frac{1}{3}\left\langle r^2\right\rangle_{eq}} = \frac{\mathbf{r}\cdot\mathbf{r}}{\frac{1}{3}\left\langle r^2\right\rangle_{eq}} = Tr(\mathbf{C}). \tag{2.53}$$

The function $f(R)$ arises from the spring force $\mathbf{F}^c$ in Eq. (2.45), that diverges as $R \to L$, preventing non-dimensional length from extending beyond L.

For last, the polymer stress, Eq. (2.46), can be rewritten in terms of $\mathbf{C}$, by using Eqs. (2.49), (2.48) and (2.51):

$$\boldsymbol{\tau}^p = nkT\left[f(R)\mathbf{C}-\mathbf{I}\right]. \tag{2.54}$$

In the FENE-P model, the polymer is characterized by three parameters: the relaxation time λ_p, the lenght parameter L and the parameter nkT which determines the polymer concentration. This quantity is related to the viscosity ratio $\beta = \mu_s/(\mu_s+\mu_p)$, where μ_s and μ_p are the solvent and polymer viscosities respectively. According to Wedgewood and Bird (via [85]), the relation between β and nkT is

$$\mu_p = (1-\beta)(\mu_s+\mu_p) = nkT\lambda_p\frac{b}{b+3} \approx nkT\lambda_p, \tag{2.55}$$

where $b = Hr_0^2/kT = L^2-3$. Generally b is very large in polymeric solutions so, $b/(b+3)\approx 1$. For a fixed relaxation time λ_p, the parameter β is proportional to a polymer concentration n and thus is considered a concentration parameter.

Introducing Eq. (2.55) in Eq. (2.54) gives the polymer stress as

$$\boldsymbol{\tau}^p = \frac{\mu_p}{\lambda_p}\left[f(R)\mathbf{C}-\mathbf{I}\right]. \tag{2.56}$$

Also, noting that

$$\frac{b}{b+3} = \frac{L^2-3}{L^2} \approx 1, \tag{2.57}$$

[2] The step-by-step deduction of this equation is presented in Appendix A.

the transpot equation for the conformation tensor $\mathbf{C}$, Eq. (2.50), takes the form:

$$\frac{D\mathbf{C}}{Dt} = \frac{\partial \mathbf{C}}{\partial t} + \mathbf{u} \cdot \nabla \mathbf{C} = \mathbf{C} \cdot \nabla \mathbf{u} + \nabla \mathbf{u}^T \cdot \mathbf{C} - \frac{1}{\lambda_p} \left[f(R)\mathbf{C} - \mathbf{I} \right]. \tag{2.58}$$

The issue of whether the FENE-P model is an adequate representation of the FENE model in the context of turbulent flow has also been investigated by Zhou and Akhavan [73]. The conclusion was that the model was accurate in steady state, incurring in some errors at transient elongational flows. The limitations are primarily related to the description of a polymer molecule. Usually consisting of $N \approx 10^5$ monomers, a polymer molecule is reduced to a single dumbbell. Therefore, higher order moments necessary for capturing more realistically rheological properties of a polymer solution are not included. In addition, dumbbell models do not incorporate polymer-polymer interactions, which can be important even for dilute polymer solutions.

Despite its inherent limitations, FENE-P model has predicted results, for different aspects of drag reduction phenomenon, that are qualitatively consistent with experiments. Besides, due to high computational cost associated with the stochastic models (FENE and FENE-P chain), is the only viable choice for high resolution turbulent flows at present.

For last, some insight on the statement that one can formally interpret the influence of polymer stretch on the flow as either elastic effect or a viscous effect. Within the framework of the FENE-P model, the elastic energy stored by a stretched polymer is proportional to the trace of the conformation tensor, $Tr(\mathbf{C}) = C_{xx} + C_{yy} + C_{zz}$ [72]. If the problem is approached from the elastic theory perspective, the transport equation for the elastic energy can be studied to understand the energy transfer between the polymers and the flow [72]. Alternatively, by taking the viscous theory point of view, Benzi *et al.* [86] found that an important component of the conformation tensor is C_{yy}, which appears in the momentum and kinetic energy equations as an effective viscosity.

Chapter 3

Numerical tools

3.1 Direct numerical simulations

Direct numerical simulations (DNS) consist in computing directly the Navier-Stokes equations without any kind of modeling assumption and have become one of the most important and useful tools in the study of turbulent flows. Orszag and Patterson [74] performed a very basic simulation of isotropic turbulence, which allowed to demonstrate how computational methods could be used to large scale simulations of three-dimensional turbulence, despite the rudimentary resolution used.

Nowadays, cautious numerical simulations of the Navier-Stokes equations are just a different kind of experiment and there is no reason to expect less realism than laboratory data [75]. Some of their drawbacks, for instance the artificial nature of some boundary conditions, are no worse than the artificial nature of the walls in a wind tunnel and both of these can be supressed by careful design. Simulations and experiments are equally valid idealizations against which one can test theories and designs. In many ways, simulations are in general better characterized than experiments, since they do not usually suffer from ambiguities regarding boundaries, inlet or initial conditions.

On the other side, once a flow has been sucessfully simulated, it can be studied more thoroughly than in a laboratory experiments. While laboratory results are often constrained by the instrumentation technology, these computational numerical experiments allow easier access to all the flow features, being limited by the ability of the researcher to ask the right questions.

Numerical simulations of turbulent flows

The large majority of flows, either natural or man made, develop at high Re and in a turbulent state. Their simulation is challenging, as no general mathematical solution for the Navier-Stokes equations exists and the recourse to numerical approaches is a need. Unfortunately, the stiff coupling of the differential equations to solve, associated with the increase of the range of scales present in these flows, heavily limits the flow geometry complexity and Re achievable in simulations.

From the several numerical simulation tools available, DNS is the most powerfull, since it solves the full Navier-Stokes equations without any simplification. It allows full knowledge of the flow characteristic

variables, like velocity and pressure, as function of time and space. However, to capture all the flow scales, down to the order of the Kolmogorov microscale ($O(\eta)$), DNS is quite expensive in terms of CPU and memory: the value of the Kolmogorov microscale decreases with increasing Re, leading to an increase in grid size so a proper resolution can be kept. For instance, a simulation with $Re_\lambda \approx 3000$ or $Re_\lambda \approx 10^4$, like in a boundary layer of a commercial airplane or in an atmospheric boundary layer [76], a full DNS would require more than 10^{15} and 10^{18} points, respectively.

This last aspect is directly connected with the amount of memory required to carry through a simulation. Besides, the need to resolve with accuracy the small scalles also rules out the use of large time steps in the time advancement scheme. So, increasing the resolution will then decrease the allowable time step to be used and consequently the simulation running time needed to obtain a solution increases [32].

However, for most engineering problems, it is not necessary to possess the full details of a flow. The engineering computation of turbulent flows relies on simpler descriptions: instead of solving for the instantaneous values, the statistical evolution of the flow is the main objective. This approach is the basis for methods like Reynolds-Averaged Navier-Stokes (RANS), Large Eddy Simulation (LES) or Detached Eddy Simulation (DES). In RANS, one-point moments like mean velocity and turbulent kinetic energy are calculated. In LES, the large energy containing scales are directly calculated from the Navier-Stokes equations while the small scales are obtained through some model. For last, DES uses RANS near the wall and a LES methodology far from the wall, lying somewhere between both methods. Yet, statistical descriptions suffer from the problem of closure, *i.e.*, the equations describing the statistical evolution of the flow contain terms that cannot be obtained from the Navier-Stokes equations and therefore require modeling. As the complexity of the computed flow increases, more complex and improved turbulence models must be implemented. This search for better turbulence models and better parameterization of the turbulence is what drives most turbulence research and DNS proves itself as a tool in this endeavor. One of the roles of DNS is then to help the development, perfecting and validation of such less demanding methods, while contributing to the expansion of knowledge about fundamental physics related with turbulent phenomena.

Being computationally intensive, the range of flows simulated using DNS has naturally expanded with the growth of computer capabilities. The first DNS simulations were done in the early 1970s at the National Center for Atmospheric Research by Orszag and Patterson [74], an homogeneous isotropic turbulence (HIT) simulation with 32^3 collocation points and $Re_\lambda = 35$. Almost four decades later, Kaneda and Ishihara [77] reached $Re_\lambda = 1200$ in an HIT simulation, using 4096 collocation points, a feat that some would have thought impossible some decades ago. Nevertheless, HIT simulations are the most straightforward in the DNS domain, since they lack some of the numerical difficulties and challenges found on non-homogeneous flows that also have occupied the attention of the turbulence community. Growth in Re and resolution for these other type of flows has not been so generous comparatively to HIT simulations [78].

Numerical simulations of dilute polymer solutions

As mentioned before, the availability of increased computer power has offered an important research alternative by providing the means for direct numerical simulations. For the most part, the DNS have provided useful information about the molecular conformation of polymeric solutions and on the corresponding rheological properties, confirming the relevance of the extensional effects on the turbulence. Others initial investigations were not self-consistent as they only solved the constitutive equation, usually the FENE-P model, for fixed Newtonian kinematics. This strategy, adopted by Hanratty and co-workers (via [87]), was important in a way that gave insight into the evolution of the molecular configurations and the corresponding fluid properties. One of their main findings was the large molecular extensions in the viscous sublayer but not significant molecular extensions in the buffer layer.

For viscoelastic fluids there is, however, an important difficulty when comparing to Newtonian DNS: *a priori*, one does not know for sure what is the correct rheological constitutive equation for a specific fluid. Even so, the DNS techniques are supplying useful information that allows researchers a better choice in terms of constitutive equation, and more importantly, to develop closures more accurately for classic models or for new turbulence models. In general, numerical simulations use constitutive equations derived from modeling the polymer molecule as two beads connected by an elastic spring (a single dumbbell). The polymer model most often implemented is the FENE-P model, although there are competing models (*e.g.*, FENE, Oldroyd-B). This one is prefered because it accounts for the finite extensibility of the molecule and uses a simple second-order closure model in the equation for the polymer stress [6]. Also, it reduces numerical instabilities and consequently computational costs. The limitations of the model are primarily a consequence of the closure approximation (higher-order moments are not accounted for) and the fact that a polymer molecule consisting of typically $N \approx 10^5$ monomers has been reduced to a single dumbbell. In addiction, polymer-polymer interactions are not covered by the model, important even for dilute polymer solutions in which polymers have been found to organize into supermolecular structures [6].

More recently, many researchers have carried out DNS for forced HIT (FHIT) and decaying HIT (DHIT) to study the interaction between polymer additives and turbulence. Some important results were obtained, but were mainly focused on the drag reduction (DR) phenomenon and the characteristics of HIT with polymer additives [4]. However, how the flow structures interact with polymer microstructures has still not been investigated in detail.

3.2 Governing equations

This work has the purpose of study the additives-turbulence interaction by DNS. Their behaviour is described by the unsteady, incompressible Navier-Stokes equations for mass conservation (Eq. (3.1)) and linear momentum (Eq. (3.2)), along with the conformation tensor evolution equation (Eq. (3.3)). The fluid rheology, described by the FENE-P model, introduces an extra stress to the Navier-Stokes

equation (3.2):

$$\nabla \cdot \mathbf{u} = 0; \tag{3.1}$$

$$\frac{\partial \mathbf{u}}{\partial t} + \mathbf{u} \cdot \nabla \mathbf{u} = -\frac{1}{\rho}\nabla p + \frac{1}{\rho}\nabla \cdot \mathbf{T}^{[s]} + \frac{1}{\rho}\nabla \cdot \mathbf{T}^{[p]}; \tag{3.2}$$

$$\frac{\partial \mathbf{C}}{\partial t} + \mathbf{u} \cdot \nabla \mathbf{C} = \mathbf{C} \cdot \nabla \mathbf{u} + \nabla \mathbf{u}^T \cdot \mathbf{C} - \frac{1}{\lambda_p}\left[f(R)\mathbf{C} - \mathbf{I}\right]. \tag{3.3}$$

The above equations (3.1 – 3.3) are valid at each point of a cartesian reference system with coordinates $\mathbf{x} = (x, y, z)$ and at the time instant t. Also, $\mathbf{u}(\mathbf{x}, t)$ is the velocity vector $\vec{u} = (u, v, w)$, $p(\mathbf{x}, t)$ is the local pressure field, ρ is the fluid density, $\mathbf{T}^{[s]} = 2\rho\nu^{[s]}\mathbf{S}$ is the Newtonian stress tensor due to the solvent, $\nu^{[s]}$ is the solvent kinetic viscosity and $\mathbf{S} = (\Gamma_{ij} + \Gamma_{ji})/2$ is the rate of strain tensor, with $\nabla \mathbf{u} = \Gamma_{ij} = \partial u_j / \partial x_i$ and $\nabla \mathbf{u}^T = \Gamma_{ji}$. Moreover $\mathbf{T}^{[p]} = (\rho\nu^{[p]}/\lambda_p)(f(R)\mathbf{C} - \mathbf{I})$ is the additional elastic stress tensor due to polymers, $\nu^{[p]}$ is the polymer viscosity, λ_p is the polymer relaxation time, $\mathbf{C}$ is the polymer conformation tensor and $\mathbf{I}$ is the unit tensor. In the FENE-P model, $f(R) = (L^2 - 3)/(L^2 - R^2)$ ensures the finite extensibility, where $R = \sqrt{trace(\mathbf{C})}$ and L are the extension length and the maximum possible extension of polymers, respectively.

The polymer viscosity $\nu^{[p]}$ is obtained from a dimensionless number representing the polymer solution concentration:

$$\beta = \frac{\mu^{[s]}}{\mu^{[s]} + \mu^{[p]}} = \frac{\nu^{[s]}}{\nu^{[s]} + \nu^{[p]}}. \tag{3.4}$$

Furthermore, the flow is also characterized by the Reynolds number Re, a non-dimensional parameter that gives the ratio between inertial and viscous forces and consequently quantifies the relative importance of these two types of forces for any given flow conditions:

$$Re_{L_c} = \frac{U_c L_c}{\nu}. \tag{3.5}$$

In Eq. (3.5), U_c is the characteristic flow velocity and L_c is the characteristic length scale. For this work, $U_c = U_0$ is the maximum streamwise velocity and L_c is equal to the size of the inlet aperture, H.

The computational domain consists in a box with dimensions L_x, L_y and L_z in directions x (streamwise), y (normal) and z (spanwise), respectively. Periodic boundary conditions are assigned to all the three directions.

3.3 Numerical code philosophy

There are two main different philosophies in direct numerical simulations: the spatial simulation and the temporal simulation, which was the approach followed in the code development. The main difference between the two comes from the fact that in a temporal simulation, periodic boundary conditions are used on boundaries which are normal to the main (streamwise) flow direction, whereas in a spatial one, these same boundaries are treated as inlet and outlet conditions.

In the spatial approach, the flow enters the computational box through the inlet conditions, evolve

along the domain, where all the flow features are to be studied, and leaves. In this philosophy, the computational domain must contain the whole entire region of interest, and therefore a very large region has to be discriminated. This discretization leads to extremely elevated computational costs, both in memory and computational time. Moreover, in a spatial simulation, special care has to be taken regarding the inlet and outlet conditions, which are in general very difficult to design. The inlet of the computational box has to mimic a realistic initial flow condition, meaning that initial velocities must be prescribed as close as possible to a solution of the Naver-Stokes equations. The outlet condition has to allow for a 'natural' exit of the flow, so that the coherent structures can exit the domain without being influenced by unnatural perturbations which may arise from numerical approximations.

On the other hand, for temporal simulations, just a small portion of the region to be studied has to be discretized. As a consequence, it needs a smaller number of points compared to a spatial simulation. So, a temporal simulation can be understood as a moving computational domain that follows the fluid as it moves along the streamwise direction. The main drawbacks are related to the periodic boundary conditions that do not allow for the natural growth of the perturbations during a transitional process. Indeed, some of this instabilities growth is connected to the feedback phenomena. Small downstream perturbations affect, through the pressure field, the upstream flow region, thus increasing the growth of the perturbations in that location. Due to this, temporal simulations are known to predict poorly the correct shear layer evolution during early turbulent stages. Plus, another disadvantage in the use of this approach is that no rigorous comparisons with experimental data can be performed. However, the flow field in the fully developed turbulent state, which is the region of interest for the present study, is to a great extent independent from the transitional process details [43]. In temporal simulations, also Kelvin-Helmholtz rollers and streamwise structures, along with other coherent structures typical of the plane jets, are well captured. Hence, this makes the temporal simulations useful to analyze the flow features of a turbulent jet at the far-field and thereby the features of the turbulent entrainment mechanisms.

In short, despite its limitations, the use of temporal simulations is justified by the fact that it has been proven to be sufficiently accurate to obtain a valid solution of the Navier-Stokes equation and therefore allowing for a correct analysis on the turbulent entrainment mechanisms, occurring at the fully developed turbulent state. Direct numerical simulations of temporal evolving plane jets were carried out by Akhavan *et al.* [79] and da Silva and Pereira [80]. Stanley *et al.* [16] and da Silva and Metáis [61] performed DNS of spatial evolving plane jets.

3.4 Spatial discretization

The numerical code applied herein use pseudo-spectral schemes to approximate derivatives along all the directions of the computational domain. However, for the conformation tensor equation a finite difference method is used instead, since spectral and other high-order schemes are not suitable to solve it, incurring in numerical instabilities. Follows a brief introduction to both methods.

3.4.1 Pseudo-spectral schemes

The numerical code makes use of pseudo-spectral schemes to approximate the derivatives along all the directions. They have a high-level of accuracy and, for the same resolution, a computational cost proportional to $n_x \log_2 n_x$, quite low comparing with other numerical methods [81]. Due to all this, these schemes are in a proeminent position for answering DNS needs [82], despite the limitation to the treatment of periodic flows.

The Fourier transform forms the basis for the pseudo-spectral codes. It is a mathematical tool that allows to represent temporal functions in terms of frequencies and spatial functions in terms of wavenumbers. One of the most important properties is the fact that the derivatives in the physical space become simple multiplications in the Fourier space. This is the main reason for the high accuracy of this method and consequently its common use in spatial discretization. On the other side, multiplications turn out into convolution products, a very complex operation, reason why all products within the numerical code are performed in the physical space.

Besides it also must be mention that, when dealing with computational methods, it is not possible to represent continuous functions due to the finite grid nodes. Thus discrete Fourier transforms must be employed. Given a periodic flow variable, $\phi(x, y, z, t)$, the three-dimensional discrete Fourier transform can be written as

$$\hat{\phi}(k_x, k_y, k_z, t) = \sum_{m=0}^{\frac{n_x}{2}-1} \sum_{n=0}^{\frac{n_y}{2}-1} \sum_{p=0}^{\frac{n_z}{2}-1} \phi(x, y, z, t) e^{-\mathrm{i}(k_x x + k_y y + k_z z)}, \tag{3.6}$$

where (k_x, k_y, k_z) are the Fourier wave numbers defined by

$$k_x = \frac{2\pi}{L_x} m \qquad k_y = \frac{2\pi}{L_y} n \qquad k_z = \frac{2\pi}{L_z} p, \tag{3.7}$$

with L_x, L_y, L_z being the spatial dimensions along the x, y, z directions and n_x, n_y and n_z the number of collocation points along those same directions, respectively.

The inverse Fourier transform can also be easily obtained:

$$\phi(x, y, z, t) = \frac{1}{n_x n_y n_z} \sum_{m=0}^{\frac{n_x}{2}-1} \sum_{n=0}^{\frac{n_y}{2}-1} \sum_{p=0}^{\frac{n_z}{2}-1} \hat{\phi}(k_x, k_y, k_z, t) e^{\mathrm{i}(k_x x + k_y y + k_z z)}. \tag{3.8}$$

Every kind of discretization has an error associated. In this way, it is interesting to analyze in the Fourier space the discretization error with different numerical schemes [81], [43], namely the one used in this work. To do that, a simple periodic function, for instance $f(x) = e^{\mathrm{i}kx}$, is chosen. The first derivative with a 2nd order central difference scheme is

$$\frac{\delta e^{\mathrm{i}kx}}{\delta x} = \frac{e^{\mathrm{i}k(x+\Delta x)} - e^{\mathrm{i}k(x-\Delta x)}}{2\Delta x} = \mathrm{i}\frac{\sin(kx)}{\Delta x} e^{\mathrm{i}kx}. \tag{3.9}$$

Knowing that the analytical first derivative is $f'(x) = \mathrm{i}k e^{\mathrm{i}kx}$, a 2nd order central difference scheme is

equivalent to replace the exact wavenumber by a different effective one

$$k_{eff} = \frac{\sin(kx)}{\Delta x} \tag{3.10}$$

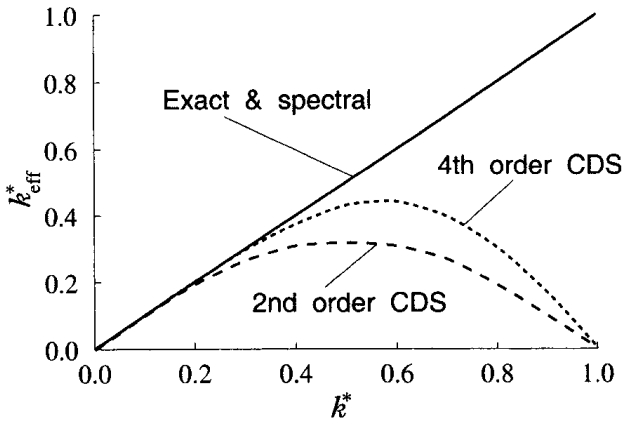

Figure 3.1: Effective wavenumber for several discretization methods non-dimensionalized by k_{max}. (via [81])

Applying a similar procedure to other schemes, one can obtain the relation between their k_{eff} and the exact one. The results obtained for several methods are shown in fig. 3.1, normalized by $k_{max} = 2\pi/\lambda_{min} = 2\pi/2\Delta x = \pi/\Delta x$, which is the maximum resolved wavenumber for a grid mesh with a resolution of Δx. From the results, it is possbile to see that the spectral scheme is the only that allows to calculate the exact derivative, whereas the remaining methods give a poor aproximation if the wavenumber is larger than half of the maximum value. Spectral methods yield an error that decreases more rapidly than any power of the grid size as the latter goes to zero [81]. However, this behaviour is obtained only when enough points are used (the definition of enough depends on the function). For small numbers of grid points, spectral methods may actually yield larger errors than finite difference methods.

Therefore, to obtain the advantages of the spectral methods (pseudo-spectral included), the functions must be periodic and the grid points uniformly spaced. Simulation of turbulence in geometrically simple domains is the kind of problem to which they are ideally suited, like the ones studied in the present work.

3.4.2 Finite difference method

The finite differences (FD) is one of the easiest methods for numerical solutions of partial differential equations (PDE). The starting point is to discretize the geometric domain and define a numerical grid. For FD discretization methods, the grid is usually locally structured, *i.e.*, each grid node is considered as the origin of a local coordinate system, whose axes coincide with grid lines. This also implies that two grid lines belonging to the same direction, say x, do not intersect, as opposed to any pair of grid lines from different directions intersect only once. Figure 3.2 shows examples of Cartesian grids used in FD

methods.

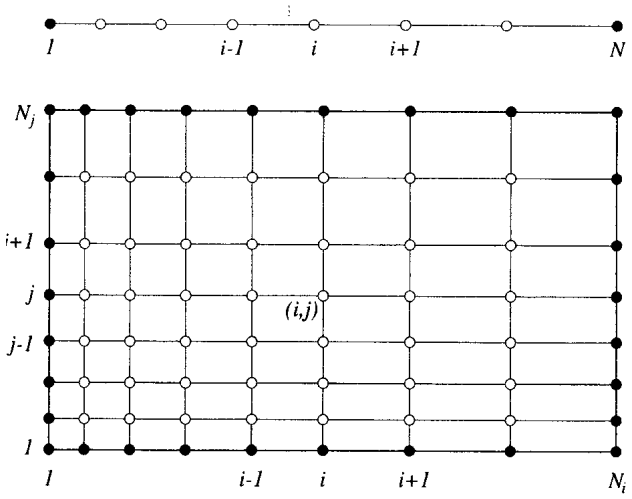

Figure 3.2: Examples of a 1D (above) and 2D (below) Cartesian grid for FD method (full symbols denote boundary nodes and open symbols denote computational nodes). [81]

As can be seen in fig. 3.2, each node is uniquely identified by a set of indices, (i,j,k) in 3D, while the neighbor nodes are defined by increasing or reducing one of the indices by multiples of unity.

The idea behind finite difference approximations comes directly from the definition of a derivative:

$$\left(\frac{\partial \phi}{\partial x}\right)_{x_i} = \lim_{\Delta x \to 0} \frac{\phi(x_i + \Delta x) - \phi(x_i)}{\Delta x}. \tag{3.11}$$

To a better understanding, a geometrical interpretation is shown in fig. 3.3. The first derivative $\partial\phi/\partial x$ at a point is the slope of the tangent to the curve $\phi(x)$ at that same point. This slope can be approximated by the slope of a line passing through two nearby points. In the figure, the dotted line, the dashed line and the line labeled 'Central' represents a *forward difference*, a *backward difference* and a *central difference*, respectively. In the first approximation, the derivative is equal to the slope of a line passing through x_i and $x_i + \Delta x$. On the second, the line passes also in x_i but now the second point is $x_i - \Delta x$. The last approximation uses the slope of a line passing through lying on opposite sides of the point x_i, which are $x_i - \Delta x$ and $x_i + \Delta x$.

Inspecting fig. 3.3, it is perceptible that some approximations methods are better than others. To the case, the central difference method has a slope very close to the slope of the exact line. Moreover, it is also possible to deduce that the quality of the approximation improves when the additional points are close to x_i, *i.e.*, as the grid is refined, Δx gets smaller and results become more accurate.

As mentioned before, there are several approaches to get an approximation of the first derivative of a generic variable ϕ.

Any continuous differentiable function $\phi(x)$ can, in the vicinity of x_i, be expressed as a Taylor series

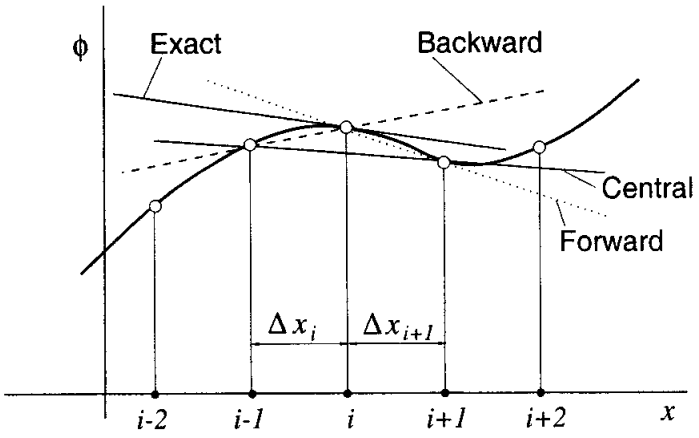

Figure 3.3: Definition of a derivative and its approximations. [81]

[81]:

$$\phi(x) = \phi(x_i) + (x - x_i)\left(\frac{\partial \phi}{\partial x}\right)_i + \frac{(x - x_i)^2}{2!}\left(\frac{\partial^2 \phi}{\partial x^2}\right)_i + \frac{(x - x_i)^3}{3!}\left(\frac{\partial^3 \phi}{\partial x^3}\right)_i + \cdots + \frac{(x - x_i)^n}{n!}\left(\frac{\partial^n \phi}{\partial x^n}\right)_i + H, \tag{3.12}$$

where H means high-order terms. By replacing x for x_{i+1} or x_{i-1} in this equation, one gets expressions for the variable values at those points of the variable and its derivatives at x_i.

Thus, by using these expansions, one can obtain approximate expressions for the first and higher derivatives at point x_i in terms of the function values at surrounding points. For instance, taking ϕ at x_{i+1} and Eq. (3.12), the first derivative takes the form:

$$\left(\frac{\partial \phi}{\partial x}\right)_i = \frac{\phi_{i+1} - \phi_i}{x_{i+1} - x_i} - \frac{x_{i+1} - x_i}{2}\left(\frac{\partial^2 \phi}{\partial x^2}\right)_i - \frac{(x_{i+1} - x_i)^2}{6}\left(\frac{\partial^3 \phi}{\partial x^3}\right)_i + H. \tag{3.13}$$

On the other side, by taking the series expression (3.12) evaluated at x_{i-1}, another expression for the derivative may be obtained:

$$\left(\frac{\partial \phi}{\partial x}\right)_i = \frac{\phi_i - \phi_{i-1}}{x_i - x_{i-1}} - \frac{x_i - x_{i-1}}{2}\left(\frac{\partial^2 \phi}{\partial x^2}\right)_i - \frac{(x_i - x_{i-1})^2}{6}\left(\frac{\partial^3 \phi}{\partial x^3}\right)_i + H. \tag{3.14}$$

Still another expression may be derived simply by using Eq. (3.12) at both x_{i-1} and x_{i+1}:

$$\left(\frac{\partial \phi}{\partial x}\right)_i = \frac{\phi_{i+1} - \phi_{i-1}}{x_{i+1} - x_{i-1}} - \frac{(x_{i+1} - x_i)^2 - (x_i - x_{i-1})^2}{2(x_{i+1} - x_{i-1})}\left(\frac{\partial^2 \phi}{\partial x^2}\right)_i - \frac{(x_{i+1} - x_i)^3 + (x_i - x_{i-1})^3}{6(x_{i+1} - x_{i-1})}\left(\frac{\partial^3 \phi}{\partial x^3}\right)_i + H. \tag{3.15}$$

It must be kept in mind that all the three expressions are exact if all terms on the right hand side are retained. Also, because the high-order derivatives are unknown, these expressions are not of great value as they are. Nevertheless, if the distance between the grid points ($x_{i+1} - x_i$ and $x_i - x_{i-1}$) is small, the higher-order terms will be small except in the unusual situation in which those higher derivatives are

locally very large. If one ignores the latter possibility and truncate each of the series after the first terms on the right hand sides, the approximations to the first derivative results in:

$$\left(\frac{\partial\phi}{\partial x}\right)_i \approx \frac{\phi_{i+1}-\phi_i}{x_{i+1}-x_i}; \tag{3.16}$$

$$\left(\frac{\partial\phi}{\partial x}\right)_i \approx \frac{\phi_i-\phi_{i-1}}{x_i-x_{i-1}}; \tag{3.17}$$

$$\left(\frac{\partial\phi}{\partial x}\right)_i \approx \frac{\phi_{i+1}-\phi_{i-1}}{x_{i+1}-x_{i-1}}. \tag{3.18}$$

These are the forward (FDS), backward (BDS), and central difference (CDS) schemes mentioned earlier, respectively. The terms deleted from the right hand sides are called the *truncation errors* and they measure the accuracy of the approximation, while at the same time determine the rate at which the error decreases as the grid gets more refined.

The truncation error is the sum of products between a power of the grid resolution and a high order derivative at the point $x = x_i$:

$$\epsilon_\tau = (\Delta x)^m \alpha_{m+1} + (\Delta x)^{m+1}\alpha_{m+2} + \cdots + (\Delta x)^n \alpha_{n+1}, \tag{3.19}$$

where Δx is the space between two grid points and the α's are higher-order derivatives multiplied by constant factors. From Eq. (3.19), it is obvious that the terms containing higher powers of Δx are smaller for small spacing so their first truncated term is usually the dominant one (the one with the smallest exponent). As Δx is reduced, the aforementioned approximations converge to the exact derivatives with an error proportional to $(\Delta x)^m$. The order of an approximation indicates only how fast the error is reduced when the grid is refined and does not indicate anything about its magnitude.

3.4.3 Navier-Stokes equations

Equations (3.1) and (3.2) can be rewritten in indicial notation

$$\frac{\partial u_i}{\partial x_i} = 0, \tag{3.20}$$

$$\frac{\partial u_i}{\partial t} + \frac{\partial (u_i u_j)}{\partial x_j} = -\frac{1}{\rho}\frac{\partial p}{\partial x_i} + \nu^{[s]}\frac{\partial^2 u_i}{\partial x_j \partial x_j} + \frac{\partial \tau_{ij,p}}{\partial x_j}, \tag{3.21}$$

where $\tau_{ij,p} = \frac{\nu^{[p]}}{\lambda_p}[f(C_{kk})C_{ij} - \delta_{ij}]$. Then, introducing the Fourier transform (FT), the mass conservation equation simple yields

$$FT\left\{\frac{\partial u_i}{\partial x_i} = 0\right\} \Rightarrow \mathrm{i}k_i\hat{u}_i = 0 \tag{3.22}$$

By doing the same thing to equation (3.21),

$$FT\left\{\frac{\partial u_i}{\partial t} + \frac{\partial (u_i u_j)}{\partial x_j} = -\frac{1}{\rho}\frac{\partial p}{\partial x_i} + \nu^{[s]}\frac{\partial^2 u_i}{\partial x_j \partial x_j} + \frac{\partial \tau_{ij,p}}{\partial x_j}\right\}, \tag{3.23}$$

one obtains:

$$FT\left\{\frac{\partial u_i}{\partial t}\right\} = \frac{\partial \hat{u}_i}{\partial t}; \tag{3.24}$$

$$FT\left\{-\frac{1}{\rho}\frac{\partial p}{\partial x_i}\right\} = -\mathrm{i}k_i FT\left\{\frac{p}{\rho}\right\} = -\mathrm{i}k_i\hat{p}; \tag{3.25}$$

$$FT\left\{\nu^{[s]}\frac{\partial^2 u_i}{\partial x_j \partial x_j}\right\} = -\nu^{[s]}k^2\hat{u}_i; \tag{3.26}$$

$$FT\left\{\frac{\partial}{\partial x_j}\left(u_i u_j - \tau_{ij,p}\right)\right\} = \hat{G}_i. \tag{3.27}$$

The modified Navier-Stokes equation for linear momentum in the Fourier space results in

$$\frac{\partial \hat{u}_i}{\partial t} + \nu^{[s]}k^2\hat{u}_i = -\mathrm{i}k_i\hat{p} - \hat{G}_i. \tag{3.28}$$

To remove the pressure from Eq. (3.28), one multiplies for $\mathrm{i}k_i$ both sides of the equation and introduces the continuity equation (Eq. (3.22)), reducing Eq. (3.28) to a Poisson equation:

$$k^2\hat{p} = \mathrm{i}k_i\hat{G}_i \tag{3.29}$$

The pressure yields

$$\hat{p} = \frac{\mathrm{i}k_i\hat{G}_i}{k^2}, \tag{3.30}$$

meaning that

$$-\mathrm{i}k_i\hat{p} = \frac{k_i k_j\hat{G}_i}{k^2}. \tag{3.31}$$

Thus, after substitution of Eq. (3.31), Eq. (3.28) becomes

$$\frac{\partial \hat{u}_i}{\partial t} + \nu^{[s]}k^2\hat{u}_i = -P_{ij}\hat{G}_i, \tag{3.32}$$

where $P_{ij} = \left(\delta_{ij} + \frac{k_i k_j}{k^2}\right)$ is the projection operator. However, there is still one unknown to be found, $\hat{G}_i$.

In order to supress this problem, in the numerical code, the starting point was the rotation form of the momentum equation:

$$\frac{\partial \mathbf{u}}{\partial t} = \mathbf{u}\times\boldsymbol{\omega} - \nabla\left(\frac{p}{\rho} + \frac{u^2}{2}\right) + \nu^{[s]}\nabla^2\mathbf{u} + \nabla\tau_p; \tag{3.33}$$

where $\boldsymbol{\omega} = \nabla\times\mathbf{u}$ is the vorticity. Applying the Fourier transform to Eq. (3.33), in the Fourier space results

$$\frac{\partial \hat{\mathbf{u}}}{\partial t} + \nu^{[s]}k^2\hat{\mathbf{u}} = \hat{\mathbf{T}}_{NL} - \mathrm{i}\mathbf{k}\hat{p}, \tag{3.34}$$

where $\hat{\mathbf{T}}_{NL} = FT\left\{\mathbf{u}\times\boldsymbol{\omega} + \nabla\tau_p\right\}$ is the nonlinear term. As before, by introducing the projection operator $\Pi = P_{ij}$, the Navier-Stokes equation is defined as:

$$\frac{\partial \hat{\mathbf{u}}}{\partial t} + \nu^{[s]}k^2\hat{\mathbf{u}} = \boldsymbol{\Pi}\cdot\hat{\mathbf{T}}_{NL}. \tag{3.35}$$

However, the convolution involved in the right hand side is very expensive to solve. The solution for this problem lies on the fast Fourier transform (FFT) procedure, which allows a much faster result than a direct evaluation of the generalized convolution product in the Fourier space. The pseudo-spectral numerical code performs the vectorial product on the physical space and then goes to the Fourier space, resulting the following final equation to be solved:

$$\frac{\partial \hat{\mathbf{u}}}{\partial t} + \nu^{[s]} k^2 \hat{\mathbf{u}} = \mathbf{\Pi} \cdot \left[FFT \left[FFT^{-1}(\mathbf{u}) \times FFT^{-1}(\boldsymbol{\omega}) \right] + \mathrm{i}\mathbf{k}\tau_p \right]. \tag{3.36}$$

Finally, by solving Eq. (3.36), one can obtain the velocity field and consequently retrieve the pressure field.

3.4.4 Conformation tensor equation

The spectral and high-order compact schemes are not suitable to solve Eq. (3.3), since they lose spectral convergence in the vicinity of the descontinuities [7]. Therefore, in spatial domain, a second-order central difference scheme is adopted for the discretization, except for the convective term.

$$\frac{\partial \mathbf{C}}{\partial t} + \mathbf{u} \cdot \nabla \mathbf{C} = \mathbf{C} \cdot \nabla \mathbf{u} + \nabla \mathbf{u}^T \cdot \mathbf{C} - \frac{1}{\lambda_p} \left[f(R)\mathbf{C} - \mathbf{I} \right] \tag{3.3}$$

Stretching Terms

Discretization of the Eq. (3.3) requires the approximation of the first derivative on the stretching terms $\mathbf{C} \cdot \nabla \mathbf{u} + \nabla \mathbf{u}^T \cdot \mathbf{C}$, here written in indicial notation:

$$\mathbf{C} \cdot \nabla \mathbf{u} + \nabla \mathbf{u}^T \cdot \mathbf{C} \Rightarrow C_{ik} \frac{\partial u_j}{\partial x_k} + C_{kj} \frac{\partial u_i}{\partial x_k}. \tag{3.37}$$

Using the central difference scheme Eq. (3.18), the first derivative results in

$$\frac{\partial u_j}{\partial x_k} = \frac{(u_j)_{m+1} - (u_j)_{m-1}}{(x_k)_{m+1} - (x_k)_{m-1}} = \frac{(u_j)_{m+1} - (u_j)_{m-1}}{2\Delta x_k}, \tag{3.38}$$

$$\frac{\partial u_i}{\partial x_k} = \frac{(u_i)_{m+1} - (u_i)_{m-1}}{(x_k)_{m+1} - (x_k)_{m-1}} = \frac{(u_j)_{m+1} - (u_j)_{m-1}}{2\Delta x_k}. \tag{3.39}$$

This method is second-order accurate everywhere in space. Replacing the derivatives, the stretching terms take the form:

$$C_{ik} \frac{\partial u_j}{\partial x_k} + C_{kj} \frac{\partial u_i}{\partial x_k} = C_{ik} \frac{(u_j)_{m+1} - (u_j)_{m-1}}{2\Delta x_k} + C_{kj} \frac{(u_j)_{m+1} - (u_j)_{m-1}}{2\Delta x_k}. \tag{3.40}$$

Convective term

For the convective term in Eq. (3.3), an approach based on the Kurganov-Tadmor (KT) scheme is used. This method guarantees that a positive scalar will remain so at all points and it was generalized to do same thing to a tensor, *i.e.*, a SPD tensor remains SPD [7]. Spatial derivatives are second-order accurate everywhere, except where it leads to a loss of the SPD property. Where that occurs, the

method automatically reverts to first-order for that grid point, ensuring the SPD property is mantained. The equations for the six independent components of $\mathbf{C}$ are coupled to the velocity field and must be solved simultaneously.

The convective term is discretized as follows [7]:

$$\mathbf{u}\cdot\nabla\mathbf{C} = \frac{\mathbf{H}^x_{i+1/2,j,k} - \mathbf{H}^x_{i-1/2,j,k}}{\Delta x} + \frac{\mathbf{H}^y_{i,j+1/2,k} - \mathbf{H}^y_{i,j-1/2,k}}{\Delta y} + \frac{\mathbf{H}^z_{i,j,k+1/2} - \mathbf{H}^z_{i,j,k-1/2}}{\Delta z}, \tag{3.41}$$

where the convective flux in each direction is given by

$$\begin{cases} \mathbf{H}^x_{i+1/2,j,k} = \frac{1}{2}u_{i+1/2,j,k}(\mathbf{C}^+_{i+1/2,j,k} + \mathbf{C}^-_{i+1/2,j,k}) - \frac{1}{2}|u_{i+1/2,j,k}|(\mathbf{C}^+_{i+1/2,j,k} - \mathbf{C}^-_{i+1/2,j,k}), \\ \mathbf{H}^y_{i,j+1/2,k} = \frac{1}{2}v_{i,j+1/2,k}(\mathbf{C}^+_{i,j+1/2,k} + \mathbf{C}^-_{i,j+1/2,k}) - \frac{1}{2}|v_{i,j+1/2,k}|(\mathbf{C}^+_{i,j+1/2,k} - \mathbf{C}^-_{i,j+1/2,k}), \\ \mathbf{H}^z_{i,j,k+1/2} = \frac{1}{2}w_{i,j,k+1/2}(\mathbf{C}^+_{i,j,k+1/2} + \mathbf{C}^-_{i,j,k+1/2}) - \frac{1}{2}|w_{i,j,k+1/2}|(\mathbf{C}^+_{i,j,k+1/2} - \mathbf{C}^-_{i,j,k+1/2}). \end{cases} \tag{3.42}$$

The superscripts '+' and '–' on the right hand side in Eq. (3.42) refers to values of the conformation tensor at the interface obtained in the limit approaching the point of interest from the right (+) or left (–). Note that nothing is forcing the two values at a boundary to be identical, allowing the possibility of jumps in the solution. The conformation tensor $\mathbf{C}$ at the interface is constructed from the following second-order linear approximations:

$$\begin{cases} \mathbf{C}^\pm_{i+1/2,j,k} = \mathbf{C}_{i+1/2\pm1/2,j,k} \mp \left(\frac{\Delta x}{2}\right)\left(\frac{\partial\mathbf{C}}{\partial x}\right)_{i+1/2\pm1/2,j,k}; \\ \mathbf{C}^\pm_{i,j+1/2,k} = \mathbf{C}_{i,j+1/2\pm1/2,k} \mp \left(\frac{\Delta y}{2}\right)\left(\frac{\partial\mathbf{C}}{\partial y}\right)_{i,j+1/2\pm1/2,k}; \\ \mathbf{C}^\pm_{i,j,k+1/2} = \mathbf{C}_{i,j,k+1/2\pm1/2} \mp \left(\frac{\Delta z}{2}\right)\left(\frac{\partial\mathbf{C}}{\partial z}\right)_{i,j,k+1/2\pm1/2}. \end{cases} \tag{3.43}$$

This central difference approximation to the convective term allows to capture the potentially sharp variations in the conformation field and, by writing the convective flux with a difference formula the conservation of the mean conformation tensor is automatically satisfied [7]. To complete the expression, approximations for the spatial derivatives of the conformation tensor are required. These quantities must be defined in a way that maintains $\mathbf{C}^\pm$ each as SPD. Therefore, potential candidates to approximate the gradients are

$$\left(\frac{\partial\mathbf{C}}{\partial x}\right)_{i,j,k} = \begin{cases} (\mathbf{C}_{i+1,j,k} - \mathbf{C}_{i,j,k})/\Delta x, \\ (\mathbf{C}_{i,j,k} - \mathbf{C}_{i-1,j,k})/\Delta x, \\ (\mathbf{C}_{i+1,j,k} - \mathbf{C}_{i-1,j,k})/(2\Delta x). \end{cases} \tag{3.44}$$

To select the correct derivative approximation, one must check if it can yield symmetric positive definite (SPD) results for $\mathbf{C}^+_{i-1/2}$ and $\mathbf{C}^-_{i+1/2}$. When two or more candidates satisfy the criterion, it is selected the one which maximizes the minimum eigenvalue for these two tensors. When none of them meet this criterion, the derivative is set to zero, reducing to first-order (locally) accurate. This slope limiting procedure will ensure that all $\mathbf{C}^\pm$ are SPD and proof of that is given by Vaithianathan *et al.* in [7].

In order to calculate the convective flux, Eq. (3.42), area-averaged velocities at the edge of the

volume surrounding each grid point are required. However, by using a pseudo-spectral code in the velocity update, a complication is the area-averaged velocities at cell edges are not known. One could try to average the nearest grid points, but this approach would not satisfy the condition

$$\frac{u_{i+1/2,j,k} - u_{i-1/2,j,k}}{\Delta x} + \frac{v_{i,j+1/2,k} - v_{i,j-1/2,k}}{\Delta y} + \frac{w_{i,j,k+1/2} - w_{i,j,k-1/2}}{\Delta z} = 0, \tag{3.45}$$

which follows from the continuity equation (Eq. (3.1)). As the spectral decomposition of the velocity is known, it is possible to obtain exact expressions for the cell edge velocities:

$$\begin{cases} u_{i\pm1/2,j,k} = FFT^{-1}\left\{\hat{u}e^{\pm ik_x\Delta x/2}\frac{\sin(k_y\Delta y/2)}{k_y\Delta y/2}\frac{\sin(k_z\Delta z/2)}{k_z\Delta z/2}\right\}, \\ v_{i,j\pm1/2,k} = FFT^{-1}\left\{\hat{v}e^{\pm ik_y\Delta y/2}\frac{\sin(k_z\Delta z/2)}{k_z\Delta z/2}\frac{\sin(k_x\Delta x/2)}{k_x\Delta x/2}\right\}, \\ w_{i,j,k\pm1/2} = FFT^{-1}\left\{\hat{w}e^{\pm ik_z\Delta z/2}\frac{\sin(k_x\Delta x/2)}{k_x\Delta x/2}\frac{\sin(k_y\Delta y/2)}{k_y\Delta y/2}\right\}, \end{cases} \tag{3.46}$$

where FFT^{-1} is the inverse fast Fourier transform, $\hat{u}(k_x, k_y, k_z)$, $\hat{v}(k_x, k_y, k_z)$ and $\hat{w}(k_x, k_y, k_z)$ are the Fourier coefficients at each grid point. Substitution of the above into Eq. (3.45) shows the discrete continuity relationship is satisfied if the continuity equation in Fourier space is also satisfied [7]:

$$k_x\hat{u}(k_x, k_y, k_z) + k_y\hat{v}(k_x, k_y, k_z) + k_z\hat{w}(k_x, k_y, k_z) = 0 \tag{3.47}$$

3.5 Temporal discretization

The simulation results from solving equations (3.1), (3.2) and (3.3) in both space and time. For this purpose, the numerical code uses a fully explicit Runge-Kutta scheme. The three equations can be rewritten as

$$\nabla \cdot \mathbf{u} = 0, \tag{3.48}$$

$$\frac{\partial \mathbf{u}}{\partial t} = N(\mathbf{u}) + L(\mathbf{u}) + S(\mathbf{C}), \tag{3.49}$$

$$\frac{\partial \mathbf{C}}{\partial t} = M(\mathbf{C}), \tag{3.50}$$

where $N(\mathbf{u}) = \mathbf{u} \times \boldsymbol{\omega} - \boldsymbol{\nabla}\pi$ is the convective term, $L(\mathbf{u}) = \nu^{[s]}\nabla^2\mathbf{u}$ is the viscous term, $\boldsymbol{\omega}(\mathbf{x}, t) = \nabla \times \mathbf{u}$ is the vorticity vector, $\pi(\mathbf{x}, t) = \frac{p}{\rho} + \frac{u^2}{2}$ is the modified pressure, $S(\mathbf{C})$ is the additional elastic stress tensor

$$S(\mathbf{C}) = \frac{\nu^{[p]}}{\tau_p}\nabla(f(R)\mathbf{C} - \mathbf{I}),$$

and $M(\mathbf{C})$ stands for

$$M(\mathbf{C}) = \mathbf{C} \cdot \nabla\mathbf{u} + \nabla\mathbf{u}^T \cdot \mathbf{C} - \mathbf{u} \cdot \nabla\mathbf{C} - \frac{1}{\lambda_p}\left[f(R)\mathbf{C} - \mathbf{I}\right].$$

The 3 step, 3rd order Runge-Kutta scheme calculates each sub-step value p from the last two time

sub-steps, $p-1$ and $p-2$, using

$$\nabla \cdot \mathbf{u}^p = 0, \tag{3.51}$$

$$\frac{\mathbf{u}^p - \mathbf{u}^{p-1}}{\Delta t} = \alpha_p[N(\mathbf{u}^{p-1}) + L(\mathbf{u}^{p-1}) + S(\mathbf{C}^{p-1})] + \beta_p[N(\mathbf{u}^{p-2}) + L(\mathbf{u}^{p-2}) + S(\mathbf{C}^{p-2})], \tag{3.52}$$

$$\frac{\mathbf{C}^p - \mathbf{C}^{p-1}}{\Delta t} = \alpha_p M(\mathbf{C}^{p-1}) + \beta_p M(\mathbf{C}^{p-2}). \tag{3.53}$$

The coefficients in Eq. (3.52) and Eq. (3.53), for a 3rd order accuracy [43] with 3 time sub-steps $p = 1, 2, 3$, are

$$\begin{aligned} \alpha_1 &= 8/15 \qquad & \beta_1 &= 0, \\ \alpha_2 &= 5/12 \qquad & \beta_2 &= -17/60, \\ \alpha_3 &= 3/4 \qquad & \beta_3 &= -5/12. \end{aligned} \tag{3.54}$$

Then, in order to solve the equations (3.51), (3.52) and (3.53), the Fourier transforms must be applied, resulting in

$$\frac{\hat{\mathbf{u}}^p - \hat{\mathbf{u}}^{p-1}}{\Delta t} = \alpha_p \left[\hat{\mathbf{N}}^{p-1} - \nu k^2 \hat{\mathbf{u}}^{p-1} + \hat{\mathbf{S}}^{p-1}\right] + \beta_p \left[\hat{\mathbf{N}}^{p-2} - \nu k^2 \hat{\mathbf{u}}^{p-2} + \hat{\mathbf{S}}^{p-2}\right], \tag{3.55}$$

$$\frac{\hat{\mathbf{C}}^p - \hat{\mathbf{C}}^{p-1}}{\Delta t} = \alpha_p \hat{\mathbf{M}}^{p-1} + \beta_p \hat{\mathbf{M}}^{p-2}, \tag{3.56}$$

where

$$k^2 = k_x^2 + k_y^2 + k_z^2. \tag{3.57}$$

The velocity field obtained from Eq. (3.55) then satisfies the incompressible condition:

$$ik_x\hat{u}^p + ik_y\hat{v}^p + ik_z\hat{w}^p = 0. \tag{3.58}$$

3.6 Stability conditions

Common to all the numerical codes are the problems related to numerical instabilities during the simulations. For the case studied herein, the main sources of instabilities and the methods used to overcome them are described in the following paragraphs.

3.6.1 Conformation tensor

The conformation tensor $\mathbf{C}$ is a variance-covariance matrix, whose elements in the diagonal are the variance of the vector $\langle r_i r_i \rangle$ and the elements in the i, j position are the covariance between the i^{th} and j^{th} elements. Therefore, since the variance of any real random variable is non-negative, the elements in the diagonal are also non-negative. Moreover, since $\langle r_i r_j \rangle = \langle r_j r_i \rangle$ the tensor is also symmetric. The constraint $\langle r_i r_i \rangle > 0$ leads to positive values for all elements in the diagonal, making the tensor symmetric and positive definite. This implies that the eigenvalues of C_{ij} should always remain greater

than zero.

$$\lambda_1, \lambda_2, \lambda_3 > 0 \tag{3.59}$$

So, it must ensured that during a simulation the conformation tensor remains SPD everywhere at any time. Early attemps at numerical simulation of viscoelastic turbulence were plagued by Hadamard instabilities that resulted from the numerical loss of the SPD property. To overcome these instabilities, most investigators introduces a stress diffusion term into the equation for the conformation tensor, a very common pratice nowadays [7].

Recently, Vaithianathan and Collins [8] exploited the SPD property of C_{ij} to derive independent equations for the eigenvectors and eigenvalues of the conformation tensor. In this formulation, besides remain greater than zero, the eigenvalues of C_{ij} should comply with the finite extensibility of the polymer:

$$\lambda_1 + \lambda_2 + \lambda_3 \leq L^2, \tag{3.60}$$

Despite the implicit formulation made by these two researchers ensured Eq. (3.60) was satisfied, the finite-difference method [8] they used did not prevent the negative eigenvalues. Thus, this decomposition guaranteed stability, but not guaranteed conservation.

The problem can be traced to the hyperbolic nature of the equation for C_{ij} in the Oldroyd-B, FENE-P and Giesekus models, which admits shocks (discontinuities) in the polymer stress tensor [7]. These jumps must satisfy the overall conservation balance to guarantee correct elastic wave propagation. However, these near discontinuities cannot be resolved in the absence of a stress diffusion term in Eq. (3.3). Spectral methods applied directly to Eq. (3.3) will produce ringing (Gibbs phenomenon) in the vicinity of the jumps in the conformation tensor, causing either overshoots or undershoots that may generate negative eigenvalues. Artificial diffusion added to Eq. (3.3) smooths out the sharp gradients so that spectral or high-order schemes can converge smoothly to a solution (fig. 3.4). Altough, because capturing the strength of the shocks, when present, is essential to correctly predict the effect of the polymer on the turbulence, this approach carries inaccuracies in these kind of situations. Also, spectral and high-order compact schemes are not suited to solving hyperbolic equations, as they lose spectral convergence in the proximity of the discontinuities.

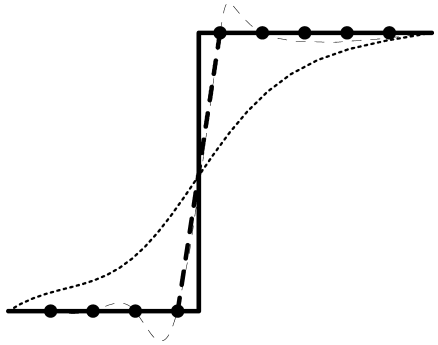

Figure 3.4: One-dimensional schematic of a shock (thick, solid line). Black dots represent the grid points. Thick dashed line is an ideal representation of the shock on the grid. Thin dashed line is spectral representation, without an artificial stress diffusivity, with overshoots and undershoots (Gibbs phenomenon). The dotted line indicates the effect of adding the stress diffusivity to the spectral representation. [7]

Due to these difficulties, Vaithianathan *et al.* [7] developed an algorithm based on the method of Kurganov and Tadmor [90] (KT). As mentioned early, this second-order scheme guarantees that a positive scalar will remain so at all points and it was generalized to guarantee that a SPD tensor also remains SPD. Besides, the limitation with numerical dissipation suffered by some central difference schemes, that cause severe smearing in the limit $\Delta t \to 0$, is also overcomed by the central difference scheme of KT. Finally, this algorithm dissipates less elastic energy than methods based on artificial diffusion, resulting in stronger polymer-flow interactions.

3.6.2 Time step

The time step used in the numerical resolution of a system of partial differential equations is bounded by stability restrictions [81]. In problems where convection is the dominant term (such as those analysed here), the key parameter governing the numerical method stability is the Courant number, expressed by Eq. (3.61):

$$C = \frac{|\mathbf{u}|\Delta t}{|\Delta x|}. \tag{3.61}$$

In the multidimensional case, the limiting Courant number for a particular problem is found by making an assessment of Eq. (3.61) for each of the flow directions.

For the viscoelastic plane jet case described, a more restrict Courant number was found [7], comparing to a Newtonian fluid. The limit value of $C < 1/6 \approx 0.1667$ was found, as opposed to the limit value of a Newtonian fluid $C < 0.6$. At each iteration, the maximum velocity of each component is found and if the former condition is violated, Δt is readjusted using Eq. (3.62):

$$\Delta t = C \times \min\left\{ \frac{\pi\Delta x}{|u|_{max}}, \frac{\pi\Delta y}{|v|_{max}}, \frac{\pi\Delta z}{|w|_{max}} \right\}. \tag{3.62}$$

In Eq. (3.62), $|u|_{max}$, $|v|_{max}$ and $|w|_{max}$ are the maximum velocity found in the flowfield, in each direction. The factor π is due to the spectral nature of the spatial discretization [82].

3.7 Boundary conditions

The proper implementation of boundary conditions is very important for the success of every numerical code. The following paragraphs describe the boundary conditions assigned during the jet simulations.

3.7.1 Inlet

The inlet condition is prescribed only at the inital time step, having a general form of

$$\mathbf{u}(\mathbf{x}_0, t_0) = \mathbf{U}_{med}(\mathbf{x}_0) + \mathbf{U}_{noise}, \tag{3.63}$$

where $\mathbf{x}_0 = (x = 0, y, z)$ is the coordinate at the inlet plane, $\mathbf{U}_{med}$ is the mean inlet profile and $\mathbf{U}_{noise}$ a superimposed random numerical noise.

For the planar jet, in the x direction, the mean velocity profile has the shape of an hyperbolic tangent profile [16] expressed by Eq. (3.64), while for the normal and spanwise directions, the mean velocities are set to be zero at the inlet.

$$U_{med} = \frac{U_2 + U_1}{2} + \frac{U_2 - U_1}{2} \tanh\left(\frac{H}{4\theta_0}\left(1 - \frac{2|y|}{H}\right)\right) \tag{3.64}$$

In Eq. (3.64), θ_0 is the momentum thickness of the initial shear layer and H is the inlet nozzle witdh. U_1 is the minimum initial jet velocity and U_2 is the maximum initial jet velocity. In the present work, $U_1 = 0$ and $U_2 = 1$, with an initial imposed value of $H/\theta_0 = 35$.

The numerical noise, $\mathbf{U}_{noise}$ superimposed to the mean profile in Eq. (3.63), results from a convolution function, $\mathbf{U}_{base}$, which creates velocity fluctuations in the inital shear layer regions of the plane jet. This noise profile has the form of

$$\mathbf{U}_{noise} = amp\mathbf{U}_{base}\mathbf{u}', \tag{3.65}$$

where $\mathbf{u}' = (u', v', w')$ comes from a random number generator designed in such way that its energy spectrum is given by

$$E(k) \propto k^s \exp\left[-\frac{s}{2}(k/k_0)^2\right]. \tag{3.66}$$

The exponent s is the slope of the noise spectrum in the large scales region and k_0 is the peak wavenumber. Both parameters are assigned to provide realistic conditions. The slope has a value of $s < 4$, as in decaying turbulence, and k_0 is chosen to give an energy input that is dominant at the small scales region (high k_0). This allows the simulations to evolve in a more 'natural' way, through the selection of its natural and most unstable modes.

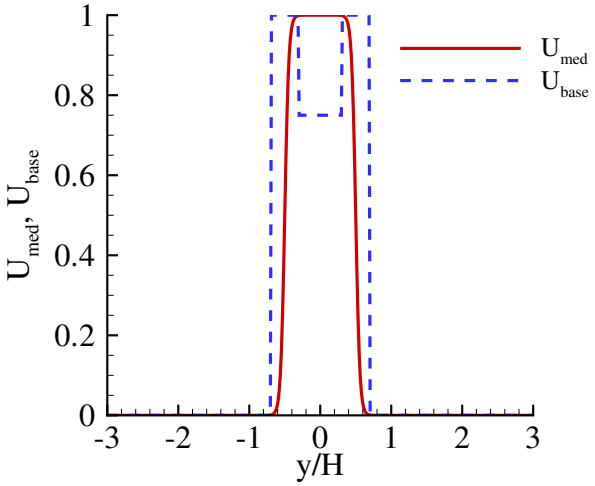

Figure 3.5: Inlet velocity profile and respective convolution function

The fluctuations on the numerical noise have relatively high amplitude (8%). This, associated with the high non-dimensional ratio between the inlet slot width and the initial momentum thickness H/θ_0,

allows to accelerate the transition process and consequently reach fully turbulent state sooner.

This velocity profile is the same used in several plane jet spatial direct numerical simulations, like the ones performed by Stanley *et al.* [16] and da Silva & Metáis [83]. It was also present on the plane jet temporal simulations realized by Akhavan *et al.* [79] and da Silva & Pereira [80], [84]. As stated, this velocity profile is commonly used, due to the fact that is recognized to be an excellent approximation to the inlet velocity profiles found in jet experimental measurements.

3.7.2 Lateral boundaries

The use of pseudo-spectral methods implies the use of periodic boundary conditions, along all three spatial directions. This means that all the spatial dependent entities, namely the velocity field and the conformation tensor, must obey the following relations:

$$\begin{aligned} \mathbf{u}(x,y,z,t) &= \mathbf{u}(x+L_x,y,z,t); \\ \mathbf{u}(x,y,z,t) &= \mathbf{u}(x,y+L_y,z,t); \\ \mathbf{u}(x,y,z,t) &= \mathbf{u}(x,y,z+L_z,t); \end{aligned} \tag{3.67}$$

$$\begin{aligned} \mathbf{C}(x,y,z,t) &= \mathbf{C}(x+L_x,y,z,t); \\ \mathbf{C}(x,y,z,t) &= \mathbf{C}(x,y+L_y,z,t); \\ \mathbf{C}(x,y,z,t) &= \mathbf{C}(x,y,z+L_z,t). \end{aligned} \tag{3.68}$$

As can be seen in Eqs. (3.67) and (3.68), there is no enforcement of zero to the instantaneous velocities normal to the boundary. Altough the mean normal velocities are null, which makes clear that such boundary conditions, despite allowing the application of pseudo-spectral schemes, do not conceive the natural growth of the jet. To supress this problem, the lateral boundaries must be placed sufficiently far away from the the inlet so the jet dynamics can develop properly. It must also be noted that the aforementioned problem only affect the normal and spanwise directions, the streamwise direction is naturaly periodic.

Chapter 4

Verification and validation

The numerical code for the viscoelastic fluids, like any other, must be validated. Since the code was already validated for the velocity fields [12], the process to obtain the conformation tensor is the one thing left for analysis. In the present work, the main concern is to ensure that the polymer model is being properly solved and therefore its contribution to the flow is physically correct.

As mentioned before, the most common source of errors is related to numerical instabilities on the conformation tensor that leads to irrealistic values. For this reason, the performance of the method implemented is evaluated through direct numerical simulations on decaying homogeneous isotropic turbulence and the results are then compared to the ones obtained by Zhang *et al.* [4].

4.1 Decaying homogeneous viscoelastic turbulence

An homogeneous and isotropic turbulent flow is characterized as being statistically invariant under rotations about arbitrary axes and, in consequence, statistically invariant under translations. From this description it is possible to infer that, when in presence of such flow, the average velocity is zero. Although this concept corresponds to an idealized type of flow, it can be approximated by a grid-generated turbulence in a wind tunnel.

Homogeneous isotropic turbulence is normally simulated using unbounded cubic domain. This geometry has periodic boundary conditions in all three directions of the domain, which also enables the use of the pseudo-spectral methods. Because they are the simplest class of flows to study under numerical simulations and because they allow the use of efficient and fast numerical schemes, homogeneous isotropic turbulent flows are a popular case study in the numerical simulations frame of reference. Besides, it allows higher Reynolds number simulations and it is the only type of flow where the turbulent structures interact free from any external surfaces, as opposed with the remaining kinds of flows where the geometry of the problem also interacts with the turbulent field, affecting the shape of those strucures.

In general, the simulation of isotropic turbulence has two approaches: decaying and forced turbulence. In the first, an homogeneous isotropic velocity field is imposed as initial condition and the flow evolves dissipating the turbulent kinetic energy. In forced turbulence, the flow is made statistically sta-

tionary by the forcing, *i.e.*, turbulence is mantained by artificially adding energy to the low-wavenumber components of the velocity field. Compared to decaying turbulence, this practice has the advantages that long stationary time series are obtained and be easily analysed. However, if the range of scales being solved is not large enough, the details of the small scales will be affected by the influence forcing has on the large motions scales, which differ (to some extent) from *natural* turbulence. Nevertheless both methods are widely used to study the physics of the small scales of turbulence.

4.2 Physical and computational parameters

The main objective of these DHIT simulations is to repeat the results Zhang *et al.* [4] obtained with a similar code and observe the same tendencies by varying some polymer parameters (*code-to-code* comparison). One Newtonian ($S1$) and two viscoelastic simulations ($S2$ and $S3$), in which the polymer solution concentration changes, are carried out to show some of the major differences between the two types of fluids. For the initial conformation field, polymers are assumed non-stretched, corresponding to $C_{ii}^0 = 1.0$.

The simulations are performed in a cubic domain with size $L_x = L_y = L_z = 2\pi$ and a grid of $N_x \times N_y \times N_z = 256 \times 256 \times 256$, the same domain used on the scientific paper in question.

The full set of simulations and the respective parameters are shown in table 4.1.

Simulation	$N_x \times N_y \times N_z$	ν	L	λ_p	β	C_{ii}^0
S1	256×256×256	10^{-2}	-	-	1.0	-
S2	256×256×256	10^{-2}	100	0.1	0.7	1.0
S3	256×256×256	10^{-2}	100	0.1	0.6	1.0

Table 4.1: Parameters for the DHIT simulations

4.3 Results

The results are based on the most meaningful parameters in DHIT and on the characteristics and influences of the polymer additives. All the quantities are non-dimensionalized, except where is mentioned otherwise. A non-dimensionalization by the initial value of each quantity is used.

The various parameters determined are presented along with the ones obtained by Zhang *et al.* [4], also non-dimensionalized. In the several graphics, they will be referred as REF. $\beta = x$, where x is the polymer solution concentration.

Starting by the Taylor microscale, it is possible to see in fig. 4.1(a) that decreases at first in the so-called energy propagation period (EPP) and then quickly grows in the energy decay period (EDP). Further, in the initial period $\lambda^{[V]} \approx \lambda^{[N]}$ (hereinafter, the superscripts 'V' represent the viscoelastic case and 'N' the Newtonian), while for the EDP $\lambda^{[V]} > \lambda^{[N]}$. Besides, between the two viscoelastic simulations, a lower value of β implies a faster growth on the Taylor microscale. The same behavior

is observed on the results withdraw from the aforementioned reference and the values are also very similar.

Next, in fig. 4.1(b), the temporal evolution of the energy dissipation rate ε is presented. In the EPP, ε begins to increase up to a peak of maximum energy dissipation, where it starts to decrease until finally approaches zero (EDP). In polymer solution cases, the inital development is very similar, but just before the peak is reached the values of ε are already lower than the Newtonian case ($\varepsilon^{[V]} < \varepsilon^{[N]}$) and remain so through the simulation (faster decay rate). This difference eventually diminishes as ε tends to zero. The smaller values of energy dissipation rate are explained by the fact that in polymer solution cases, there are two dissipative modes, one due to viscosity and other due to elasticity of the polymer additives, as opposed to one (viscosity) in the Newtonian fluids. Moreover, to a lower value of β correspond slightly lower values of ε. The results present in [4] show the same development.

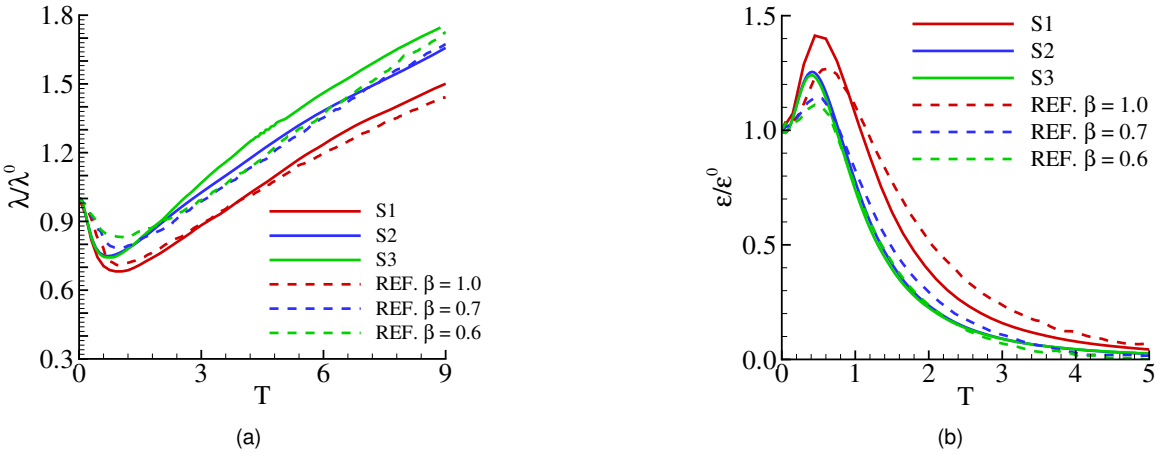

Figure 4.1: Temporal evolution of (a) the Taylor microscale (λ) and (b) the energy dissipation rate (ε), both non-dimensionalized by their initial value.

The temporal evolution of the total turbulent kinetic energy ξ can be seen in fig. 4.2(a). As it should be in DHIT, ξ is continuously decreasing. In the polymer solution cases, a larger decay rate is present during the early stage of EDP and a smaller decay rate occurs on the later stage of EDP. Therefore, the turbulent kinetic energy decays much faster with polymer additives, also meaning that higher polymer concentrations (lower β) induce slightly faster decaying rates. The same conclusions can be observed in the results of Zhang *et al.*.

Regarding the enstrophy Ω, its temporal evolution in both Newtonian and polymer solution cases are shown in fig. 4.2(b). In the initial period (EPP), Ω starts by increasing, which physically means that vortex structures are being stretched. Follows a quick decreasing of Ω, indicating the suppression and dissipation of the vortex structures. In both cases, the enstrophy in the viscoelastic fluid is much weaker compared with its Newtonian counterpart. Despite the lack of enstrophy temporal evolution for the same polymer concentrations used in this work, the results present in the previous mentioned reference show a similar evolution and difference between the two type of fluids.

The mean trace of the conformation tensor (R^2) with different concentrations is also analysed and the temporal evolution of this quantity is presented in fig. 4.3. It is possible to see that R^2 quickly grows

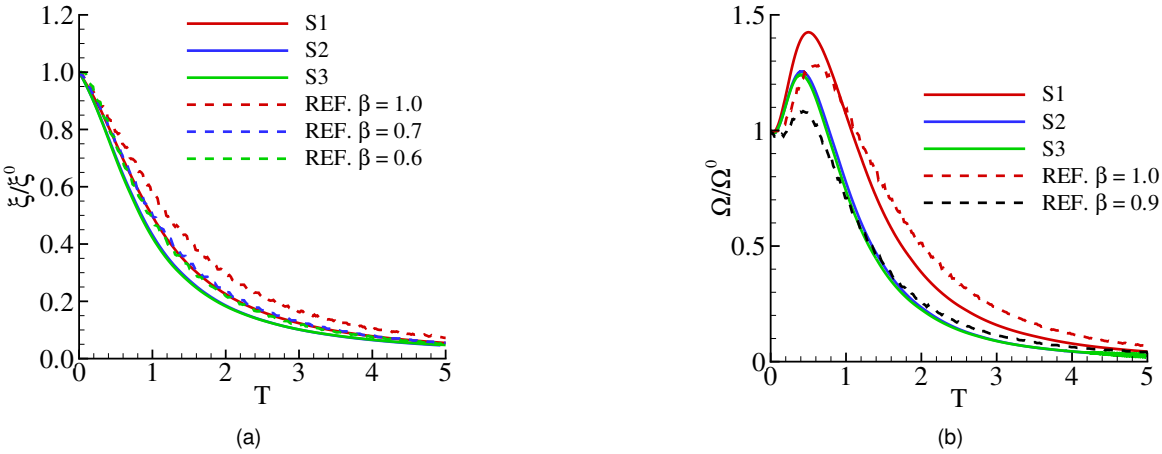

Figure 4.2: Temporal evolution of (a) the total turbulent kinetic energy (ξ) and (b) the enstrophy (Ω), both non-dimensionalized by their inital value.

due to the initial mean velocity gradients generated by turbulent fluctuations that leads to higher polymer extensions. It also shows that during the EPP the mean trace is almost the same for all concentrations and it decreases with polymer concentration (lower β) during the EDP. However, the values obtained here for R^2 are higher than the ones Zhang *et al.* presented. The reason that can explain this difference lies on the method adopted for time marching. While the authors of [4] use a second-order Adams-Bashford scheme, the code implemented in the course of this work uses a third-order Runge-Kutta scheme. This leads to different values of each quantity calculated when solving the Navier-Stokes and the conformation tensor equations. Therefore, the small discrepancies observed also on the previous graphics can have on this fact their origin. Nevertheless, the evolution of R^2 is very similar to the one present in the reference.

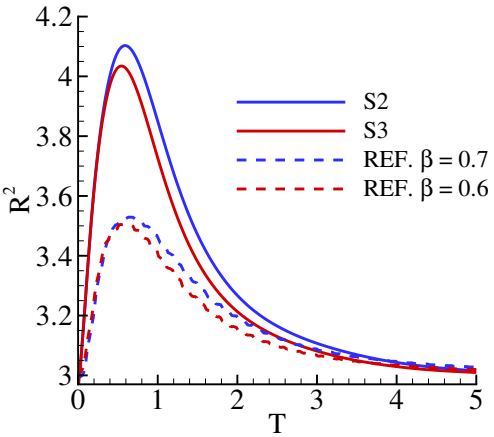

Figure 4.3: The time evolution of R^2 for different concentrations.

Finally, temporal evolution of the energy spectrum of each simulation is shown in figs. 4.4(a) to 4.4(c). Initially (EPP), the energy is transferred from small to large wavenumbers and so raises the tail of the energy spectra. Then, during the EDP, the viscous effect dominates so that the dissipation lowers the

tail of energy spectra. However, particularly in this period, the energy spectra from the viscoelastic fluid ($E(k)^V$) is different from the Newtonian one ($E(k)^N$), where $E(k)^V > E(k)^N$ at small scales. Furthermore, $E(k)^V$ keeps nearly constant at this range of scales, *i.e.*, the polymer dominant scale range. The same type of spectra are visible on the previous mentioned reference.

Overall, the results obtained from the DHIT simulations showed good agreement with the ones obtained by Zhang *et al.* [4]. The various quantities analysed allow one to infer that all range of scales are being well solved and the polymer additives particularities are also being well captured.

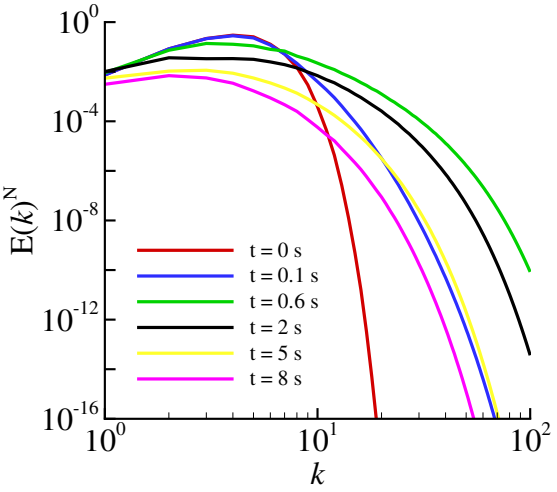

(a)

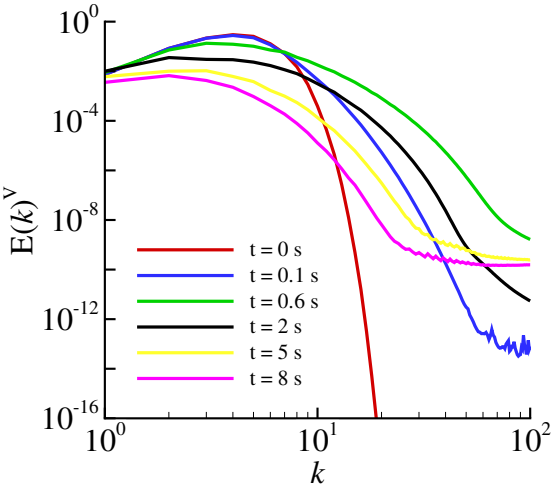

(b)

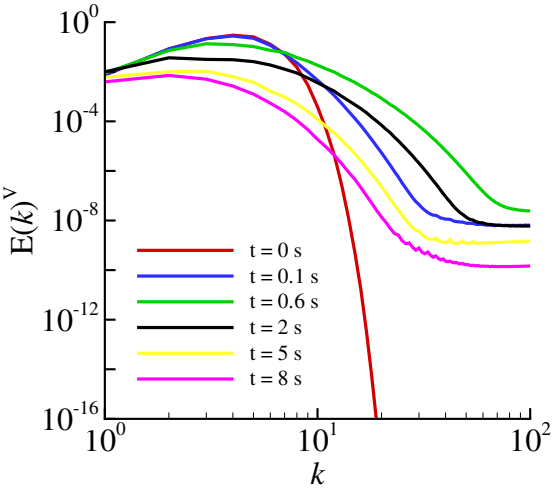

(c)

Figure 4.4: Turbulent kinetic energy spectra $E(k)$ in DHIT. (a) Newtonian fluid case $S1$; (b) polymer solution case $S2$ (c) polymer solution case $S3$.

Chapter 5

Results

This chapter presents the numerical results from the present work. The discussion is based on various simulations of a plane jet, either with viscoelastic or Newtonian fluid, and on the post-processing work. As already referred, the study is focused on the turbulent/non-turbulent (T/NT) interface and on the influence polymer additives have in the small scale characteristics of this layer. For this purpose, different simulations are performed by varying the value of the polymer solution concentration and keeping the other parameters constant. The post-processing tools produce a wide range of results, allowing a detail characterization of the phenomena taking place on that area.

The present chapter starts by a small description of the various simulations performed, complementing the information that was given in chapter 3. After this the several results obtained are presented, such as vorticity contour plots, conditional mean profiles and probability density functions (PDF's), among others.

5.1 Physical and computational parameters

The DNS were started by using, as initial condition, an hyperbolic-tangent velocity profile (see section 3.7.1), since it is recognized that it represents a very good approximation to the inlet velocity profile found in measured experimental jets. The initial Reynolds number is equal to $Re_H = (U_2 - U_1)H/\nu = 3200$ and the inital $H/\theta_0 = 35$, in order to accelerate the transition phase (section 3.7.1).

Besides, to allow the code to solve all the range of scales (until close to the Kolmogorov microscale), the computational box measures $(L_x, L_y, L_z) = (4H, 6H, 4H)$. The grid size consists in $(N_x \times N_y \times N_z) = (256 \times 384 \times 256)$ grid points. It is important to point out that the grid is isotropic, *i.e.*, $\Delta x = \Delta y = \Delta z = 0.0156H$, and that the computational box does not constrain the jet in its development and spreading rate. In the streamwise direction, one must ensure that the computational domain in this direction is big enough to allow the development of the primary Kelvin-Helmoltz instability. The Strouhal number is equal to $Str_\theta = f_0\theta_0/U_0 = 0.0165$ (section 2.1.5) and since $H/\theta_0 = 35$, the associated instability length scale is equal to $\lambda_{sl} = \theta_0/Str_\theta = 1.73H$. Thus, the box size in the streamwise direction is more than two times bigger than the Kelvin-Helmoltz instability length scale. Concerning the other directions,

numerous previous works [12] have showed that there is no particular problem with the size of the box in the normal direction and that usually the spanwise direction has smaller sizes. Therefore, the box size used in the present simulations is indeed sufficient.

The parameters for all simulations are presented in table 5.1.

Simulation	$N_x \times N_y \times N_z$	ν	L	λ_p	β	C_{ii}^0
JET1	256×384×256	10^{-2}	-	-	1.0	1.0
JET2	256×384×256	10^{-2}	100	0.1	0.7	1.0
JET3	256×384×256	10^{-2}	100	0.1	0.6	1.0

Table 5.1: Plane jet simulations parameters

5.2 T/NT interface detection

In the present work, the T/NT interface is defined by using the vorticity norm $\omega = (\omega_i\omega_i)^{1/2}$. It was observed that the detection threshold of $\omega = 0.7U_2/H$ best delineated the vortical regions. Figure 5.1 shows contours of vorticity modulus corresponding to this threshold in an (x, y) plane of the jet at $T/T_{ref} = 12$, for each simulation. This instant is located in the far-field and in fully developed turbulent regime. It can be seen that the T/NT interface is strongly contorted and between Newtonian and viscoelastic fluid there are no major large scale differences, apart from the more intense vortices in the Newtonian fluid.

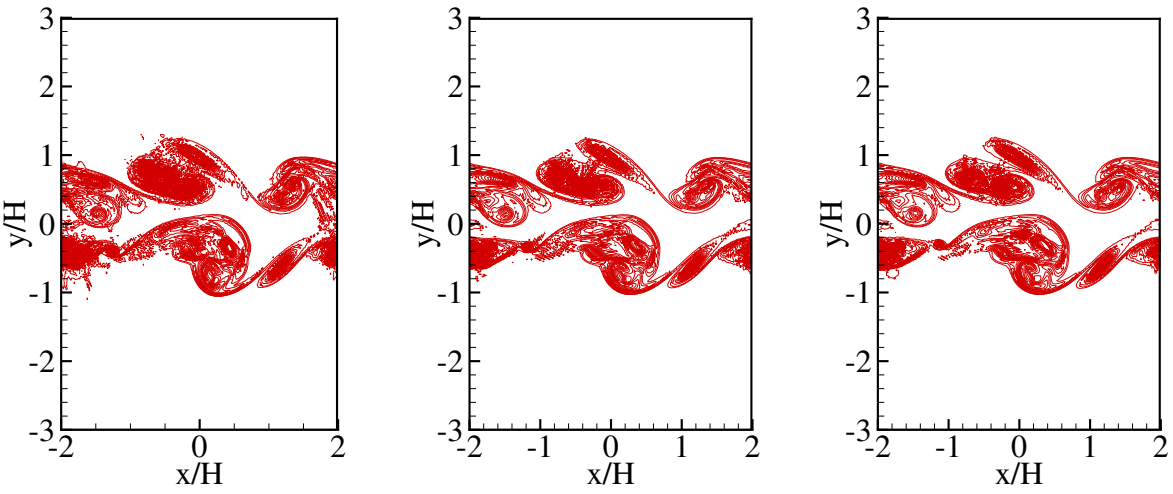

(a) JET1 (b) JET2 (c) JET3

Figure 5.1: Countors of vorticity modulus corresponding to $\omega = 0.7U_2/H$ in the (x, y) plane of the various jets at $T/T_{ref} = 12$.

To study the turbulent entrainment, conditional statistics are analysed in relation to the location of the interface envelope by using a procedure similar to the one described in [12]. It starts with the determination of the T/NT interface envelope location $Y_I(x)$, for each one of the N_x grid points in the original coordinate system along the x direction. $Y_I(x)$ is obtained through a linear interpolation along

the y direction, using the vorticity norm threshold indicated above to detect the T/NT interface. A new coordinate system (x_I, y_I) is defined with the lines tangent (x_I) and normal (y_I) to the interface envelope (fig. 5.2). In this new coordinate system, the T/NT interface is exactly at $(x_I, y_I) = (0, 0)$, the flow is turbulent for $y_I > 0$ and irrotational for $y_I < 0$.

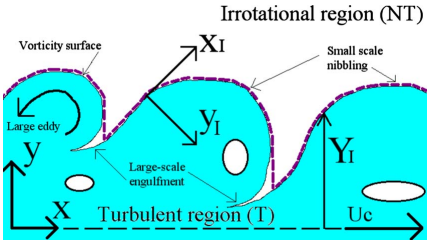

Figure 5.2: Sketch of the T/NT interface for the plane jet indicating the vorticity surface (solid line) and the interface envelope (gray dashed lines). The new coordinate system used to analyse the T/NT interface (x_I, y_I) is also visible. The three holes represent regions of irrotational fluid inside the turbulent region.

Along both sides of this y_I line, $N_I = 120$ points are defined, starting $y_I = 0$ and equally spaced with a distance equal to the mesh size Δx. This defines a total of $2 \times N_I - 1 = 239$ grid coordinates for the y_I axis that will be used to display the mean conditional profiles. For each coordinate y_I, the mean conditional profile of a given flow variable $P(x, y, z, t)$, in the upper shear layer, for the plane (x, y) corresponding to $z = Z$ and at time $t = T$ is obtained by interpolating the value of $P(x, y, z, t)$ into the point $(x_I, y_I) = (0, y_I)$. In this case, a simple bilinear interpolation is used for the purpose. All the points inside 'holes' of irrotational fluid that appear in the jet are removed from the statistical sample.

The procedure just described is also used for the lower shear layer and the resulting profiles are averaged in the end. This is done for each one of the (x, y) planes available and the final results are once again averaged over all the existing N_z planes.

5.3 Conditional mean vorticity

Figure 5.3 shows mean conditional profiles of $\langle|\omega_z|\rangle_I$ (non-dimensionalized by U_2/H) in relation to the distance from the T/NT interface y_I, which is non-dimensionalized by the value of the Kolmogorov microscale at the jet shear layer. This quantity shows a sharp transition from the irrotational to the turbulent zone, in both types of fluid, and a peak very close to the interface. However, it is perceptible that this peak value (and also inside the turbulent region) is lower for viscoelastic fluids. This allows one to do a first conclusion, that the turbulence in a fluid with polymer additives is less intense.

Based on this profile, three particular locations in relation to the distance from the T/NT interface are considered: $y_I/\eta = 0.0$, exactly at the T/NT interface, $y_I/\eta = 19.9$, which is close to the point of maximum $\langle|\omega_z|\rangle_I$, and $y_I/\eta = 64.7$, a point that is already well inside the turbulent zone.

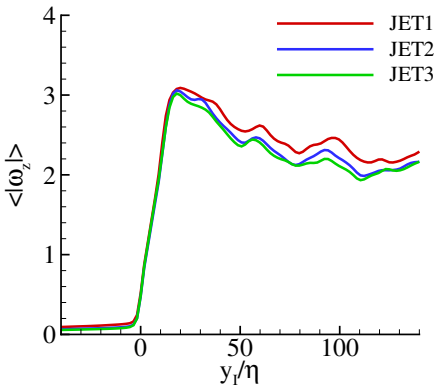

Figure 5.3: Mean conditional profiles of $\langle|\omega_z|\rangle_I$ (normalized by U_2/H).

5.4 Analysis of the invariants Q_W and Q_S

In fig. 5.4 are presented conditional mean profiles of the second invariant of the rate-of-strain tensor Q_S and the invariant of the rate-of-rotation tensor Q_W in relation to the distance from the T/NT interface, along with the profile for the vorticity component $\langle|\omega_z|\rangle_I$ and the symbols marking the three locations mentioned above. The analysis of this quantities helps to understand the geometry of the dissipation.

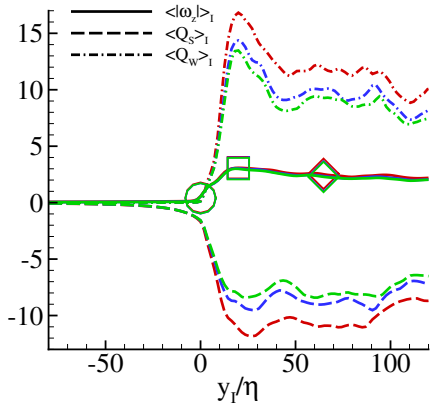

Figure 5.4: Conditional mean profiles in relation to the distance from the T/NT interface for $\langle Q_S\rangle_I$ and $\langle Q_W\rangle_I$. The conditional mean profile $\langle|\omega_z|\rangle_I$ is also shown and the symbols mark: (◯) $y_I/\eta = 0$ - T/NT interface, (□) $y_I/\eta = 19.9$ - point of maximum $\langle|\omega_z|\rangle_I$, and (◇) $y_I/\eta = 64.7$ - well inside the turbulent region. Simulations JET1, JET2 and JET3 are represented by the red, blue and green lines, respectively.

Both invariants display quick changes near the interface, following the behavior of $\langle|\omega_z|\rangle_I$. Starting with the invariant $Q_W = \Omega_{ij}\Omega_{ij}/2$, it is negligible in the irrotational flow region ($y_I/\eta < 0$) and steeply rises once the T/NT interface has been crossed ($y_I/\eta = 0$). In the turbulent region ($y_I/\eta > 0$), a peak value is reached and then it appears to stabilize around a small interval of values when well inside this region. The conditional mean profile of $\langle Q_S\rangle_I$ begins by being negligible in the irrotational region and far away from the T/NT interface. Then, around $y_I/\eta \approx -50$, the absolute value of $\langle Q_S\rangle_I$ starts to increase until very close to the interface where it reaches a non-negligible value (at $y_I/\eta \approx -20, \langle Q_S\rangle_I \approx -0.44(U_2/H)^2$). Once the T/NT interface is crossed, the absolute value of $\langle Q_S\rangle_I$ increases at a faster

rate than before, reaching its turbulent gap of values.

The interesting thing here is that the polymer influence does not manifest itself until crossing the T/NT interface, since the mean profile evolution is exactly the same for $y_I/\eta < 0$, regardless the type of fluid. Even for $\langle Q_S \rangle_I$, that begins to grow before the interface, in the viscoelastic fluid the same behavior is verified. However, as soon as the T/NT interface has been crossed, the polymer immediately alters the evolution of both $\langle Q_S \rangle_I$ and $\langle Q_W \rangle_I$, it causes a lower increase rate. Since $\langle Q_S \rangle_I = -\langle S_{ij} S_{ij} \rangle_I / 2$ is proportional to the dissipation rate, this means that the mechanism of viscous dissipation is altered during the turbulent entraiment process. Moreover, $Q_W = \Omega_{ij} \Omega_{ij} / 2$ is proportional to the enstrophy density and the lower values verified in the viscoelastic fluids confirms that turbulence is less intense with polymer additives.

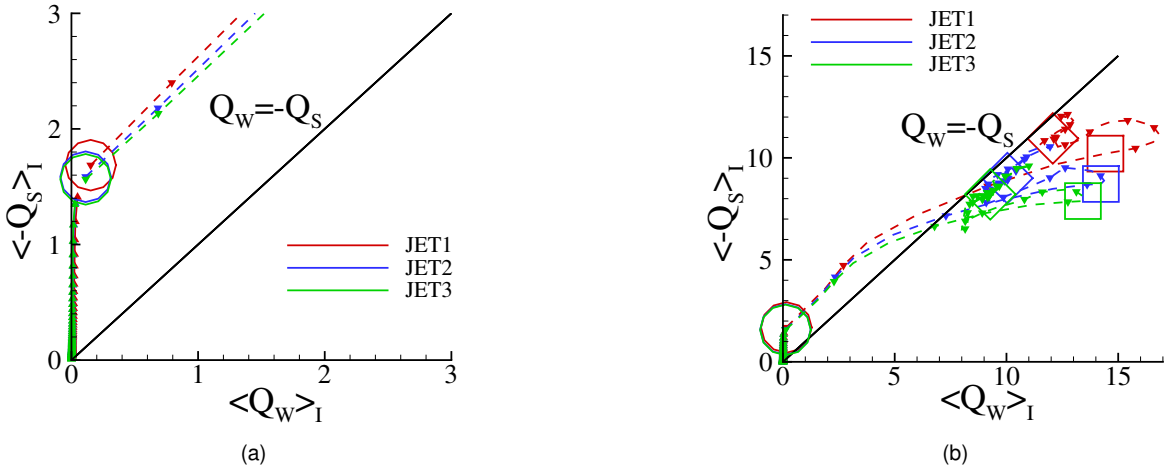

Figure 5.5: Trajectories of the conditional mean values of $\langle Q_S \rangle_I$ and $\langle Q_W \rangle_I$ in their associated phase map. The solid line and solid triangles indicate points in the irrotational region $y_I/\eta < 0$ and the dashed line and solid inverted triangles indicate points in the turbulent region $y_I/\eta \geq 0$. The symbols mark: (◯) $y_I/\eta = 0$, (□) $y_I/\eta = 19.9$, and (◊) $y_I/\eta = 64.7$.

Figures 5.5(a) and 5.5(b) show the trajectory of the mean values of $\langle Q_W \rangle_I$ and $\langle -Q_S \rangle_I$ in their associated phase map. In the irrotational region, the mean values of the invariants are near the vertical line defined by $\langle Q_W \rangle_I = 0$. This represents flow points with high dissipation but little enstrophy, causing the mean geometry of the dissipation at the T/NT interface to be characterized by irrotational dissipation. The interface region is crossed at $\langle Q_W \rangle_I \approx 0.2$ and $\langle -Q_S \rangle_I \approx 1.7$, for the Newtonian fluid, and for the viscoelastic fluid at $\langle Q_W \rangle_I \approx 0.1$ and $\langle -Q_S \rangle_I \approx 1.6$. The flow then detaches from the vertical line and approaches $\langle Q_W \rangle_I = \langle -Q_S \rangle_I$, indicating a predominance of vortex sheets in the flow inside the turbulent region. In the middle, when it reaches the point of maximum $\langle |w_z| \rangle_I$, the flow topology is a mix between irrotational dissipation and vortex sheets, since it is between the lines of $\langle Q_W \rangle_I = 0$ and $\langle Q_W \rangle_I = \langle -Q_S \rangle_I$. Besides, after the irrotational region, the differences between the two viscoelastic flows are more pronounced, even with a small change in the polymer concentration (JET2 - $\beta = 0.7$ and JET3 - $\beta = 0.6$).

Figures 5.6 to 5.8 present joint PDFs of $(Q_W, -Q_S)$ for the three simulations and at the three particular locations used before. At the T/NT interface $(y_I/\eta = 0)$ the joint PDF shows a marked tendency to

be aligned with the vertical line defined by Q_W, which attests the previous conclusions, that irrotational dissipation dominates.

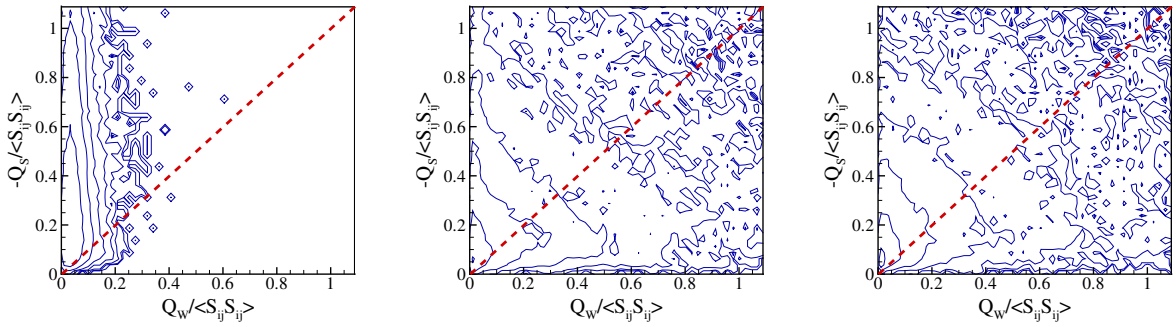

(a) $y_I/\eta = 0$ (b) $y_I/\eta = 19.9$ (c) $y_I/\eta = 64.7$

Figure 5.6: Joint PDFs of Q_W and $-Q_S$ for simulation JET1. The contour levels are 0.01, 0.03, 0.1, 0.3, 1.3, 10 and 30.

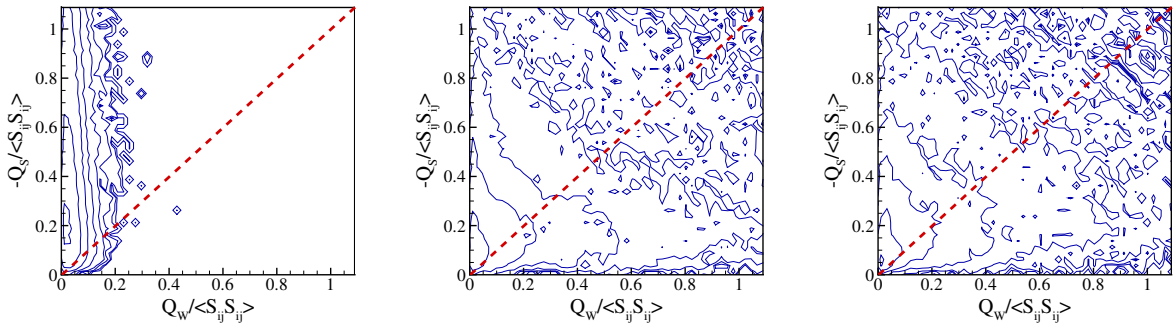

(a) $y_I/\eta = 0$ (b) $y_I/\eta = 19.9$ (c) $y_I/\eta = 64.7$

Figure 5.7: Joint PDFs of Q_W and $-Q_S$ for simulation JET2. The contour levels are the same as in fig. 5.6.

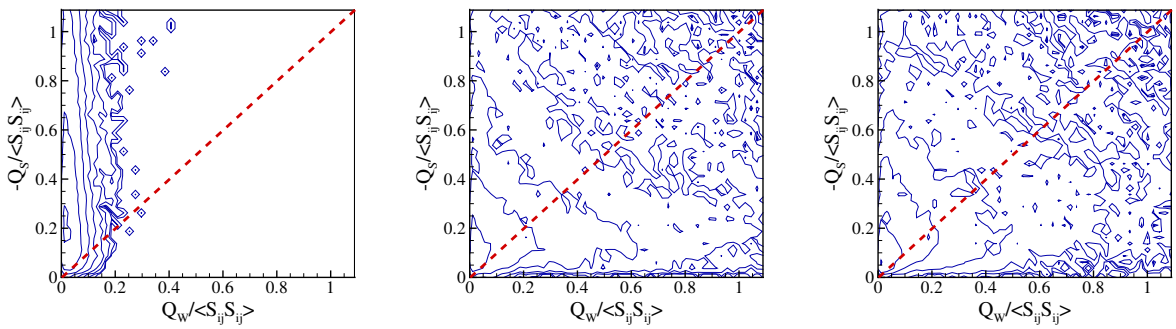

(a) $y_I/\eta = 0$ (b) $y_I/\eta = 19.9$ (c) $y_I/\eta = 64.7$

Figure 5.8: Joint PDFs of Q_W and $-Q_S$ for simulation JET3. The contour levels are the same as in fig. 5.6.

In the viscoelastic cases, it is possible to see that the more probable values are more closely clustered in the centre of the joint PDF, implying a predominance of smaller gradients than in the Newtonian case.

5.5 Analysis of the invariants Q_S and R_S

In order to analyse the geometry of straining of the fluid elements, the second and third invariants of the rate-of-strain tensor Q_S and R_S are investigated near the T/NT interface. Figure 5.9 displays mean profiles of these invariants in relation to the distance from the T/NT interface. The conditional mean profile of $\langle|\omega_z|\rangle_I$ is also present and the symbols marking the three locations: $y_I/\eta = 0, 19.9$, and 64.7. The profile of $\langle R_S\rangle_I$ was not represented in fig. 5.4 to avoid difficulties on the visualization of all quantities. Therefore, the profiles of $\langle Q_S\rangle_I$ and $\langle|\omega_z|\rangle_I$ are here repeated.

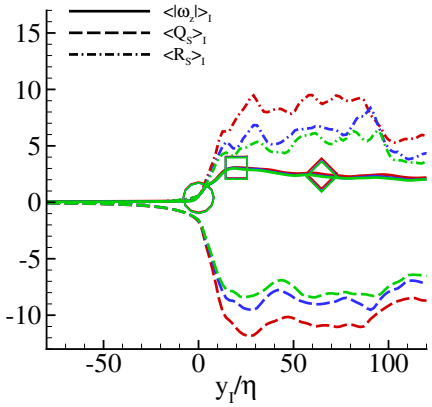

Figure 5.9: Conditional mean profiles in relation to the distance from the T/NT interface for $\langle Q_S\rangle_I$ and $\langle R_S\rangle_I$. The conditional mean profile $\langle|\omega_z|\rangle_I$ is also shown and the symbols mark: (◯) $y_I/\eta = 0$ - T/NT interface, (□) $y_I/\eta = 19.9$ - point of maximum $\langle|\omega_z|\rangle_I$, and (◇) $y_I/\eta = 64.7$ - well inside the turbulent region. Simulations JET1, JET2 and JET3 are represented by the red, blue and green lines, respectively.

The evolution of the mean invariant $\langle Q_S\rangle_I$ was already described in section 5.4. As for $\langle R_S\rangle_I$, it starts by being negligible for $y_I/\eta < 0$, but when the T/NT interface is crossed, this quantity starts to grow until reach its interval of turbulent values. By adding the polymer, the increase rate of $\langle R_S\rangle_I$ becomes even lower, diminishing the deformation of the fluid elements.

In figs. 5.10(a) and 5.10(b) the trajectories of the mean values of $\langle Q_S\rangle_I$ and $\langle R_S\rangle_I$ are shown, in their associated phase map. For the entire flow region, the invariants are always in the zone of $\langle R_S\rangle_I > 0$ and $\langle Q_S\rangle_I < 0$, meaning that the mean flow geometry is related with expansion of the fluid elements. In the irrotational region, the mean flow topology is $3:1:-4$ (sheetlike structures) and then starts changing to $2:1:-3$ between the T/NT interface and the point of maximum $\langle|\omega_z|\rangle_I$. However, just before this location, the flow geometry turns again into $3:1:-4$ and there it stays until well inside the turbulent region. As before, associated to the viscoelastic fluids are lower values of $\langle Q_S\rangle_I$ (discussed in the previous section) and $\langle R_S\rangle_I$, but the invariants trajectory is proportionally the same. This means that the fluid elements deform less but in same way and shape on both fluids.

The joint PDFs of (R_S, Q_S) at the three particular locations used before ($y_I/\eta = 0$, 19.9, and 64.7) and for the three simulations can be seen in figs. 5.11 to 5.13. There is a predominance in the region of $R_S > 0$ and $Q_S < 0$, associated to extensive straining. The more frequent values are preferable aligned toward $2:1-3$. The smaller scales seem associated with the axisymmetric extension ($1:1:-2$).

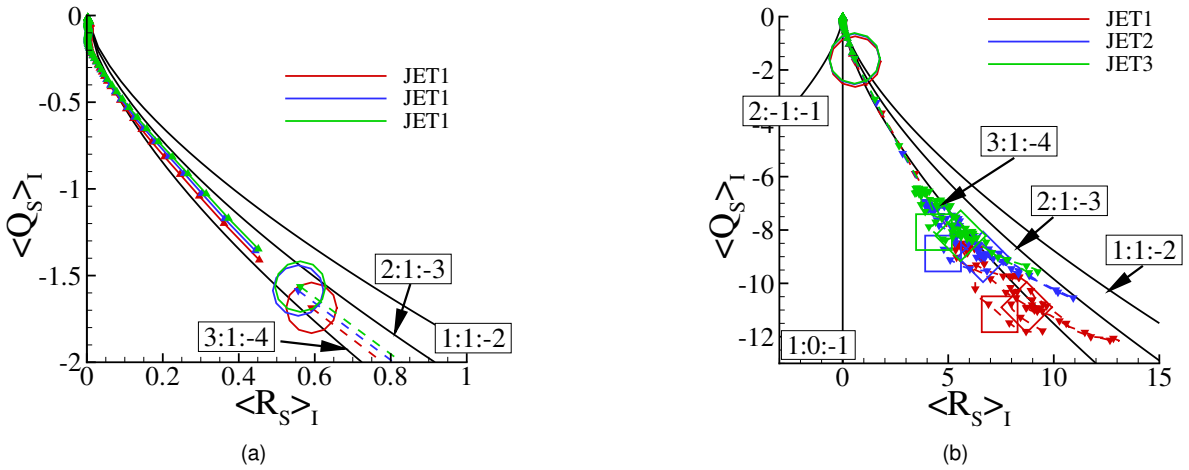

Figure 5.10: Trajectories of the conditional mean values of $\langle R_S \rangle_I$ and $\langle Q_S \rangle_I$ in their associated phase map. The solid line and solid triangles indicate points in the irrotational region $y_I/\eta < 0$ and the dashed line and solid inverted triangles indicate points in the turbulent region $y_I/\eta \geq 0$. The symbols mark: (◯) $y_I/\eta = 0$, (□) $y_I/\eta = 19.9$, and (◊) $y_I/\eta = 64.7$.

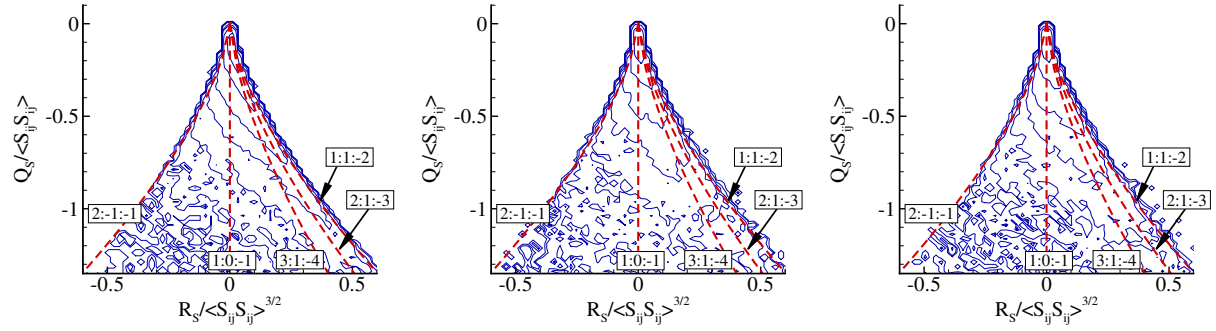

(a) $y_I/\eta = 0$ (b) $y_I/\eta = 19.9$ (c) $y_I/\eta = 64.7$

Figure 5.11: Joint PDFs of R_S and Q_S for simulation JET1. The contour levels are 0.01, 0.03, 0.1, 0.3, 1.3, 10 and 30.

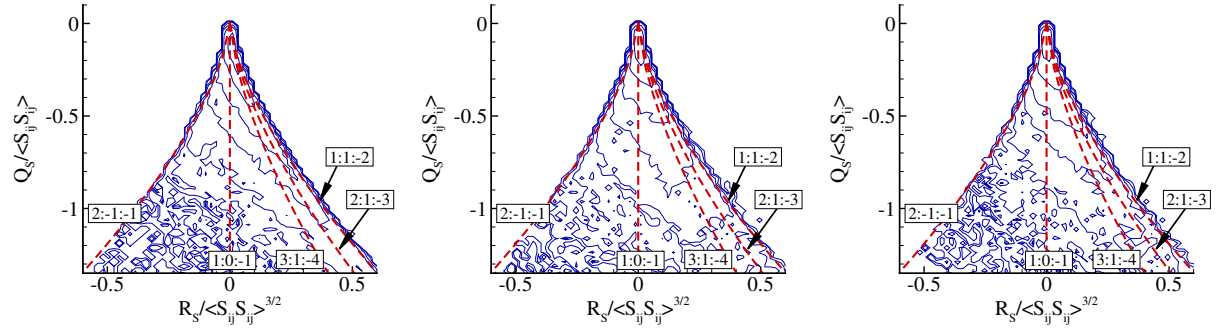

(a) $y_I/\eta = 0$ (b) $y_I/\eta = 19.9$ (c) $y_I/\eta = 64.7$

Figure 5.12: Joint PDFs of R_S and Q_S for simulation JET2. The contour levels are the same as in fig. 5.11.

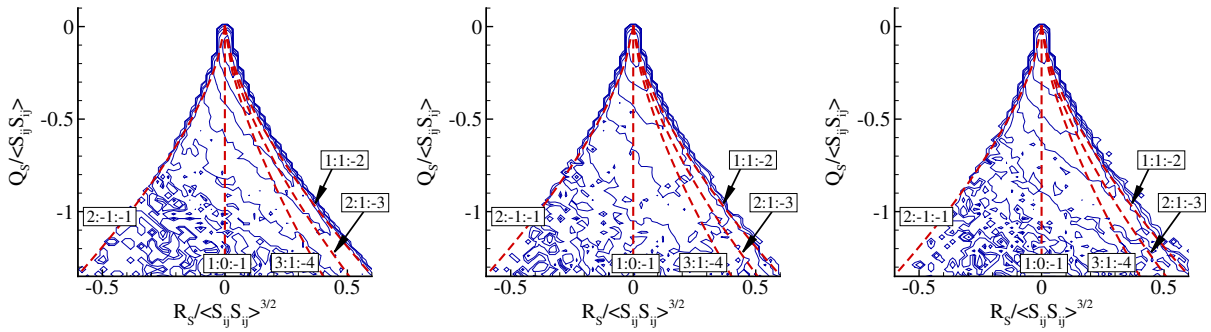

(a) $y_I/\eta = 0$ (b) $y_I/\eta = 19.9$ (c) $y_I/\eta = 64.7$

Figure 5.13: Joint PDFs of R_S and Q_S for simulation JET3. The contour levels are the same as in fig. 5.11.

5.6 Analysis of the invariants Q and R

The second and third invariants of the velocity gradient tensor, Q and R, allow to analyse the relation between the flow topology and dynamics. Conditional mean profiles of this quantities in relation to the T/NT interface are shown in fig. 5.14. Once again, the mean profile of $\langle|\omega_z|\rangle_I$ and the symbols marking $y_I/\eta = 0, 19.9$, and 64.7 are also presented.

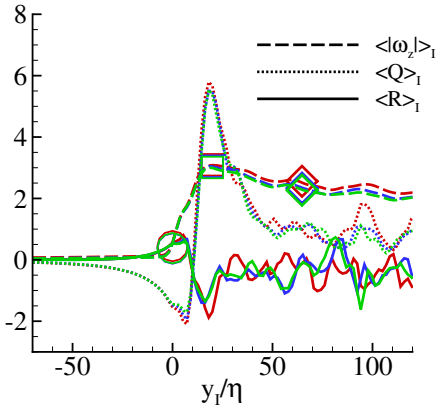

Figure 5.14: Conditional mean profiles in relation to the distance from the T/NT interface for $\langle Q\rangle_I$ and $\langle R\rangle_I$. The conditional mean profile $\langle|\omega_z|\rangle_I$ is also shown and the symbols mark: (◯) $y_I/\eta = 0$ - T/NT interface, (□) $y_I/\eta = 19.9$ - point of maximum $\langle|\omega_z|\rangle_I$, and (◊) $y_I/\eta = 64.7$ - well inside the turbulent region. Simulations JET1, JET2 and JET3 are represented by the red, blue and green lines, respectively.

In the irrotational region, the conditional mean profile of $\langle Q\rangle_I$ takes negative values ($\langle Q\rangle_I < 0$). Since $Q = (\omega_i\omega_i - 2S_{ij}S_{ij})/4$ and in this region there is virtually no vorticity, the evolution of $\langle Q\rangle_I$ is dominated by the strain product ($\langle Q\rangle_I \approx \langle Q_S\rangle_I$). Therefore, its evolution is not surprising. Just after the T/NT interface, $\langle Q\rangle_I$ reaches a minimum of $\langle Q\rangle_I \approx -2.0$, -1.9 and -1.7 at $y_I/\eta \approx 8$ respectively for JET1, JET2 and JET3. From this point onward, the enstrophy dominates over strain product, because it grows at a lower rate (see $\langle R_S\rangle_I$) than the vorticity (hence enstrophy), and a maximum at about $y_I/\eta \approx 20$ is achieved. Next, a decrease is verified. Differently, the invariant $R = -[S_{ij}S_{ik}S_{ki} + (3/4)\omega_i\omega_j S_{ij}]/3$ is negligible until just before the T/NT interface. At $y_I/\eta = 15$, $\langle R\rangle_I$ begins to be non-negligible ($\langle R\rangle_I =$

$0.1(U_2/H)^3$), due to strain production (the vorticity is still virtually zero at this point). After the T/NT interface, $\langle R\rangle_I$ reaches a positive maximum of $\langle R\rangle_I \approx 0.8(U_2/H)^3$, $0.7(U_2/H)^3$ and $0.6(U_2/H)^3$ at $y_I/\eta \approx 6$, respectively for simulations JET1, JET2 and JET3 (the higher polymer concentration, lower the value). Afterwards, $\langle R\rangle_I$ decreases to a minimum $\langle R\rangle_I \approx -1.9(U_2/H)^3$, $-1.4(U_2/H)^3$ and $-1.4(U_2/H)^3$ at $y_I/\eta \approx 18$, 16 and 14, respectively for JET1, JET2 and JET3. An increase to zero would now be expected, but instead fluctuations around a negative value are visible.

Figures 5.15(a) and 5.15(b) display the trajectory of the mean values of $\langle Q\rangle_I$ and $\langle R\rangle_I$ in the respective phase map. In the irrotational flow region, the mean invariants stay at the origin ($\langle R\rangle_I \approx 0$ and $\langle Q\rangle_I \approx 0$) of the map. Approaching the T/NT interface makes the invariants to move away and become more distant from the origin, towards the region of $\langle R\rangle_I > 0$ and $\langle Q\rangle_I < 0$, associated with straining of fluid elements. After the T/NT interface, the mean flow topology quickly moves to the region dominated by vortex stretching ($\langle R\rangle_I < 0$ and $\langle Q\rangle_I > 0$). The point of maximum $\langle|\omega_z|\rangle_I$ is located in this area, indicating a relation with maximum values of vortex stretching that occur during the turbulent entrainment. For last, the mean invariants go back to the region near the origin of the phase map, as expected, since the mean values of $\langle R\rangle_I < 0$ and $\langle Q\rangle_I > 0$) in the center of the jet shear layer behave as isotropic turbulence (are near zero).

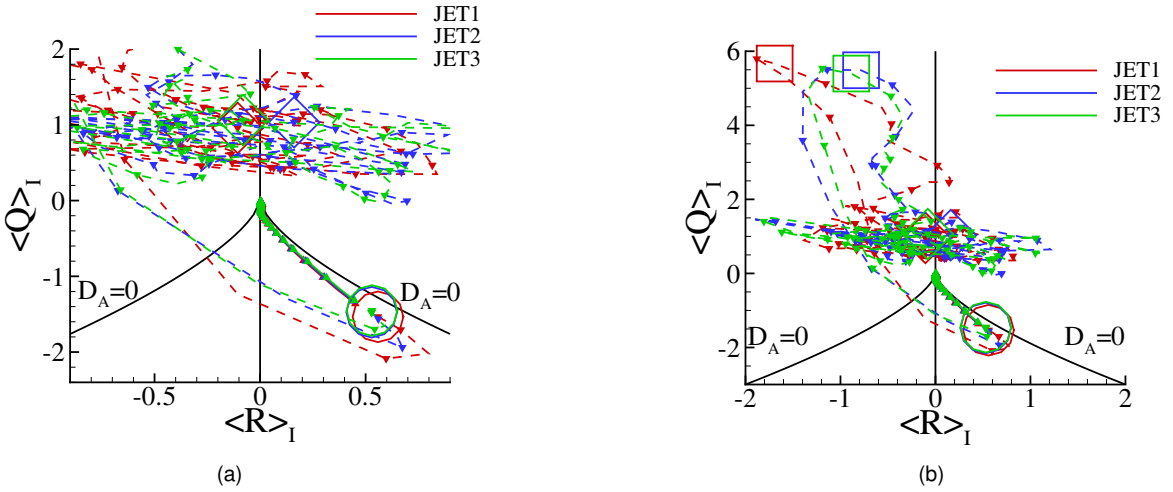

Figure 5.15: Trajectories of the conditional mean values of $\langle R\rangle_I$ and $\langle Q\rangle_I$ in their associated phase map. The solid line and solid triangles indicate points in the irrotational region $y_I/\eta < 0$ and the dashed line and solid inverted triangles indicate points in the turbulent region $y_I/\eta \geq 0$. The symbols mark: (◯) $y_I/\eta = 0$, (□) $y_I/\eta = 19.9$, and (◇) $y_I/\eta = 64.7$.

However, in the figures there is a large dispersion of points on both sides of the map which makes very difficult to see the trajectory. A solution for this problem is to increase the number of samples used in the conditional statistics. In the fully developed turbulent regime, each instantaneous field is statistically equivalent. Thefore, by taking other fields it would still be in the same turbulent regime and the trajectory of the mean values would be better converged. Nevertheless, a few thoughts on the differences between viscoelastic and Newtonian fluids can be withdraw. One more time, the polymer additives restrain the normal development of the mean conditional values, but opposed to the previous quantities, the differences are less significative. The maximum and minimum values are indeed lower

and higher, respectively, within a viscoelastic fluid, but the evolution is pratically the same, except inside the turbulent zone, where the convergence is not very good.

Joint PDFs of (R, Q) for the three simulations and at the previous mentioned locations are shown in figs. 5.16 to 5.18. The teardrop characteristic shape of the (R, Q) map cannot be seen at the T/NT interface $(y_I/\eta = 0)$. In line with the results described before, the values of R and Q exist only below the lines defined by the discriminant $D_A = 0$, but the contour lines are already aligned with this line. At the points of maximum $\langle|\omega_z|\rangle_I$ and deep inside the turbulent region, the joint PDFs show the teardrop shape, correlating Q and R in two regions: $R > 0$ and $Q < 0$ associated to biaxial stretching and $R < 0$ and $Q > 0$, where enstrophy production by vortex stretching is predominant.

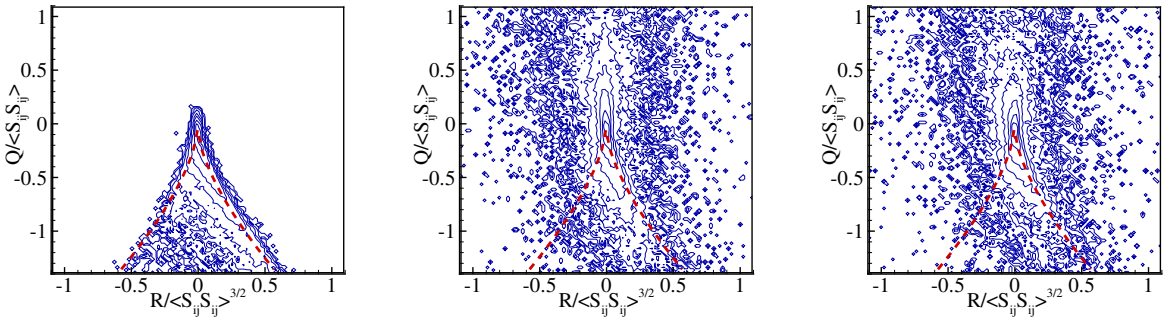

(a) $y_I/\eta = 0$ (b) $y_I/\eta = 19.9$ (c) $y_I/\eta = 64.7$

Figure 5.16: Joint PDFs of R and Q for simulation JET1. The contour levels are 0.01, 0.03, 0.1, 0.3, 1.3, 10 and 30.

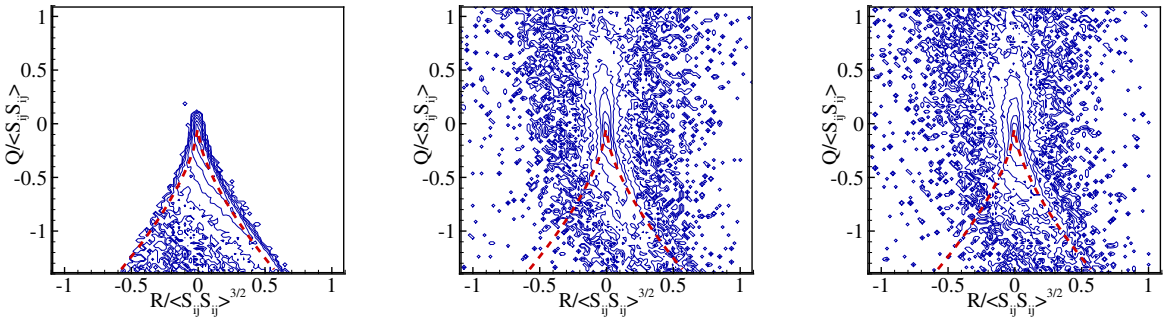

(a) $y_I/\eta = 0$ (b) $y_I/\eta = 19.9$ (c) $y_I/\eta = 64.7$

Figure 5.17: Joint PDFs of R and Q for simulation JET2. The contour levels are the same as in fig. 5.16.

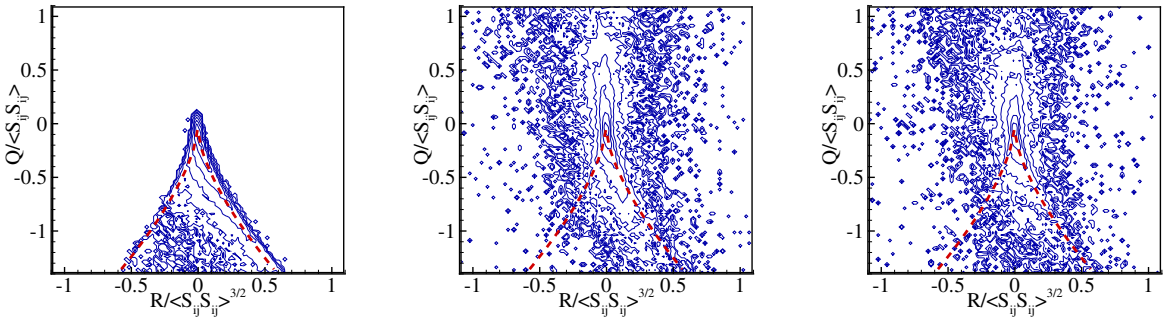

(a) $y_I/\eta = 0$ (b) $y_I/\eta = 19.9$ (c) $y_I/\eta = 64.7$

Figure 5.18: Joint PDFs of R and Q for simulation JET3. The contour levels are the same as in fig. 5.16.

Chapter 6

Conclusions

6.1 Concluding remarks

In the present work, direct numerical simulations of turbulent viscoelastic jets were undertaken in order to assess the small scale turbulent characteristics during the process of turbulent entrainment in jets.

The work consisted in the implementation of the FENE-P model into a pseudo-spectral Navier-Stokes solver. The FENE-P model was thoroughly analysed and tested using decaying viscoelastic turbulence.

After this, direct numerical simulations were carried out in order to analyse the small scale characteristics in viscoelastic jets near the turbulent/non-turbulent interface of the jet. Specifically, the study addressed geometry of the dissipation, the geometry of the straining and the relation between vortex stretching and geometry of the fluid elements. These points were assessed through the computation of conditional profiles of the invariants of the velocity gradient, rate-of-strain and rate-of-rotation tensors.

The principal conclusion from this study is that, somehow surprisingly, the introduction of polymer additives in a turbulent flow does not cause significant changes for these invariants. The numerical results from the present work showed that the viscoelastic turbulent jet maintains most of its characteristics compared to the newtonian jet. However, it was possible to detect some subtle discrepancies regarding the most intense gradients observed for the small scales.

From the large scales point of view, the vorticity contour plots showed that externally the Newtonian and viscoelastic jets are very similar. The observed difference concerns the magnitude of the vortices surrounding the T/NT interface. For the viscoelastic fluids, smaller vorticity magnitudes are observed.

In some sense polymer chains can be interpreted as a secondary dissipation mode, which is different from the classic viscous mode. The polymer molecules have the capability to absorve and inhibit the steep gradients that are predominant at the small scales, leading to relatively smaller values of total kinetic energy in the whole flow. Finally, it is also important to mention that a small change on the polymer concentration causes a considerable change between two viscoelastic flows.

6.2 Achievements

A code to simulate viscoelastic flows was implemented and verified against a decaying homogeneous isotropic turbulence (DHIT) simulation. Three large direct numerical simulations (DNS) of a plane jet were carried out, one with Newtonian fluid and the other two with viscoelastic fluids of different polymer concentrations.

The role of the polymer additives on the turbulent entrainment near the turbulent/non-turbulent interface was analysed by using conditional statistics and the invariants of the velocity gradient, rate-of-strain and rate-of-rotation.

The development of this work originated an article published in a national congress on computational fluid mechanics and currently another one is being written to be submitted to an international scientific journal.

6.3 Future work

As future work, the results obtained with this viscoelastic model should be benchmarked with experimental results, in order to confirm or detect any problem with the polymer model or the code implemented.

On the other side, the algorithm used to solve the conformation tensor equation should be improved in terms of computational speed and cost, since it has to solve six more variables than the Newtonian case. Besides, the process to choose the correct derivative for the stretching term of the conformation tensor equation (section 3.4.4) is very slow. Therefore, one way to enhance the calculus speed is to parallelize the code.

Moreover, to improve the convergence of the conditional statistics during the post-processing phase, the use of more instantaneous fields is advised.

The influence of other polymer parameters (relaxation time, maximum extension) on the small scales and turbulent entrainment should also be assessed, as well as compare the results using other polymer chain models.

References

[1] B.A. Toms. Some observation on the flow of linear polymer solutions through straight tubes at large Reynolds number. *Proceedings of First Internacional Congress on Rheology*, 2:135–141, 1948.

[2] R.H. Nadolink and W.W. Haigh. Bibliography on skin friction reduction with polymers and other boundary-layers additives. *Applied Mechanics Review*, 48:351, 1995.

[3] C.D. Dimitropoulos, Y. Dubief, E.S.G. Shaqfeh, P. Moin and S.K. Lele. Direct numerical simulation of polymer-induced drag reduction in turbulent boundary layer flow. *Physics of Fluids*, 17:011705, 2005.

[4] W.-H. Cai, F.-C- Li and H.-N. Zhang. DNS study of decaying homogeneous isotropic turbulence with polymer additives. *Journal of Fluid Mechanics*, 665:334–356, 2010.

[5] E. De Angelis, C. Casciola, R. Benzi and R. Piva. Homogeneous isotropic turbulence in dilute polymers. *Journal of Fluid Mechanics*, 531:1–10, 2005.

[6] C.M. White and M.G. Mungal. Mechanics and prediction of turbulent drag reduction with polymer additives. *Annual Review of Fluid Mechanics*, 40:235–256, 2008.

[7] T. Vaithianathan, A. Robert, J.G. Brasseur and L.R. Collins. An improved algorithm for simulating three-dimensional, viscoelastic turbulence. *Journal of Non-Newtonian Fluid Mechanics*, 140:3–22, 2006.

[8] T. Vaithianathan and L.R. Collins. Numerical approach to simulating turbulent flow of a viscoelastic polymer solution. *Journal of Computational Physics*, 187:1–21, 2003.

[9] S. Jin. Numerical simulations of dilute polymer solution in isotropic turbulence. PhD thesis, Cornell University, USA, 2007.

[10] P. Perlekar, D. Mitra and R. Pandit. Manifestations of Drag Reduction by Polymer Additives in Decaying, Homogeneous, Isotropic Turbulence. *Physical Review Letters*, 97:264501, 2006.

[11] C. Kalelkar, R. Govindarajan and R. Pandit. Drag reduction by polymer additives in decaying turbulence. *Physical Review E*, 72:017301, 2005.

[12] C.B. da Silva and J.C.F. Pereira. Invariants of the velocity-gradient, rate-of-strain, and rate-of-rotation tensors across the turbulent/nonturbulent interface in jets. *Physics of Fluids*, 20:055101, 2008.

[13] A. Ooi, J. Martin, J. Soria and M. Chong. A study of the evolution and characteristics of the invariants of the velocity-gradient tensor in isotropic turbulence. *Journal of Fluid Mechanics*, 381:141, 1999.

[14] J. Soria, R. Sondergaard, B. Cantwell, M. Chong and A. Perry. A study of the fine-scale motions of incompressible time-developing mixing layers. *Physics of Fluids*, 19:219, 1994.

[15] H. Blackburn, N. Mansour and B. Cantwell. Topology of fine-scale motions in turbulent channel flow. *Journal of Fluid Mechanics*, 310:269, 1996.

[16] S.A. Stanley, S. Sarkar and J.P. Mellado. A study of the flow-field evolution and mixing in a planar turbulent jet using direct numerical simualtion. *Journal of Fluid Mechanics*, 450:377–407, 2002.

[17] R.D. Moser, M.M. Rogers and D.W. Ewing. Self-similarity of time-evolving plane wakes. *Journal of Fluid Mechanics*, 367:255–289, 1998.

[18] *Vortex Street Near Madeira Island* – Visible Earth, accessed April 29, 2002. `http://visibleearth.nasa.gov/view.php?id=63391`

[19] *Fun Facts: Why is Formula 1 the pinnacle of motorsports?* – Biser3a, accessed April 29, 2012. `http://biser3a.com/formula-1/fun-facts-why-is-formula-1-the-pinnacle-of-motorsports/`

[20] *Starry Night* – Van Gogh Gallery, accessed April 29, 2012. `http://www.vangoghgallery.com/catalog/Painting/508/Starry-Night.html`

[21] R. Ecke. The Turbulence Problem: An Experimentalist's Perspective. *Los Alamos Science*, 29, 2005.

[22] O. Reynolds. An experimental investigation of the circunstances which determine whether the motion of water shall be direct or sinuous, and of the law of resistance in parallel channels. *Philosophical Transactions of the Royal Society of London*, 174:935–982, 1883.

[23] H. Tennekes and J.L. Lumley. A First Course in Turbulence. Massachusets Institute of Technology, USA, 1972.

[24] A. Tsinober. An Informal Introduction to Turbulence. Kluwer Academic Publishers, USA, 2004.

[25] J. Jiménez. Turbulence and vortex dynamics. Madrid (Spain) and Stanford (USA), 2004.

[26] E.D. Siggia. Numerical Study of Small-Scale Intermittency in Three-Dimensional Turbulence. *Journal of Fluid Mechanics*, 107:375–406, 1981.

[27] S. Douady, Y. Couder and M.E. Brachet. Direct observation of the intermittency of intense vortex filaments in turbulence. *Physical Review Letters*, 64:983, 1991.

[28] M. Lesieur. Turbulence in fluids. Kluwer, third edition, 1997.

[29] L.F. Richardson. Weather prediction by numerical process. Cambridge University Press, UK, 1922.

[30] A.N. Kolmogorov. The local structure of turbulence in incompressible viscous fluids at very large Reynolds numbers. Doklady Akademii Nauk, USSR, 30:301–305, 1941. Reprinted in *Proceedings of the Royal Society A*, 434:9–13, 1991.

[31] A. Obukhov. Spectral energy distribution in turbulent flow. Doklady Akademii Nauk, USSR, 1:22–24, 1941.

[32] S.B. Pope. Turbulent Flows. Cambridge Universidade Press, UK, 2000.

[33] F.O. Thomas and K.M.K. Prakash. An investigation of the natural transition of an untuned planar jet. *Physics of Fluids*, 3:90–105, 1991.

[34] *World's Biggest Dam - Three Gorges - China* – Myclipta.com, accessed April 29, 2012. `http://myclipta.blogspot.pt/2010/11/worlds-biggest-dam-three-gorges-china.html`

[35] *Icelandic Smoke Monster Ash Continues to Halt Travel* – Gothamist, accessed April 29, 2012. `http://gothamist.com/2010/04/17/icelandic_smoke_monster_ash_continu.php`

[36] *Using Plants Instead of Petroleum to Make Jet Fuel* – Scientific American, accessed April 29, 2012. `http://www.scientificamerican.com/article.cfm?id=using-plants-instead-of-petroleum-to-make-jet-fuel`

[37] R.J.N. Reis. The dynamics of coherent vortices near the Turbulent/Non-turbulent Interface analysed by Direct Numerical Simulations. Ph.D. thesis, Instituto Superior Técnico, Lisboa, 2011.

[38] R.M.R. Taveira. Direct Numerical Simulation of the Turbulent Entrainment in Jets - A Fundamental Study. Master thesis, Instituto Superior Técnico, Lisboa, 2008.

[39] S.C. Crow and F.H. Champane. Orderly structure in jet turbulence. *Journal of Fluid Mechanics*, 48:547–591, 1971.

[40] K.B.M.Q. Zaman and A.K.M.F. Hussain. Vortex pairing in a circular jet under controlled excitation. Part 1. General jet response. *Journal of Fluid Mechanics*, 101:449–491, 1980.

[41] G. Urbin and O. Métais. Large-eddy simulations of three-dimensional spatially-developing round jets. In P.R.V.J.P. Chollet and L. Kleiser, editors, Direc and large-eddy simulations II, 539–542. Kluwer Academic Publishers, 1997.

[42] C.-M. Ho and P. Huerre. Perturbed free shear layers. *Annual Review of Fluid Mechanics*, 16:356:425, 1984.

[43] C.B. da Silva. The role of coherent structures in the control and interscale interactions of round, plane and coaxial jets. Ph.D. thesis, Institut National Politechnique de Grenoble, France, 2001.

[44] S. Corrsin and A.L. Kistler. Free-stream boundaries of turbulent flows. Technical Report TN-1244, NACA, 1955.

[45] A.A. Townsend. The mechanism of entrainment in free turbulent flows. *Journal of Fluid Mechanics*. 26:689–715, 1966.

[46] C.B. da Silva and R.R. Taveira. The thickness of the turbulent/nonturbulent interface is equal to the radius of the large vorticity structures near the edge of the shear layer. *Physics of Fluids*, 22:121702, 2010.

[47] G. Brown and A. Roshko. On density effects and large structure in turbulent mixing layers. *Journal of Fluid Mechanics*, 64:775–816, 1974.

[48] W. Dham and P. Dimotakis. Measurements of entrainment and mixing in turbulent jets. *The American Institute of Aeronautics and Astronautics*, 25:1216–1223, 1987.

[49] J.A. Ferré, J.C. Mumford, A.M. Savill and F. Giralt. Three-dimensional large-eddy motions and fine-scale activity in a plane turbulent wake. *Journal of Fluid Mechanics*, 210:371–414, 1990.

[50] P.E. Dimotakis. The mixing transition in turbulent flows. *Journal of Fluid Mechanics*, 409:69–98, 2000.

[51] D.K. Bisset, J.C.R. Hunt and M.M. Rogers. The turbulent/non-turbulent interface bounding a far wake. *Journal of Fluid Mechanics*, 451:383–410, 2002.

[52] J. Westerweel, C. Fukushima, J.M. Pedersen and J.C.R. Hunt. Momentum and scalar transport at the turbulent/non-turbulent interface of a jet. *Journal of Fluid Mechanics*, 631:199–230, 2009.

[53] C.B. da Silva, R.J.N. dos Reis and J.C.F. Pereira. The intense vorticity structures near the turbulent/non-turbulent interface in a jet. *Journal of Fluid Mechanics*, 685:165–190, 2011.

[54] M. Holzner, A. Liberzon, B. Luthi, N. Nikitin, W. Kinzelbach and A. Tsinober. A lagrangian investigation of the small-scale features of turbulent entrainment through particle tracking and direct numerical simulation. *Journal of Fluid Mechanics*, 598:465–475, 2008.

[55] C.B. da Silva and J.C.F. Pereira. Analysis of the gradient-diffusion hypothesis in large-eddy simulations based on transport equations. *Physics of Fluids*, 19:035106, 2007b.

[56] C.B. da Silva. The behaviour of subgrid-scale models near the turbulent/nonturbulent interface in jets. *Physics of Fluids*, 21:081702, 2009.

[57] C.B. da Silva and J.C.F. Pereira. Erratum: “Invariants of the velocity-gradient, rate-of-strain, and rate-of-rotation tensors across the turbulent/nonturbulent interface in jets.” [*Physics of Fluids*, 20:055101, 2008]. *Physics of Fluids*, 21:019902, 2009.

[58] P.A. Davidson. Turbulence, An Introduction for Scientists and Engineers. Oxford University Press, USA, 2004.

[59] J. Jiménez, A. Wray, P. Saffman and R. Rogallo. The structure of intense vorticity in isotropic turbulence. *Journal of Fluid Mechanics*, 255:65–90, 1993.

[60] E. Balaras, U. Piomelli and J. Wallace. Self-similar states in turbulent mixing layers. *Journal of Fluid Mechanics*, 446:1, 2001.

[61] C.B. da Silva and O. Métais. Vortex control of bifurcating jets: A numerical study. *Physics of Fluids*, 14:3798, 2002.

[62] F. Moisy and J. Jiménez. Geometry and clustering of intense structures in isotropic turbulence. *Journal of Fluid Mechanics*, 513:111, 2004.

[63] M.P. Escudier, F. Presti and S. Smith. Drag reduction in the turbulent pipe flow of polymers. *Journal of Non-Newtonian Fluid Mechanics*, 81:197–213, 1999.

[64] R.B. Bird, R.C. Armstrong and O. Hassager. Dynamics of Polymeric Liquids, John Wiley and Sons, second edition, 1987.

[65] M. Doi. Introduction to Polymer Physics. Oxford University Press, UK, 1996.

[66] J.L. Lumley. Drag reduction by additives. *Annual Review of Fluid Mechanics*, 1:367–384, 1969.

[67] G. Ryskin. Turbulent drag reduction by polymers: a quantitative theory. *Physical Review Letters*, 59:2059–62, 1987.

[68] D.D. Joseph. Fluid Dynamics of Viscoelastic Liquids. Springer-Verlag, 1990.

[69] M. Tabor and P.G. de Gennes. A cascade theory of drag reduction. *Europhysics Letters*, 2:519–22, 1986.

[70] J.L. Lumley. Drag reduction in turbulent flow by polymer additives. *Journal of Polymer Science: Macromolecular Reviews*, 7:263–90, 1973.

[71] K.R. Sreenivasan and C.M. White. The onset of drag reduction by dilute polymer additives, and the maximum drag reduction asymptote. *Journal of Fluid Mechanics*, 409:227–255, 2000.

[72] T. Min, H. Choi and J.Y. Yoo. Maximum drag reduction by polymer additives in a turbulent channel flow. *Journal of Fluid Mechanics*, 492:91–100, 2003.

[73] Q. Zhou and R. Akhavan. A comparison of FENE and FENE-P dumbbell and chain models in turbulent flow. *Journal of Non-Newtonian Fluid Mechanics*, 109:115–155, 2003.

[74] S. Orszag and G. Patterson. Numerical simulation of three-dimensional homogeneous isotropic turbulence. *Physical Review Letters*, 28:76–79, 1972.

[75] J. Jiménez. Computing high-Reynolds-number turbulence: will simulations ever replace experiments?. *Journal of Turbulence*, 4:N22, 2003.

[76] J. Jiménez. Turbulence, in Perspectives in Fluid Mechanics. Cambridge University Press, UK, 2000.

[77] Y. Kaneda and T. Ishihara. High-resolution direct numerical simulation of turbulence. *Journal of Turbulence*, 7(20):1–17, 2006.

[78] A. Dewan, M. Pathak and K.A. Dass. A survey of selected literature on important flow properties and computational fluid dynamics treatments of incompressible turbulent plane and round jets in quiescent ambient. *Indian Journal of Engineering and Materials Sciences*, 13:180–194, 2005.

[79] R. Akhavan, A. Ansari, S. Kang and N. Mangiavacchi. Sub grid-scale interactions in a numerically simulated planar turbulent jet and implications for modeling. *Journal of Fluid Mechanics*, 408:83–120, 2000.

[80] C.B. da Silva and J.C.F. Pereira. The effect of subgrid-scale models on the vortices computed form large-eddy simulations. *Physics of Fluids*, 16:4506–4534, 2004.

[81] J. Ferziger and M. Perich. Computational methods for fluid dynamics. Springer-Verlag, 1996.

[82] C. Canuto, M. Hussaini, A. Quarteroni and T. Zang. Spectral Methods in Fluid Dynamics. Springer-Verlag, 1987.

[83] C.B. da Silva and O. Metáis. On the influence of coherent structures upon interscale interactions in turbulent plane jets. *Journal of Fluid Mechanics*, 473:103–145, 2002.

[84] C.B. da Silva and J.C.F. Pereira. On the local equilibrium of the subgrid scales: The velocity and scalar fields. *Physics of Fluids*, 17:1–4, 2005.

[85] A. Robert. Fundamental Physics Underlying Polymer Drag Reduction from DNS of Homogeneous Shear and Isotropic Turbulence with FENE-P Model. Ph.D. thesis, The Pennsylvania State University, USA, 2008.

[86] R. Benzi, E. De Angelis, V.S. L'vov, I. Procaccia and V. Tiberkevich. Maximum drag reduction asymptotes and the cross-over to the Newtonian plug. *Journal of Fluid Mechanics*, 551:185–95, 2006.

[87] P. Resende. Turbulence models for viscoelastic fluids. Ph.D. thesis, Faculdade de Engenharia da Universidade do Porto, Portugal, 2005.

[88] F.T. Pinho, C.F. Li, B.A. Younis and R. Sureshkumar. A low Reynolds number turbulence closure for viscoelastic fluids. *Journal of Non-Newtonian Fluid Mechanics*, 154:89–108, 2008.

[89] A. Liberzon, M. Holzner, B. Lüthi, M. Guala and W. Linzelbach. On turbulent entrainment and dissipation in dilute polymer solutions. *Physics of Fluids*, 21:035107, 2009.

[90] A. Kurganov and E. Tadmor. New high-resolution central schemes for nonlinear conservation laws and convection-diffusion equations. *Journal of Computational Physics*, 160:241–282, 2000.

Appendix A

The Conformation Tensor Transport Equation

The present appendix intend to give a more detailed description about the method used to obtain the transport equation for the conformation tensor mentioned in section 2.3.2. In the process, an appropriate characteristic length scale is determined in order to non-dimensionalize the transport equation for $\langle \mathbf{r}\mathbf{r}^T \rangle$. The steps followed to obtain that length scale are presented in the following section, along with the assumptions made. Then, the definition of the conformation tensor is presented and all the procedure of non-dimensionalization is fully described.

A.1 The Equilibrium Length

The equilibrium length used to non-dimensionalize the equation of motion for $\langle \mathbf{r}\mathbf{r}^T \rangle$, Eq. (2.47), is obtained by performing a few mathematical operations to that same equation but under two assumptions.

$$\frac{D\langle \mathbf{r}\mathbf{r}^T \rangle}{Dt} = \frac{\partial \langle \mathbf{r}\mathbf{r}^T \rangle}{\partial t} + \mathbf{u}\cdot\nabla\langle \mathbf{r}\mathbf{r}^T \rangle = \langle \mathbf{r}\mathbf{r}^T \rangle \cdot \nabla\mathbf{u} + \nabla\mathbf{u}^T \cdot \langle \mathbf{r}\mathbf{r}^T \rangle - \frac{\langle \mathbf{r}\mathbf{r}^T \rangle}{\lambda_p(1-\langle r^2\rangle/r_0^2)} + \frac{4kT}{\zeta}\mathbf{I} \tag{2.47}$$

Considering the time derivate negligible ($D/Dt = 0$) and that there is no flow ($\mathbf{u} = 0$), Eq. (2.47) yields:

$$0 = -\frac{\langle \mathbf{r}\mathbf{r}^T \rangle}{\lambda_p(1-\langle r^2\rangle/r_0^2)} + \frac{4kT}{\zeta}\mathbf{I}. \tag{A.1}$$

Then, the trace of Eq. (A.1) results in:

$$0 = -\frac{\langle r^2 \rangle}{\lambda_p(1-\langle r^2\rangle/r_0^2)} + \frac{12kT}{\zeta}, \tag{A.2}$$

since $Tr(\mathbf{r}\mathbf{r}^T) = \mathbf{r}\cdot\mathbf{r} = r^2$ and $Tr(\mathbf{I}) = 3$. Next,

$$\frac{\langle r^2 \rangle}{(1-\langle r^2\rangle/r_0^2)} = \frac{3kT\lambda_p}{H}, \tag{A.3}$$

and by introducing $\lambda_p = \zeta/4H$ into the above equation, one gets:

$$\frac{\langle r^2 \rangle}{(1 - \langle r^2 \rangle / r_0^2)} = \frac{3kT}{H}. \tag{A.4}$$

After some mathematical procedure, the final equation for the equilibrium length $\langle r^2 \rangle_{eq}$ is given by

$$\langle r^2 \rangle_{eq} = \frac{\frac{3kT}{H}}{1 + \frac{3kT}{Hr_0^2}}. \tag{A.5}$$

A.2 The Transport Equation

As mentioned in section 2.3.2, the equilibrium length $\langle r^2 \rangle_{eq}$ is used to non-dimensionalize $\langle \mathbf{r}\mathbf{r}^T \rangle$ and define a conformation tensor:

$$\mathbf{C} = \frac{\langle \mathbf{r}\mathbf{r}^T \rangle}{\frac{1}{3}\langle r^2 \rangle_{eq}}. \tag{2.49}$$

The substitution of Eq. (2.49) into Eq. (2.47) is straigthforward for all left-hand side (LHS) and for the first two terms on the right-hand side (RHS) of Eq. (2.47). The last two terms requires a little more work. Starting by the third term on RHS of Eq. (2.47), the substitution results in

$$\frac{1}{3}\langle r^2 \rangle_{eq} \frac{\mathbf{C}}{\lambda_p(1 - \langle r^2 \rangle / r_0^2)} = \frac{1}{3}\langle r^2 \rangle_{eq} \frac{\mathbf{C}}{\lambda_p} \left(\frac{r_0^2}{r_0^2 - \langle r^2 \rangle} \right). \tag{A.6}$$

On the other hand, the last term of the RHS must also be written in terms of $\frac{1}{3}\langle r^2 \rangle_{eq}$ and λ_p. Therefore, recovering Eq. (A.5) and solving in order to kT, one gets:

$$\langle r^2 \rangle_{eq} = \frac{\frac{3kT}{H}}{1 + \frac{3kT}{Hr_0^2}} \Leftrightarrow kT = \frac{1}{3}\langle r^2 \rangle_{eq} H \left(1 - \frac{\langle r^2 \rangle_{eq}}{r_0^2} \right)^{-1}. \tag{A.7}$$

Then, substituting in the last term of Eq. (2.47) and using $\lambda_p = \zeta/4H$, results

$$\frac{4kT}{\zeta}\mathbf{I} \Leftrightarrow \frac{1}{3}\langle r^2 \rangle_{eq} \frac{4H}{\zeta} \left(1 - \frac{\langle r^2 \rangle_{eq}}{r_0^2} \right)^{-1} \mathbf{I} = \frac{1}{3}\langle r^2 \rangle_{eq} \frac{1}{\lambda_p} \left(\frac{r_0^2}{r_0^2 - \langle r^2 \rangle_{eq}} \right) \mathbf{I}. \tag{A.8}$$

Using the previous relations, the last two terms from the transport equation for the conformation tensor yield

$$\frac{1}{3}\langle r^2 \rangle_{eq} \frac{r_0^2}{\lambda_p} \left(\frac{1}{r_0^2 - \langle r^2 \rangle} \mathbf{C} - \frac{1}{r_0^2 - \langle r^2 \rangle_{eq}} \mathbf{I} \right), \tag{A.9}$$

or in a more familiar form

$$\frac{1}{3}\langle r^2 \rangle_{eq} \frac{1}{\lambda_p} \frac{r_0^2}{r_0^2 - \langle r^2 \rangle_{eq}} \left(\frac{r_0^2 - \langle r^2 \rangle_{eq}}{r_0^2 - \langle r^2 \rangle} \mathbf{C} - \mathbf{I} \right). \tag{A.10}$$

With Eq. (A.10), the full transport equation for the conformation tensor is given by

$$\frac{1}{3}\left\langle r^2\right\rangle_{eq}\frac{D\mathbf{C}}{Dt}=\frac{1}{3}\left\langle r^2\right\rangle_{eq}\mathbf{C}\cdot\nabla\mathbf{u}+\frac{1}{3}\left\langle r^2\right\rangle_{eq}\nabla\mathbf{u}^T\cdot\mathbf{C}+\frac{1}{3}\left\langle r^2\right\rangle_{eq}\frac{1}{\lambda_p}\frac{r_0^2}{r_0^2-\left\langle r^2\right\rangle_{eq}}\left(\frac{r_0^2-\left\langle r^2\right\rangle_{eq}}{r_0^2-\left\langle r^2\right\rangle}\mathbf{C}-\mathbf{I}\right). \quad \text{(A.11)}$$

Dividing Eq. (A.11) by $\frac{1}{3}\left\langle r^2\right\rangle_{eq}$:

$$\frac{D\mathbf{C}}{Dt}=\mathbf{C}\cdot\nabla\mathbf{u}+\nabla\mathbf{u}^T\cdot\mathbf{C}+\frac{1}{\lambda_p}\frac{r_0^2}{r_0^2-\left\langle r^2\right\rangle_{eq}}\left(\frac{r_0^2-\left\langle r^2\right\rangle_{eq}}{r_0^2-\left\langle r^2\right\rangle}\mathbf{C}-\mathbf{I}\right) \quad \text{(A.12)}$$

For last, defining L^2 as

$$L^2=\frac{r_0^2}{\frac{1}{3}\left\langle r^2\right\rangle_{eq}} \quad \text{(A.13)}$$

and introducing into Eq. (A.12) results

$$\frac{D\mathbf{C}}{Dt}=\mathbf{C}\cdot\nabla\mathbf{u}+\nabla\mathbf{u}^T\cdot\mathbf{C}+\frac{1}{\lambda_p}\frac{L^2}{L^2-3}\left(f(R)\mathbf{C}-\mathbf{I}\right), \quad \text{(A.14)}$$

where the *Peterlin function* is defined as

$$f(R)=\frac{L^2-3}{L^2-R^2}, \quad \text{(A.15)}$$

with R^2 being the non-dimensional polymer stretch,

$$R^2=\frac{r^2}{\frac{1}{3}\left\langle r^2\right\rangle_{eq}}=\frac{\mathbf{r}\cdot\mathbf{r}}{\frac{1}{3}\left\langle r^2\right\rangle_{eq}}=Tr(\mathbf{C}). \quad \text{(A.16)}$$